



AD-A278 761

NRL/MR/6790--94-7366



Experimental Studies of Very-High Mach Number Hydrodynamics

JACOB GRUN
CHARLES MANKA

*Beam Physics Branch
Plasma Physics Division*

BARRETT RIPIN

*Senior Scientist for Experiments
Plasma Physics Division*

ALFRED BUCKINGHAM

*Lawrence Livermore National Laboratory
Livermore, California*

IRA KOHLBERG

*Kohlberg Associates, Inc.
Alexandria, Virginia*



February 14, 1994

Approved for public release; distribution unlimited.

94 5 02 136

REPORT DOCUMENTATION PAGE

Form Approved
OMB No. 0704-0188

Public reporting burden for this collection of information is estimated to average 1 hour per response, including the time for reviewing instructions, searching existing data sources, gathering and maintaining the data needed, and completing and reviewing the collection of information. Send comments regarding this burden estimate or any other aspect of this collection of information, including suggestions for reducing this burden, to Washington Headquarters Services, Directorate for Information Operations and Reports, 1215 Jefferson Davis Highway, Suite 1204, Arlington, VA 22202-4302, and to the Office of Management and Budget, Paperwork Reduction Project (0704-0188), Washington, DC 20503.

1. AGENCY USE ONLY (<i>Leave Blank</i>)	2. REPORT DATE February 14, 1994	3. REPORT TYPE AND DATES COVERED Interim	
4. TITLE AND SUBTITLE Experimental Studies of Very-High Mach Number Hydrodynamics		5. FUNDING NUMBERS	
6. AUTHOR(S) Jacob Grun, Charles Manka, Barrett Ripin,* Alfred Buckingham,** and Ira Kohlberg†		8. PERFORMING ORGANIZATION REPORT NUMBER NRL/MR/6790-94-7366	
7. PERFORMING ORGANIZATION NAME(S) AND ADDRESS(ES) Naval Research Laboratory Washington, DC 20375-5320		10. SPONSORING/MONITORING AGENCY REPORT NUMBER	
9. SPONSORING/MONITORING AGENCY NAME(S) AND ADDRESS(ES) Office of Naval Research Arlington, VA 22217-5660		11. SUPPLEMENTARY NOTES	
11. SUPPLEMENTARY NOTES *Senior Scientist for Experiments **Lawrence Livermore National Laboratory, Livermore, CA †Kohlberg Associates, Inc., Alexandria, VA		12a. DISTRIBUTION/AVAILABILITY STATEMENT Approved for public release; distribution unlimited.	
12a. DISTRIBUTION/AVAILABILITY STATEMENT		12b. DISTRIBUTION CODE	
13. ABSTRACT (<i>Maximum 200 words</i>) We present results of experiments on very-high Mach number (> 100) shocks and very-high Mach number and Reynolds number (> 100, 10 ⁶) turbulence. Such high Mach number hydrodynamics are initiated with a powerful laser pulse driver. We show that shocks created with a laser driver follow the Taylor-Sedov self-similar solution and scale via the Sachs scaling law just like shocks created by more traditional methods. In one experiment we examined laser-produced-shock solid-surface interactions and observed expected phenomena such as Mach stems and triple points, and also measured a new phenomenon termed a blast wave decursor. In second experiment we found that shocks become unstable if they propagate through a gas which has a low adiabatic index and we measured the growth rate of the instability. In a third experiment we have shown that a high Mach number shock dramatically enhances the structure of a turbulent field through which it passes and that the shock is itself badly distorted. This result is unexpected since common wisdom has it that high Mach number shocks would self-heal as they pass through a turbulent field.			
14. SUBJECT TERMS Turbulence Shock		15. NUMBER OF PAGES 76	
17. SECURITY CLASSIFICATION OF REPORT UNCLASSIFIED		16. PRICE CODE	
18. SECURITY CLASSIFICATION OF THIS PAGE UNCLASSIFIED		20. LIMITATION OF ABSTRACT UL	
19. SECURITY CLASSIFICATION OF ABSTRACT UNCLASSIFIED		20. LIMITATION OF ABSTRACT	

CONTENTS

1.	INTRODUCTION	1
2.	EXPERIMENTS	3
	2.1 LASER-PRODUCED SHOCKS BEHAVE NORMALLY	3
	2.2 HIGH MACH NUMBER SHOCKS BECOME UNSTABLE IN A LOW γ GAS	7
	2.3 HIGH MACH NUMBER SHOCKS AMPLIFY TURBULENCE SPECTRUM	9
3.	SUMMARY	9
4.	REFERENCES	11
	APPENDIX - RELEVANT PUBLICATIONS	13

Accession For	
NTIS GRA&I	<input checked="" type="checkbox"/>
DTIC TAB	<input type="checkbox"/>
Unannounced	<input type="checkbox"/>
Justification	
By _____	
Distribution _____	
Availability Codes	
Dist	Avail and/or Special
A-1	

EXPERIMENTAL STUDIES OF VERY-HIGH MACH NUMBER HYDRODYNAMICS

J. Grun¹, C. K. Manka¹, B. H. Ripin¹, A. C. Buckingham², and I. Kohlberg³

¹Plasma Physics Division, Naval Research Laboratory, Washington DC 20375, USA

²Lawrence Livermore National Laboratory, Livermore, Ca, USA

³Kohlberg Associates, Inc., Alexandria, VA 22304, USA

Abstract. We present results of experiments on very-high Mach number (>100) shocks and very-high Mach number and Reynolds number (>100 , 10^6) turbulence. Such high Mach number hydrodynamics are initiated with a powerful laser pulse driver. We show that shocks created with a laser driver follow the Taylor-Sedov self-similar solution and scale via the Sachs scaling law just like shocks created by more traditional methods. In one experiment we examined laser-produced-shock solid-surface interactions and observed expected phenomena such as Mach stems and triple points, and also measured a new phenomenon termed a blast wave decursor. In second experiment we found that shocks become unstable if they propagate through a gas which has a low adiabatic index and we measured the growth rate of the instability. In a third experiment we have shown that a high Mach number shock dramatically enhances the structure of a turbulent field through which it passes and that the shock is itself is badly distorted. This result is unexpected since common wisdom has it that high Mach number shocks would self-heal as they pass through a turbulent field.

Key words: Laser matter interaction, Shock, Turbulence, Blast wave, Decursor, Shock instability, Shock turbulence interaction

1. Introduction

High Mach number and high Reynolds number hydrodynamics occurs in man made and natural phenomena. Examples include wakes and shocks generated by hypersonic vehicles, shocks from surface discontinuities on hypersonic vehicles interacting with a turbulent boundary layer near the vehicle surface, shocks induced by jet or slot coolant injection interacting with separated shear layers, flows within ramjet engines, and supernovae explosions. The nature of the interactions between the different flows can influence eddy transport, component mixing, diffusion, surface shear, and heat transfer - and thus have important consequences in practical systems. Shock instabilities are thought to play a role in structures seen in supernovae remnants and in galaxy and star formation.

Very high Mach number and Reynolds number flows are initiated at the Naval Research Laboratory (NRL) using a powerful laser pulse driver. In these experiments a millimeter-diameter, few-micron thick target is placed in an evacuated chamber, which is then backfilled with gas. The target is irradiated and super-heated at an intensity of 1 to 100 Terawatts/cm² by a focused pulse from the Pharos III Nd-glass laser, which has three beams and produces up to 1500 Joules per pulse. A very thin (~ 1 micron) layer ablates from the target surface, expands rapidly into the background gas, and - much like the products of a chemical explosion - forms a shock wave expanding in the direction of the incident laser pulse (Grun, et al - 1981, 1986, Ripin, et al - 1986, Stamper, et al - 1988). The rest of the target is pushed into the background gas by the rocket-like effect of the ablating material. This part of the target rapidly falls apart due to the Raleigh Taylor instability (Grun, et al - 1984, 1987) creating high Mach number and high Reynolds number turbulence in the ambient gas.

Shock waves created by a laser pulse can have Mach numbers up to a few hundred, pressures up to tens of megabar, and temperatures from a fraction of eV to greater than 1 KeV. Turbulence spatial structure can have Reynolds numbers of the order of one to one hundred million. By using high atomic number target material x-ray radiation of a few KeV can be produced together with the hydrodynamics. Typical spatial

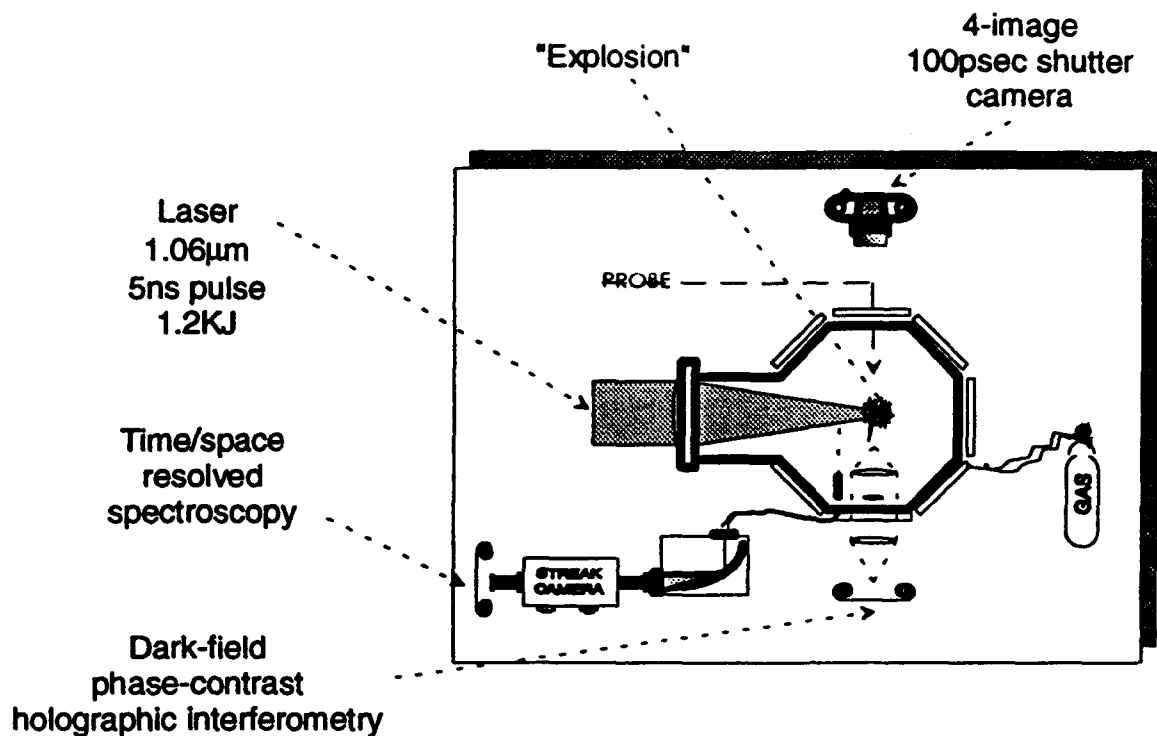


Figure 1. Setup of a typical experiment: Ablation from a target surface drives a high Mach number shock into a background gas while the rest of the target generates turbulence. The shock front or turbulence structures are recorded with optical shadowgraphy and interferometry techniques that are sensitive to index-of-refraction fluctuations. Examples of such methods are bright-field shadowgraphy, dark field shadowgraphy, phase-contrast-shadowgraphy, shearing interferometry and holographic interferometry. In our experiments up to four sequential frames can be recorded with these methods. The last three methods *produce quantitative results* that can be reliably compared to theory. In addition, the visible emission from the blast front is photographed with two very fast (100-psec shutter), four-frame, microchannel-plate intensifier cameras. Thus, on each shot we can record four shadowgraph or interferometric images, and eight emission frames, getting twelve photographs of the blast wave at different times in its evolution. Gas emission spectra are measured with time and space resolved spectroscopy. From these measurements the state of the gas is inferred. Fiber-optic sensors can be used to measure shock pressure.

and temporal scales are centimeter and microsecond. A special feature of the laser driver technique is that the ratio of energy to mass is an extremely high $\sim 10^9$ joule/gram, which is difficult to obtain by other means.

In this paper we summarize the results of three experiments: (1) an experiment which shows that laser-produced shocks behave like shocks produced by other methods. We demonstrate the formation of Mach stems and triple points, and show a new phenomenon termed a blast wave decursor. (2) an experiment which demonstrates that shocks become unstable if they propagate through a gas which has a low adiabatic index, and (3) an experiment which shows that a high Mach number shock enhances the structure of a turbulent field through which it passes and is itself distorted.

2. Experiments

2.1 Laser-produced shocks behave normally

We proceed to show that laser-produced shocks obey the Taylor - von Neumann - Sedov relation (Zel'dovich and Raizer - 1966) and the Sachs scaling law (Sachs - 1944). Ideal shocks (blast waves) propagate according to the relation

$$R \equiv \zeta (E/\rho_0)^{1/5} t^{2/5}, \quad \text{with} \quad \zeta = \left[\frac{75(\gamma-1)(\gamma+1)^2}{16\pi(3\gamma-1)} \right]^{1/5}, \quad (1)$$

where E is the explosion energy, ρ_0 is the ambient-gas density, t is the time of observation, and γ is the adiabatic index or ratio of specific heats. These expressions assume spherical symmetry, energy and momentum conservation, and an instantaneous, mass-less, point explosion. In our experiments we varied the laser energy, laser focal-spot size (and therefore the ablation velocity), pressure, and observation times. We found that as long as the ambient pressure is high enough (>0.5 torr) to place the experiment in a collisional regime, laser-produced shocks follow equation (1). From the data and equation (1) we determined that $\zeta = 1.0 \pm 0.1$ in a nitrogen ambient gas, which implies a γ of 1.3 (Ripin et al 1986). These results are shown in Figure 2.

Shock overpressure is determined from dark-field photographs such as that in Fig. 2 using the expressions (Kinney et al - 1985):

$$\frac{P}{P_0} = \frac{2\gamma}{\gamma+1} (M^2 - 1) \quad (2)$$

$$M = \frac{(dR/dt)}{C_0} \quad (3)$$

$$\frac{dR}{dt} \equiv [3(\gamma-1)(\gamma+1)^2/4\pi(3\gamma-1)]^{1/2} [E/\rho_0]^{1/2} R^{-3/2} \quad (4)$$

where P is the peak over-pressure, P_0 is the ambient pressure, M is the Mach number, and C_0 is the sound speed in the ambient gas. Figure 3 plots the overpressures inferred from equations 2-4 as a function of distance from the explosion scaled using the Sachs scaling law. This law, which is based on geometrical similarity principles and conservation of momentum, is used to compare experiments performed with different explosive yields and at different ambient pressures. Also plotted are curves expected of a Taylor - von Neumann - Sedov shock and shocks created with explosives (Kinney et al - 1985). Figure 3 shows that collisional laser-produced shocks follow the ideal scaling law and continue to do so even where

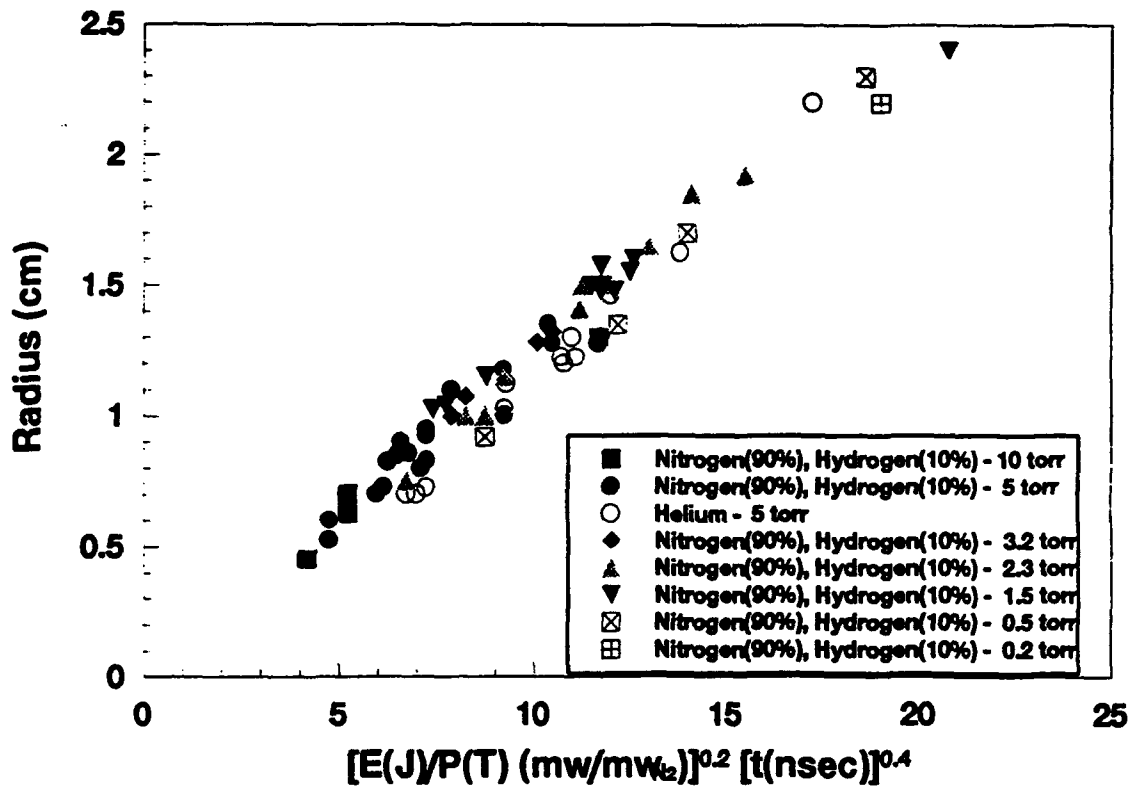


Figure 2. Top: Typical dark-field shadowgraph of a shock produced by irradiating an aluminum target. Bottom: A graph of shock location versus time shows that laser-produced shocks obey the Taylor - von Neumann - Sedov relation .

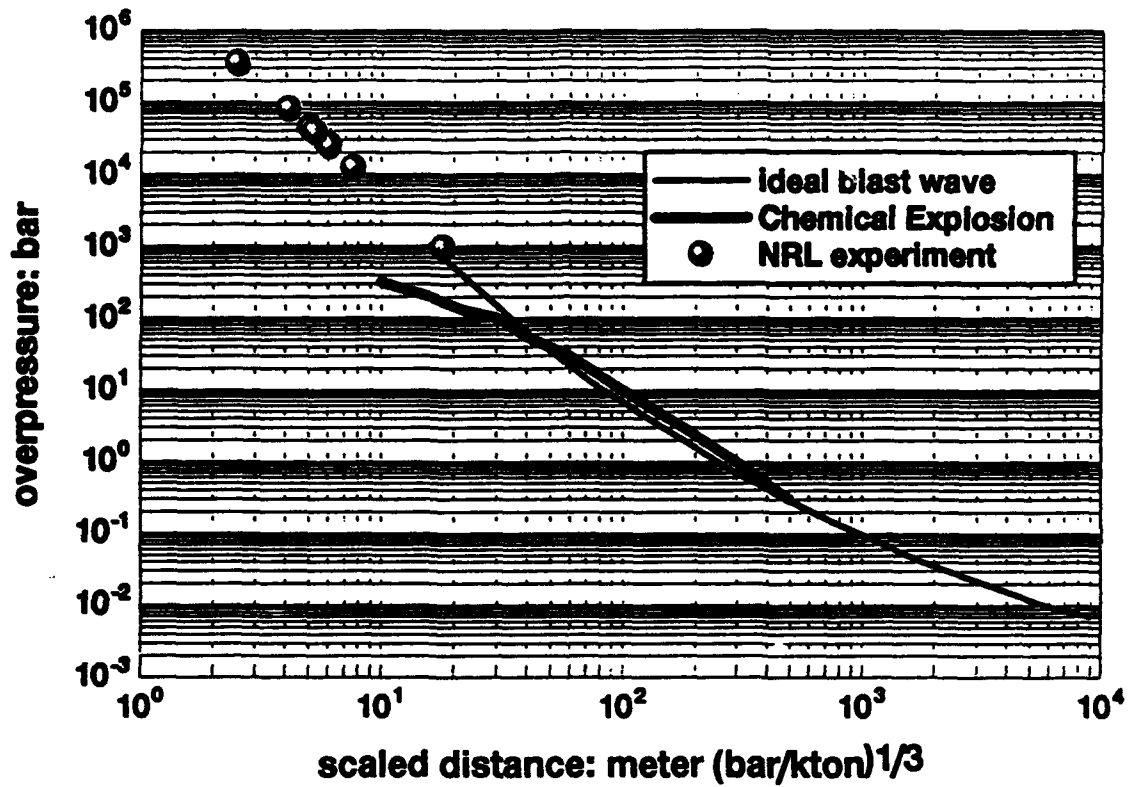


Figure 3. Overpressures of laser-created shocks compared to Taylor - von Neumann - Sedov shocks and shocks created by chemical explosions. Data is compiled on one plot utilizing the Sachs scaling law (Grun, et al. 1991).

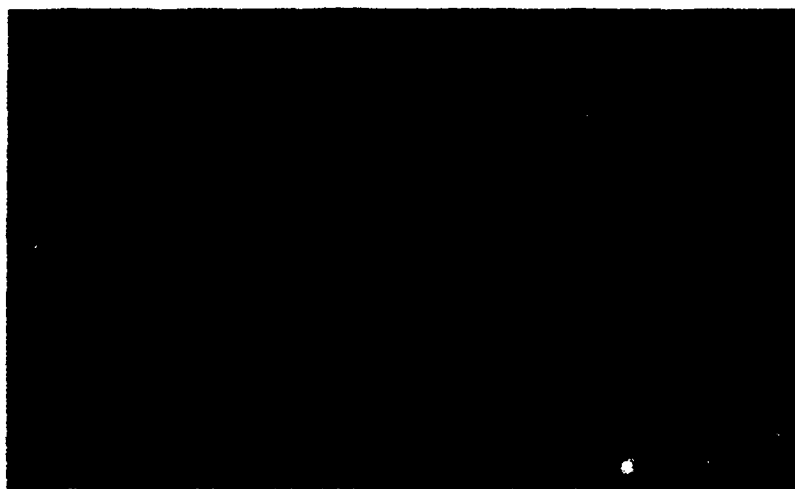


Figure 4. Decursor shock near the surface of an aluminum plane. Note the triple points and Mach stem in the reflected shock.

shocks produced with chemical explosives deviate from ideal scaling. Furthermore, the laser experiment produces shocks with overpressures greater than 100 kbar, which is more than 1000 times greater than the capability of conventional explosives. All this is a consequence of the very large energy to mass ratio of laser-produced "explosions".

It is well known that a blast wave colliding with a planar surface sets up a reflection that propagates back into the ambient gas heated by the passage of the incident front. The interacting incident and reflected blast fronts form Mach stems and triple points. If the sound speed near the reflecting surface is higher than in the rest of the ambient gas, part of the blast front moves faster and outruns the bulk of the blast wave forming a structure called a shock precursor (Glasstone and Dolan - 1977, Glowacki, et al -1986). When the sound speed near the reflecting surface is slower than in the rest of the ambient gas a part of the blast wave can lag behind the rest. The existence of such lagging structure, called a decursor, has been predicted theoretically and was observed first in our experiments. Figure 4 shows examples of Mach stems, triple points, and decursors measured in our experiments. See Grun, et al. 1991 for a discussion of these phenomena.

2.2 High Mach number shocks become unstable in a low γ gas

Shock instabilities are thought to contribute to the structuring observed in supernovae and play a role in the formation of stars and galaxies (Chevalier - 1976), Gerola and Seiden, -1978, Ostriker and Cowie - 1981), Trimble - 1988). Theories of shock instability in uniform ambient have been accompanied by considerable controversy (Isenberg - 1977, Cheng - 1979, Bernstein and Book - 1980, Gaffet- 1984, Kohlberg -1989, Newman - 1980, Vishniac - 1983), Ryu and Vishniac - 1987, Vishniac and Ryu -1989). with some concluding that such instabilities do not exist (Newman - 1980). Laser produced shocks have characteristics similiar in some respects to supernovae (Ripin, et al - 1990). Our experiments (Grun et al - 1991) show conclusively that shocks are unstable if they propagate through a uniform gas with a low adiabatic index γ (such as $\gamma=1.06$). These results were consistent with the 1989 theory of Vishniac and Ryu. A nonlinear analysis of our results was performed by Low and Norman in 1992.

The experiments were designed to compare the propagation of shocks through two gases: nitrogen and xenon. A basic difference between these gases is that nitrogen has an adiabatic index $\gamma_N=1.3 \pm 0.1$, while xenon has a much lower adiabatic index $\gamma_{Xe}=1.06 \pm 0.02$. To determine γ_{Xe} we utilized measurements which showed that shocks in both nitrogen and xenon propagate according to equation (1). Therefore, by dividing the measured radius R in nitrogen by the measured radius R in xenon at any given time we arrived at a relationship between γ_{Xe} , γ_N , and the mass of each gas species. Solving for γ_{Xe} as a function of γ_N , we found that as γ_N varies from 1 to 5/3, γ_{Xe} varies from 1 to 1.13. Hence, for any reasonable value of γ_N the value of γ_{Xe} must be less than 1.13. Moreover, since we have determined γ_N to be 1.3 ± 0.1 , γ_{Xe} must be 1.06 ± 0.02 .

γ_{Xe} is lower than γ_N because xenon gas radiates much more than nitrogen gas. Radiation increases the degrees of freedom within a gas and hence reduces its effective γ . This was demonstrated by examining the spectrum of light emanating from a point some distance in front of the laser's focal spot. In nitrogen gas the laser-induced explosion produces little measurable emission prior to the arrival of the shock. Immediately before the shock arrives at the observation point there is a slight increase of N^{1+} and N^{2+} lines: These lines are probably excited by UV or heat from the shock. When the shock front reaches the observation point there is a sudden increase in emission from the N^{1+} , N^{2+} , and target C^{2+} lines, as well as an increase in continuum emission. In contrast, xenon radiates copiously in many Xe^{1+} and some Xe^{2+} lines from the moment the laser hits the foil and well before the shock reaches the observation point. We conclude, therefore, that it is the radiation in xenon which reduces its effective γ below that of nitrogen.

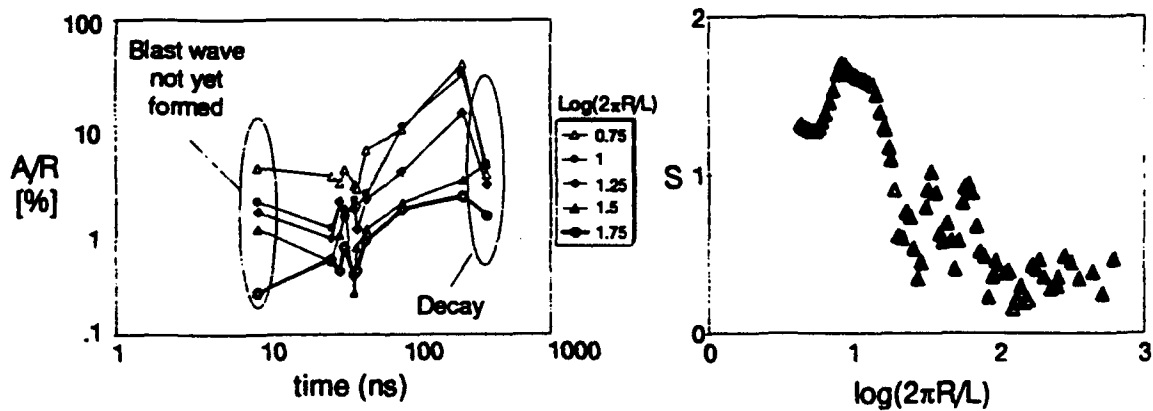
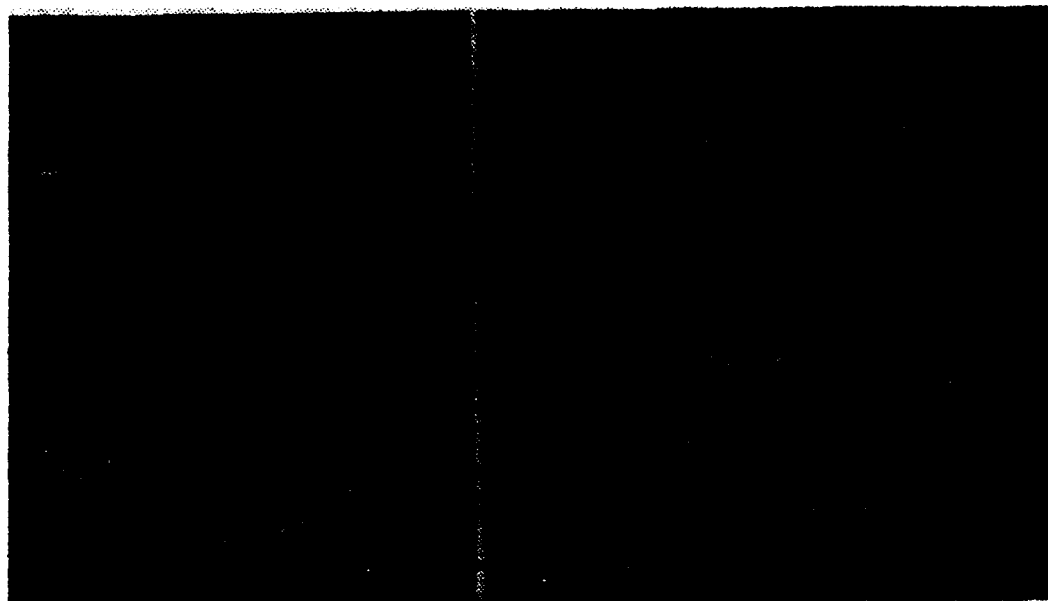


Figure 5. Top: Dark-field shadowgraph of: a stable blast wave in nitrogen gas, and an unstable blast wave in xenon gas. Bottom: Instability growth amplitude as a function of time for different values of $\text{log}(kR)$ and Growth exponent $S(kR)$.

Imaging diagnostics show that shocks propagating through nitrogen gas are stable and smooth. In startling contrast, shocks propagating through xenon gas become wrinkled like a dried prune! This wrinkling was quantified by tracing and then Fourier transforming the outer edge of the shock front and presenting the result as $A_t(k)/R$ versus $\log(kR)$, where $A_t(k)$ is the full amplitude of the mode with wavenumber k at time t , and R is the average radius of the shock boundary. A power law of the form $A_t(k)/R \cong t^{S(kR)}$ was fit to the $A_t(k)/R$ vs. time data and the exponent $S(kR)$ was determined. We found growth occurring for modes satisfying $0.7 < \log(kR) < 2$. Maximum growth occurred at $\log(kR) = 1$ where $S = 1.6$, and minimum growth, with $S = 0.3$, occurred at $\log(kR) = 2$.

2.3 High Mach number shocks amplify turbulence spectrum

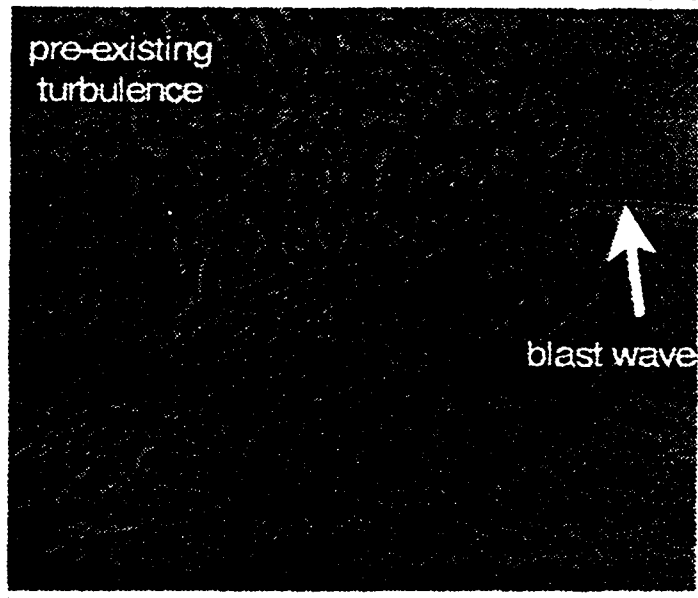
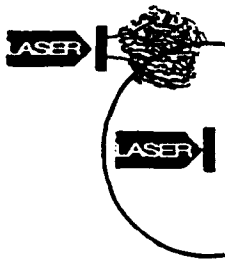
Consider what happens when a shock traverses a turbulent flow. To zero'th order the turbulence can be viewed as a collection of positive and negative "shock lenses" of various powers, sizes, and dimensions. A shock passing through those "lenses" breaks-up into shocklets that focus in some places and defocus in others. The focused shocklets quickly become nonlinear, deposit their energy in the turbulent field, and thereby alter its structure. Such shock-turbulence interactions have been studied both computationally and experimentally for low Mach number shocks (Trolrier and Duffy - 1985, Hartung and Duffy - 1986; Smits and Muck - 1987; Keller and Merzkirch - 1990; Buckingham - 1987, 1989, 1990, 1991; Crowley and Burk - 1991). Significant enhancement of the turbulence structure have been observed. However, there is a commonly held view that in the hypersonic regime (Mach >6) reinforcement of shock strength by nonlinear pressure field interactions heals any shock front irregularities and suppresses shock distortion as well as its influence on the turbulent field.

Our current work involves measuring the interaction of very high Mach number shocks with turbulent flows (Grun, et al - 1992, Buckingham and Grun - 1993). Such work is needed because information on the strongly interactive influence of high Mach number (>6) and high Reynolds number ($>10^6$) is virtually *non-existent*. Experimental data at Mach <6 in high Reynolds Number flows are neither useful nor extrapolateable to higher flow Mach number conditions because low Mach number flows do not exhibit sufficiently strong acoustical-density-temperature-velocity coupling to allow separation and analysis of these important physical effects. Furthermore, without the ability to vary important parameters, such as Mach number, over a broad hypersonic range understanding of Mach-Reynolds number coupling is difficult. The NRL experiment vary the Mach number over a broad hypersonic range and through systematic variation of this parameter we will examine the coupling of Reynolds number and Mach number.

Initial results indicate that contrary to common expectations a high Mach number (M=100) shock *does* enhance the structure of a turbulent field through which it passes. In addition, the shock itself is badly distorted as it passes through the turbulence. In the experiment turbulent flow is produced by accelerating a thin foil into a 5-Torr N_2 ambient background gas by irradiating the foil with one 300 J pulse from the PHAROS III laser. A second Pharos III beam creates a high Mach number shock which flows over the turbulent flow created by the first beam. The power spectral density (PSD) of the turbulent flow, which provides a quantitative measure of the turbulence, is measured with phase-contrast microscopy. Figure 6 shows the experimental result and a comparison of experimental pre-shocked and post-shocked turbulence spectrum with predictions by Lawrence Livermore Laboratory's large eddy simulation code (Buckingham and Grun - 1993).

3. Summary

We have shown that a kilojoule laser is a suitable driver for launching and studying very high Mach number hydrodynamic flows - flows that are difficult to study by any other method. Our experiments produced the first observations of a shock decursor as well as the first measurements of shock instability, and unexpected measurements of the intensification of a turbulent structure by a very high Mach number shock.



2cm

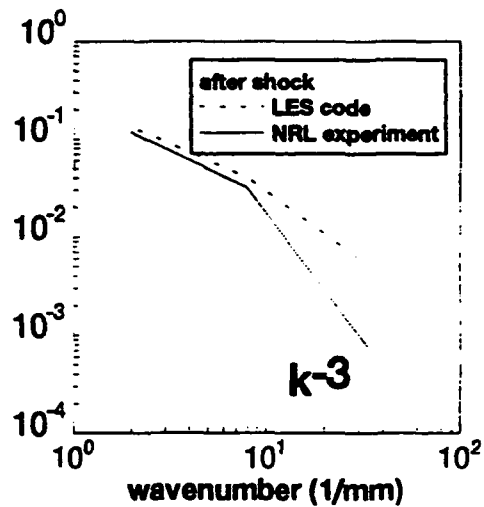
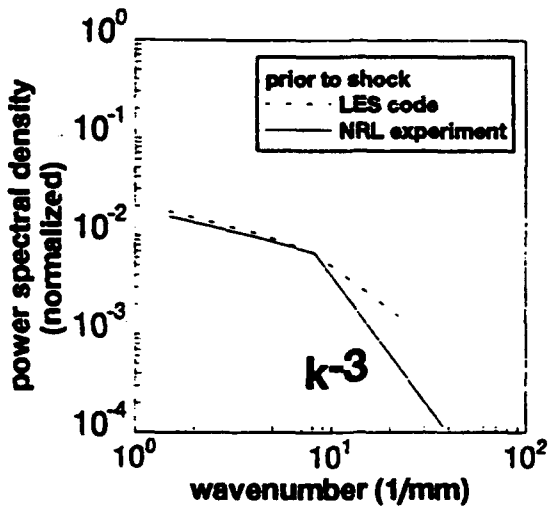


Figure 6: Top: A high Mach number shock changes the structure of turbulence through which it passes. In this experiment one beam of the Pharos laser created a structured flow while another created a high Mach number shock. Laser-beam and target geometries were arranged so that the shock would flow over the structure. Dark-field photographs like the one here produced a striking visual record of the enhancement in the pre-existing structure as it is over-run by a shock. Bottom: Comparison of pre and post shocked turbulence structure. (The experiment and code differ at high wave number because the experiment is in spherical and the code in cylindrical geometry.)

We are grateful to Mr. Ray Burris, Mr. Levi Daniels, Mr. Jim Ford, and Mr. Nicholas Nocerino for their expert and dedicated technical assistance. We acknowledge enlightening exchanges with Dr. Ethan Vishniac, Dr. Jim Barthel and Dr. David Book. This work was supported by the Office of Naval Research

4. References

- Bernstein I.B. and Book D.L. , *Astrophysical J.* **240**, 223 (1980) .
- Buckingham A.C. and Grun J., in "Numerical Methods in Laminar and Turbulent Flow" to be published (1993)
- Chevalier R.A. , *Astrophys. J.* **207**, 872 (1976).
- Cheng A. , *Astrophysical J.* **227**, 955 (1979).
- Gaffet B. , *Astron. Astrophys.* **135**, 94 (1984).
- Gaffet B. , *Astrophys. J.* **279**, 419 (1984).
- Gerola H. and Seiden P.E. , *Astropys. J.* **223**, 129 (1978).
- Glasstone S. and Dolan P.J. , "The effects of Nuclear Weapons", (United States Department of Defense and the Energy Research and Development Administration, Washington DC, 1977).
- Glowacki W.J., Kuhl A.L. , Glaz H.M. , and Ferguson R.E. in "Shock Waves and Shock Tubes", pg. 187, D. Bershader and R. Hanson editors, (Stanford University Press, Stanford, 1986); D. Krauss-Varban, *ibid.*
- Grun J. ,Decoste R. , Ripin B.H. , and Gardner J., *Appl. Phys. Lett.* **39**, 545 (1981).
- Grun J., Emery M.H., Kacenjar S., Opal C.B., McLean E.A., Obenschain S.P., Ripin B.H., and Schmitt A. *Phys. Rev. Lett.* **53**, 1352 (1984).
- Grun J. , Stellingwerf B. , and Ripin B.H. , *Phys. Fluids* **29**, 3390 (1986).
- Grun J., Emery M.H., Manka C.K., Lee T.N., McLean E.A., Stamper J, Obenschain S.P., Ripin B.H., *Phys. Rev. Lett.* **58**, pg. 2672 (1987).
- Grun J. , Stamper J. , Manka C.K. , Resnick J. , Burris R., and Ripin B.H. *Appl. Phys. Lett.* **59** (2), pg. 246 (1991).
- Grun J., Stamper J. , Manka C. ,Resnick J. ,Burris R. , Crawford J. , *Phys Rev. Lett.* **66**, pg. 2738 (1991).
- Isenberg P.A., *Astrophys. J.* **217**, 597 (1977).
- Kinney G.F. and Graham K.J., "Explosive Shocks in Air", (Springer-Verlag, New York, 1985).
- Kohlberg I. , *Kohlberg Associates Report KAINRL02-89* (1989).
- Low M.M. and Norman M.L. , "Nonlinear growth of Dynamical Overstabilities in Blast Waves" University of Illinois at Urbana-Champaign preprint 013 (July 1992).
- Newman W.I., *Astrophys. J.* **236**, 880 (1980).
- Ostriker J.P. and Cowie L.L, *Astrophys. J. Letters* **243**, L127 (1981).
- Ripin B.H., Ali A.W. Griem H.R., Grun J., Kacenjar S.T., Manka C.K., McLean E.A., Obenschain S.P., and Stamper J.A., *Laser Interactions and Related Plasma Phenomena*, Vol. 7 Hora H. and Miley G.H., editors (Plenum 1986)
- Ripin B.H., Manka C.K., Peyser T.A. McLean E.A., Stamper J.A. Mostovych A.N. Grun J., Kearney K., Crawford J.R., and Huba J.D. in "Laser and Particle Beams Volume 8 (Cambridge U. Press, 1990)
- Ryu D. and Vishniac E.T. , *Astrophys. J.* **313**, 820 (1987).
- Sachs P.G. " The Dependence of Blast on Ambient Pressure and Temperature", Aberdeen Proving Ground, Maryland, BRL Report No. 466 (1944).
- Sedov L.I. "Similarity and Dimensional Methods in Mechanics", (Academic Press, New York, 1959).
- Stamper J.A., Ripin B.H., Peterkin R.E. and Stellingwerf R.F., *Phys. Fluids* **31** 3353 (1988)
- Trimble V. *Rev. of Modern Physics* **60**, 859 (1988).
- Vishniac E.T. *Astrophys. J.* **274**, 152 (1983).
- Vishniac E.T. and Ryu D. , *Astrophys. J.* **337**, 917 (1989).
- Zel'dovich Ya. B. and Raizer Yu. P., "Physics of Shock Waves and High-Temperature Hydrodynamic Phenomena", (Academic Press, New York, 1966).

Appendix

Relevant Publications

**LARGE-EDDY SIMULATION OF
SHOCKWAVE PASSAGE THROUGH TURBULENCE**

LARGE-EDDY SIMULATION OF SHOCKWAVE PASSAGE THROUGH TURBULENCE

Alfred C. Buckingham
Center for Compressible Turbulence
Lawrence Livermore National Laboratory
Livermore, California

ABSTRACT

This is a discussion of progress on some continuing efforts to understand and predict the influence of shock waves on turbulent fields. Observations show that the average turbulent energy and Reynolds stress increase following shock interaction. Strong support for the peak stress amplification is provided by the sharply accelerated random strain field appearing immediately downstream of the shock. This is succeeded by a gradual decay from peak amplification to a new, more modestly amplified, near-equilibrium level that persists a substantial distance behind the shock. Practical interest is focused on the alterations to and influences of post-shock turbulent kinetic energy, transport, component mixing, wall shear, and heat transfer. This work addresses some fundamental questions that remain about the dynamics of the amplification process. Initially, viscoelastic turbulence response parameters are developed from Monte-Carlo shock structure computations to model the localized shock front interaction. In the post-shock decay region, compressible two dimensional large-eddy simulations (LES) are applied.

INTRODUCTION

When a shock moves in and interacts with an upstream turbulent field, the intensity of the fluctuating components (velocity, density, temperature) increases after the encounter. Turbulent component mixing, transport, and diffusion are correspondingly enhanced.

Basic understanding of the shock-turbulence interaction dynamics is required for accurately estimating the influence of the shock-enhanced turbulence on the design of components exposed to supersonic turbulent flow. It is required for the development of useful design-support predictive models and for the effective design of confirming experiments.

Considerations about the physics of shock turbulence interactions have a high priority in supersonic/hypersonic aerodynamic flow field design analysis, exposed surface materials selection, fabrication, and performance analysis, as well as supersonic combustion process and design analysis. Shock turbulence interaction

considerations also exert considerable influence on the, perhaps, less familiar work in simulating and modeling the evolution dynamics of thermal, electromagnetic, and radiation fields encountered in astrophysical, magnetically confined plasmadynamic, and inertial confinement fusion processes.

Many experimental observations of the enhancement of shocked turbulent field intensity during shock turbulence interactions are reported for jets, wakes, free shear layers and boundary layer flows.

Some of the variety of experimental configurations used in association with the present work include measurements from shock tube experiments in the reflected shock phase (Trolier and Duffy, 1985; Keller and Merzkirch, 1987), shock tube, incident shock phase measurements of the interaction with a pre-existing randomly varying density field (Hesselink and Sturtevant, 1988) and supersonic compression corner shock boundary layer interaction experiments (Smits and Muck, 1987).

While qualitative agreement exists on the enhancement of the turbulence by shock transition, the level of peak enhancement, the persistence of the enhancement downstream, the post shock energy partition and distribution, as well as changes to turbulent spectral structure, length and time scales are inconsistent, unresolved, or in disagreement.

This is not a criticism of the experiments but rather attests to the basic difficulty inherent in extracting turbulence information from compressible supersonic flows. This type of experiment imposes severe requirements on diagnostic technique development and the ingenuity of the experimentalist in designing the experiments and interpreting the results. One is faced with the formidable task of rapidly sampling a sufficient number of highly resolved statistical realizations from a supersonic background flow in order to be able to interpret and deduce useful information from as many as three uncorrelated statistical fields.

The collaboration between those involved in physical experiments with those involved in numerical simulations is becoming more common in practice. The present work on large-eddy simulations responds to this theme.

The computations are developed in the spirit of Bird's (1967) one-dimensional shock structure/transport simulations, but with an additional (transverse) dimension added for angular momentum exchange, curvature and vorticity development.

The statistical "reservoir states" for the ensemble of interactive encounter values describing upstream and downstream conditions had to be increased appropriate to the additional degrees of freedom. Pre-shocked and post-shocked states and the evolution of the distribution of states over the shockwave interaction region are simulated in a discretized macroscopic analogy to the asymptotic state conditions derived in Mott-Smith's (1951) theoretical expansion procedure for kinetic theory shock structure calculations.

Additional motivation for these simulations was provided by the theoretical observation of the viscoelastic response evident for an isotropic turbulence field on imposition of a sudden variation in mean strain. This finding was suggested in analyses of the evolution of turbulent field structure using direct interaction approximation (DIA) computations (Kraichnan, 1967).

Figure 3. shows the filtered, ensemble-averaged probability density distributions of fluctuating velocity (u^*), internal energy (E^*), and mass density (ρ^*) fluctuations computed through a distance swept by an unsteadily deforming shock front during interaction with turbulence. Here we are concerned with ensemble averaged peaks (designated with a double asterisk) of the distribution of the turbulence pressure, $p^{**} = \langle p^{**} \rangle \langle q^2 \rangle$, density fluctuations, $\langle \rho^{**} \rangle$, and, by implication, velocity fluctuations since $\langle q^2 \rangle = 1/2 \langle u_i^{**2} + u_j^{**2} \rangle$. The brackets, $\langle \rangle$, designate ensemble averages taken over 5 averaged realization distribution profiles.

The shock deforms and vibrates about its mean position (in a coordinate system moving with a Mach 3 shock front) as shown in the shaded silhouette trace on the right side of the figure. This trace is the spatial displacement swept by the shock front fluctuations over the total Monte Carlo simulation period. Details of the procedure and the results are reported in Buckingham (1989, 1990).

In preliminary tests, the Monte-Carlo simulations were applied for comparison to the Shigemi, Koyama, and Alhara (1976) unsteady shock resonance tube experiments. Results of simulations on the shock oscillation frequency as well as the entropy defect in comparison to stationary Hugoniot conditions (or approach to adiabaticity by unsteady shock waves) were compared with the resonance tube experiments. The Monte Carlo results, which include both the influence of random deformation of the front as well as random motion about the mean shock position somewhat overpredict the energy transferred to turbulence, but the predicted values and qualitative behavior (the apparent rate of decay of the rate of transfer of directed shock energy to turbulence energy with increasing Mach No.) appears to be reasonable representations of the experimental results. This, however, is a candidate for more systematic future investigations using a broader experimental data base, if available.

Table I summarizes some of the dimensional scale results of the Monte-Carlo simulations. Here the diminishing unsteady shock interaction motion range is traced from Mach 2 to Mach 6 in the Monte-Carlo simulations. This is designated D in the table. The values are ratioed to a unit unsteady displacement trace at Mach 2. The correlation length scales, Λ , of the principle eddy distortions of the shock front are given in the second column, again ratioed to the unit value assigned to the trace of the overall shock motion at Mach 2. This length scale, Λ , is an important parameter in the viscoelastic response model frequency discussed later. The ensemble averaged amplification of the preshocked turbulence streamwise kinetic energy component (initiated at 4% relative intensity) is given in the third column.

We move now to the general solution of the resolved grid scale motions and modifications used for the Smagorinsky subgrid scale eddy viscosity model. The solution is approximated on the discretized, time explicit, two-dimensional equations of compressible viscous flow, where averaging is mass-weighted (Favre, 1983) over the Smagorinsky modeled subgrid scale motions represented by a total, shear, buoyancy (bulk) and dilatation contribution to the eddy viscosity, ν_t .

The equations are written in conservation form prior to the discretization defining spatial mesh distribution and explicit time evolution. For simplicity, this description will be confined to a regular Cartesian coordinate space in contrast to the variety of coordinate transformations used in applications involving complex geometries. The variable labels are: coordinate directions, x_i , velocity components and their derivatives with respect to the coordinate directions, u_i , $u_{i,j}$, mass density, ρ , and specific total energy, $E = e + u_k^2/2$. Here e is the specific internal energy. A calorically corrected polytropic equation of state of the gas used for these trials; with static pressure, $p = (\gamma-1)\rho e$, temperature, $\theta = e/c_v$, where c_v is corrected for bound state excitation. The averaged mass, momentum, and energy conservation equations for the resolved scales are:

$$\rho_{,t} + (\rho u_k)_{,k} = 0, \quad (1)$$

$$(\rho u_i)_{,t} + (\rho u_i u_k)_{,k} = -p_{,i} + (\rho \nu_t S_{ik})_{,k} + \rho (\epsilon_{ijk} \phi_j)_{,k}, \quad (2)$$

$$(\rho E)_{,t} + (\rho E u_k)_{,k} = [(\rho \nu_t / n^*) E_{,k}]_{,k} + \rho \nu_t S_{ik} u_{i,k} - \rho u_{k,k} - \rho (\epsilon_{ijk} \phi_j)_{,k} u_i, \quad (3)$$

The tensor summation convention holds in the foregoing equations, ϵ_{ijk} is the standard alternating tensor and δ_{ik} is the Kronecker delta tensor.

The resolved scale deviatoric strain rate tensor on which the local shear production depends is given by,

$$S_{ik} = u_{i,k} + u_{k,i} - 2/3 u_{j,j} \delta_{ij}$$

Away from the shock, at modest finite distance, Ξ , the form of the eddy frequency given by equation (7) obtains directly.

The generalized eddy viscosity is given by,

$$\nu_t = (Cs\lambda)^2 f. \quad (10)$$

Results

Predicted LES from Buckingham (1991, symbol B) and from Rotman (1991, symbol R) shock amplification of the turbulent kinetic energy over the total grid is illustrated in Figures 4 and 5 in comparison to experimental values from Keller and Merzkirch (1990, symbol K & M). Figure 4 shows pre-shocked values of power spectral density while Figure 5 shows the post-shocked values. The power spectral densities which are different for the experiments and the simulations are rescaled and renormalized individually to the highest decade obtained in their post-shock value. Hence, spectral shape and relative change may be obtained from these figures instead of absolute quantitative values.

Here the Rotman results show some evidence of long period computational dissipation in the absence of a subgrid scale model while predicting an increase in the overall grid spectral energy content of about 20% following shock transition. The Buckingham results predict about an 85% increase in the kinetic energy while the experimental values at these flow conditions reflect a measured increase of about 150% where limited measurement site distributions may be reflected in this disparity. However, these results seem to confirm the utility of a formal procedure for modeling the influence of the non-resolvable subgrid scales even when using advanced, high resolution multi-grid shock capturing procedures for the resolved scales in LES.

The 3 compression corner cases illustrated in Figures 6, 7, and 8 serve to illustrate the need for recent efforts on implementing a more general subgrid scale model for near wall anisotropic compressible behavior.

In Figure 6 the effects of boundary layer diffraction and near wall dissipation on the sharply inclined oblique shockwave, supported by an 8 degree half angle compression corner, are apparent. The actual outermost streamline kinetic energy profile (at $y^+ = 0.6$) taken from the experiments of Smits and Muck (1987) shows a much more modest amplification than the results predicted by the LES scheme. Furthermore, the near-wall influences at $y^+ < 0.6$ could not be successfully modeled. The outermost streamline is the only one in which the results are comparable in the neighborhood of the wall.

Results for a 16 degree half angle compression corner, are shown in Figure 7. Somewhat more satisfactory agreement is obtained (in part, fortuitously) because of the emergence to a less shallow inclination of the shock in the shock boundary layer interactive region. Again, results for the lower lying streamlines indicate the need of improvement in the dissipative near-wall region.

Figure 8, indicates that for even steeper shocks the outermost streamline results are satisfactorily reasonable in comparison to experiment. It should also be noted that these current results represent ensemble averages over

at least five computational runs as opposed to the very inadequate results of single realizations previously shown. This confirms a suggestion made by Leith (1991) on analyzing the results of a properly set LES resolved scale data set as stochastic, with interpretations based on ensemble averages of a repeated set of realizations.

SUMMARY AND PROJECTIONS

More generally effective compressible subgrid scale models may be obtained by including the intensity of the density fluctuations as a parameter, together with a turbulent Mach number and including the influence of the compressible dilatation explicitly as pointed out in the analysis of the subgrid scale closure process by Speziale, Erlebacher, Zang and Hussaini (1988). In this work advantage is taken of the appropriate use of low Reynolds Number direct numerical simulations to illustrate some crucial features of the wave dominated turbulent transport region in comparison to the rotationally dominated region. Implementation and later encouraging results in the evolution of the LES scheme is provided in Erlebacher, Speziale, Hussaini and Zang (1990).

One of the several, more universal subgrid model developments is a two band grid to subgrid scale overlap model where an algebraic identity provides a procedure for making use of the resolved scale spectrum in dynamically altering subgrid scale eddy viscosity coefficients (Germono, Piomelli, Moin, and Cabot, 1991). This has been extended to compressible flows more recently by Moin, Squires, Cabot, and Lee (1991). Implementation and test are delayed by properly adjusting average frequencies along at least one homogeneous dimensional direction. In the present compression corner experiments this is represented by the spanwise direction. This work is in progress, but is inconclusive at this stage.

It is suggested that the shockwave turbulence interaction problem is a prototypical physical process that is imperfectly understood and yet dominates many typical supersonic and hypersonic flow investigations. It is also a daunting numerical problem combining the special problems of resolving shockwaves and turbulence. This discussion emphasizes current progress in developing all Reynolds no. compressible LES procedures to assist us in our investigation of the underlying physical mechanisms that govern the interaction. The discussion here focuses on the progress to date in the search for effective subgrid scale closure procedures and numerical algorithm development. The search is clearly far from over.

ACKNOWLEDGEMENTS

This is a report of work performed under the auspices of the U.S. Department of Energy by the Lawrence Livermore National Laboratory under Contract No. W-7405-Eng-48. The writer gratefully acknowledges the ideas, comments and suggestions that were developed in the many discussions with C. E. Leith, D. A. Rotman, and W. P. Dannevik during the course of this work.

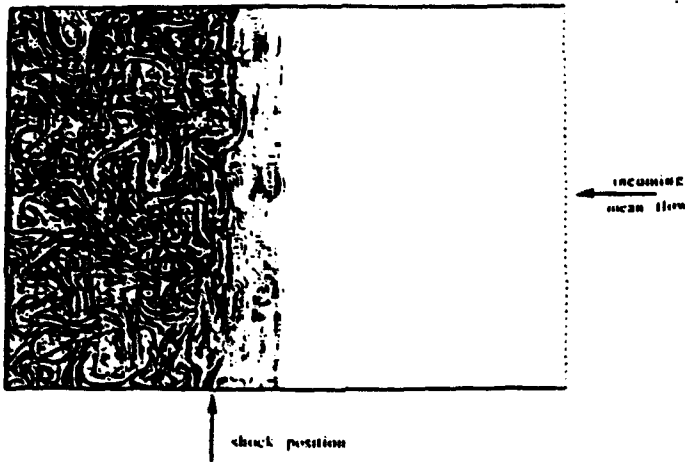


FIGURE 1. ROTMAN (1991) ADAPTIVE MESH GODUNOV LES DENSITY GRADIENT ILLUSTRATION OF $M = 1.5$ SHOCK PASSAGE THROUGH 4.7% RELATIVE INTENSITY DENSITY FLUCTUATIONS.

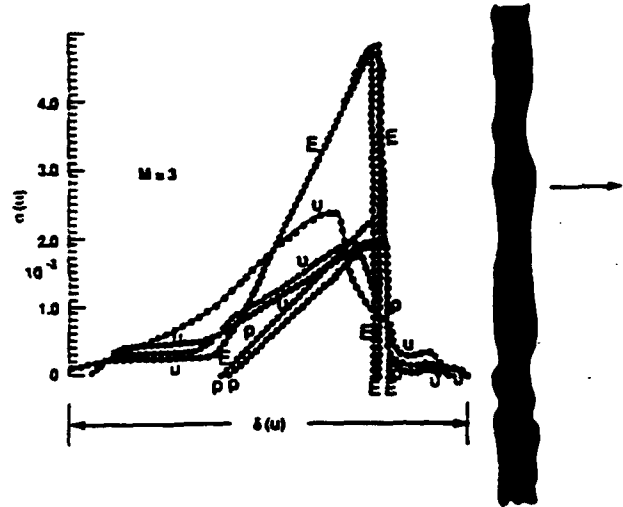


FIGURE 3. FILTERED AVERAGE PROBABILITY DENSITY DISTRIBUTIONS OF FLUCTUATIONS IN INTERNAL ENERGY (E), DENSITY (ρ) AND VELOCITY (U).

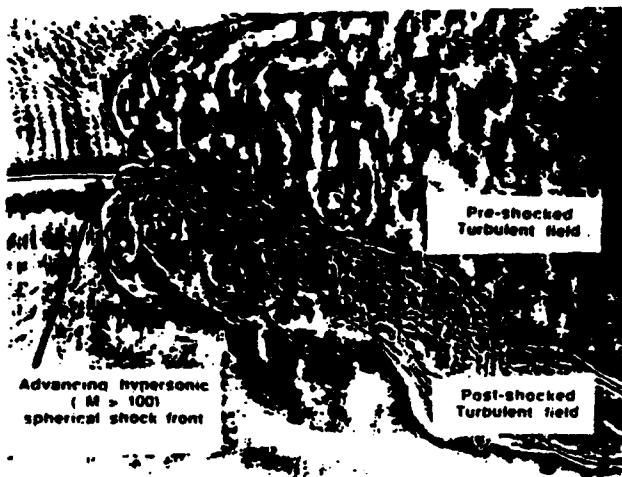


FIGURE 2. DARK FIELD SHADOWGRAPH OF LASER-GENERATED MACH 100 SHOCK OVER RUNNING AND DISTORTED BY PASSAGE THROUGH TURBULENCE.

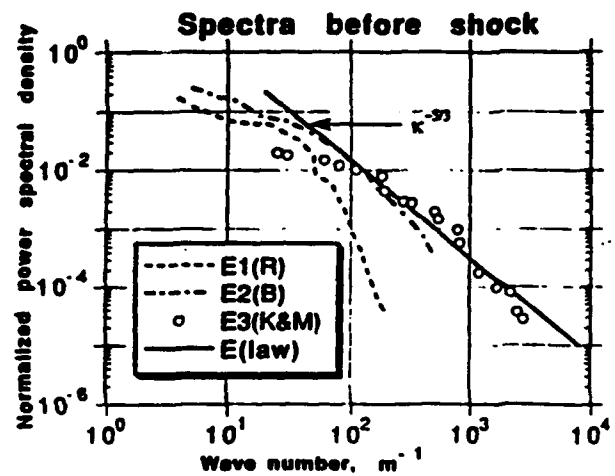


FIGURE 4. NORMALIZED POWER SPECTRAL DENSITY OF UPSTREAM TURBULENCE. COMPARING COMPUTED RESULTS FROM : ROTMAN (1991), E1(R); CURRENT RESULTS, E2(B); AND EXPERIMENTS OF KELLER AND MERZKIRCH (1990), E3(K&M).

**SUB-GRID SCALE MODELING FOR
LARGE-EDDY SIMULATIONS IN ANALYSIS OF
SHOCK-TURBULENCE INTERACTIONS**

SUB-GRID SCALE MODELING FOR LARGE-EDDY SIMULATIONS IN ANALYSIS OF SHOCK - TURBULENCE INTERACTIONS

Alfred C. Buckingham* and Jacob Grun**

*Center for Compressible Turbulence at Lawrence Livermore National
Laboratory, MC/L-321, P.O. Box 808, Livermore, California 94551, USA.

**Plasma Physics Division, Space Plasma Branch, Code 6795, Naval
Research Laboratory, Washington DC 20375, USA.

ABSTRACT

Presented are recent computational results in continuing work on the description and prediction of the influence of shock wave interactions on turbulence. Depending on the strength of the shock and the intensity of the pre-shocked turbulence, interaction may significantly increase turbulent energy and, in some situations, severely distort the shockwave. Behind the shock front, the amplification decays to a new, more modestly amplified state, relative to the pre-shocked level. Practical consequences include the influence of this shock turbulence enhancement on post-shock eddy transport, component mixing, diffusion, surface shear and heat transfer. In the present work, we combine a viscoelastic response model, developed from independent Monte-Carlo shock interaction simulations with compressible, large-eddy simulations (LES). Results are compared and interpretations developed with the aid of experiments, including some remarkable new data for very strong, hypervelocity shocks interacting with intense turbulence.

1. INTRODUCTION

When a shock interacts with a pre-existing turbulent field, a substantial enhancement of the turbulent intensity and a simultaneous distortion and realignment of the turbulent strain rate field and resulting turbulent stress field occurs. Component mixing, and transport are often significantly enhanced.

Combinations of low upstream turbulent intensity and strong shocks bring about the most pronounced changes in the level of turbulent intensity. Contrastingly, for weak shocks and intense upstream turbulence, shock distortions, and localized shock surface motions are most evident. However, very recent experimental evidence suggests that for intense upstream turbulence, significant shock distortions may develop in very strong, hypervelocity shock fields [1].

Accurate description of the shock-turbulence interactions is vital for development of useful predictions and predictive models of their influence on: supersonic/hypersonic flow field analysis, design, and materials selection, interior supersonic exterior flow field analysis, design, materials selection, interior supersonic combustion analysis and combustion chamber design. It is also crucial for accurately predicting the development and evolution of flow field generated thermal and electromagnetic radiation fields which are important considerations in supersonic/hypersonic configuration design analysis.

The shock tube experiments of Hesselink and Sturtevant [2] illustrate that substantial shock front deformation may occur when a weak shockwave traverses a relatively intense initial turbulent field. The interactions may even eventually lead to the apparent shock front break up of weak shocks into separate waves. These experiments are the focus of Rotman's [3] LES investigations discussed later. Emphasis was placed on capturing and resolving, as well as possible, the distortions of the shock front during interactive passage through turbulence. The multi-grid Euler procedure of Colella and Glaz [4] was adapted for these high-resolution shock interaction results using an initiated random velocity and density field.

In contrast, it is a commonly held view that if the interactive shock Mach number is in the hypersonic range (shock Mach numbers equal to or greater than about 6), rapid reinforcement of shock strength at the front by non-linear pressure field interactions and consequent self-healing of shock front geometric irregularity act to suppress front distortion and also suppress the influence of the shock interactions on turbulence. In the present work, recent experiments, numerical large eddy simulations (LES), and analysis are presented which contradict this notion. Pronounced shock front distortion and substantial interactive modification of the turbulence seems to persist even for shocks propagating at shock Mach numbers well in excess of 100.

A primary goal of the present work is to provide a supplementary, high precision, numerical simulation tool for augmenting the sparse experimental evidence on shock turbulence interactions at these elevated Mach Numbers. Some commonly held theoretical views (such as those described in the previous paragraph) appear to be, at least, inadequately descriptive of the limited experimental data and, more significantly, may be potentially misleading. Results of systematic numerical simulations for selected geometries and flow conditions may substantially improve this situation.

2. FORMULATION AND NUMERICAL PROCEDURE

The 2D subgrid-scale model used for most of the present work is the simple algebraic Smagorinsky model [5] with assumed isotropic production/dissipation balance, but adjusted at the sub-grid level for compressibility sources and dissipation. Point-to-point seeding of directly simulated space and time white random perturbational acceleration provides the initial disturbance. Evolution to the desired average initial turbulence field is computed over a predetermined initial trial computational phase. This process is repeated, as necessary, with slight alterations to the ensemble statistics until the prescribed initial preshocked turbulent state develops.

Favre [9] mass averaging is included in the discretized grid scale Navier Stokes equations which are written in conservation form. The general LES formulation follows directly from the model developments outlined for studies of the 2D shear layer in Leith [6] and for the compressible 3D turbulence massively parallel processor simulations of Leith [7].

A dynamic viscoelastic response model for the turbulent field changes on shock interaction couples directly to the shock-free Smagorinsky subgrid model through buoyancy source, divergence work and dilatational dissipation relations. Coupling occurs at the sub-grid scale characteristic frequency level. Use is made of relaxation and instantaneous modulus parameters developed in a previous phase of the present work through application of the results of direct Monte-Carlo shock structure simulations [8,9].

Perturbational variables developed from the Monte-Carlo simulations include ensemble-averaged probability density distributions of fluctuating velocity (u_i^*), internal energy (E^*), and mass density (ρ^*). The distributions are computed over a spatial range of statistical shock turbulence interaction equivalent to the physical distance swept by the deforming shock front during interaction with turbulence. For LES model application, use is made of specific ensemble averaged peak values, as well as correlations, and integral scales. The peak values are designated with a double asterisk. Consideration is given to peak turbulent pressure, $p^{**} = \langle \rho^{**} \rangle \langle q^2 \rangle$; peak fluctuations in mass density, $\langle \rho^{**} \rangle$; and, by implication, peak component velocity fluctuations, where $\langle q^2 \rangle = 1/2 \langle u_i^{**2} + u_j^{**2} \rangle$. Here the brackets, $\langle \rangle$, designate ensemble averages usually formed over 5 realization distributions.

The Monte-Carlo simulations also yield required correlation length scales of the principle shock front eddy distortions, Λ . This length scale is an important parameter in the viscoelastic response model frequency discussed later.

We move now to description of the general procedure. The LES grid scale (resolved) motions are developed from discrete approximations to the time dependent, two-dimensional equations of compressible viscous flow. Favre [9] mass-weighted averaging applies to the resolved motion scales down to a dimension of the order of the mesh spacing. The influence of the unresolved scales are modeled as single turbulence wave-length band grid scale averages or new two band scale overlap procedures at the scale division separating computed from unresolved scales of motion.

The latter yields a procedure for dynamic modifications to the compressible Smagorinsky sub-grid scale model that adjusts modeled near field behavior for wall influences and provides additional degrees of freedom for channeling the influence of the grid scale to the modeled subgrid scale motions. Test applications of the two band model are currently in progress. [10]. Here the subgrid scale compressibility is modeled by shear, buoyancy (bulk), and dilatation contributions to the eddy viscosity, ν_t .

For simplicity, this description will be confined to a regular Cartesian coordinate space, in contrast to the variety of coordinate transformations used in applications involving complex geometries. The variable notation used includes: coordinate directions, x_j ; velocity components and their derivatives

with respect to the coordinate directions, u_i , u_j ; mass density, ρ ; and specific total energy, $E = e + u_k^2/2$. Here e is the specific internal energy.

A calorically corrected quasi-ideal polytropic equation of state of the gas is used for the current tests, in which the static pressure is given simply by, $p = (\gamma-1)\rho e$. The caloric correction applies to the temperature, $\theta = e/c_v$, where c_v is corrected for bound state or continuum excitation.

The averaged mass, momentum, and energy conservation equations for the resolved scales are written:

$$\rho_{,t} + (\rho u_k)_{,k} = 0, \quad (1)$$

$$(\rho u_i)_{,t} + (\rho u_i u_k)_{,k} = -\rho_{,i} + (\rho v_t S_{ik})_{,k} + \rho(\epsilon_{ijk}\phi_j)_{,k}, \quad (2)$$

$$\begin{aligned} (\rho E)_{,t} + (\rho E u_k)_{,k} &= [(\rho v_t/n^*)E_{,k}]_{,k} + \rho v_t S_{ik} u_{i,k} \\ &- \rho u_{k,k} - \rho(\epsilon_{ijk}\phi_j)_{,k} u_i. \end{aligned} \quad (3)$$

The tensor summation convention holds in the foregoing equations, ϵ_{ijk} is the standard alternating tensor. Also, δ_{ij} denotes the Kronecker delta tensor.

The resolved scale deviatoric strain rate tensor on which the local shear production depends is given by,

$$S_{ik} = u_{i,k} + u_{k,i} - 2/3 u_{j,j} \delta_{ij}. \quad (4)$$

In some of the present computations tests are underway on stochastic backscatter influences. [10] These influence, to lowest order, the smallest resolved scales (marginally larger than the resolution scale of the grid). Definitive comments await further analysis.

However, for completeness, we introduce the form of the stochastic modeling used for testing these influences at this time. The influences are explicitly modeled using the space and time white random tensor acceleration potential developed by Leith [6,7],

$$\phi_k = C_b (f\delta t)^{3/2} (\lambda/\delta t) 2g_k. \quad (5)$$

This is applied at each grid point and at each explicit time step in the calculation, where the characteristic resolution length scale, λ , is taken to be twice the grid scale, Δx . This acts as a smoothing filter to partially compensate for coarse grain random errors that develop in propagating random disturbances at exactly the resolution scale. The explicit time step of the calculation is represented by δt . The vector term, g_k , components are unit gaussian random numbers, each drawn from a population with zero mean and unit variance. The generalized eddy frequency, f , and the constant, C_b , are identified in the subsequent Smagorinsky subgrid scale model discussion.

An implicit assumption is that the velocity field in a test problem contains an indefinitely large number of scales of motion (a unit Reynolds number of the order of perhaps 10^5 or greater), so that the classical Kolmogorov inertial range separation between production and dissipation emerges with a universal energy spectrum, $E(\kappa) = \alpha \varepsilon^{2/3} \kappa^{-5/3}$. This provides the necessary basis for the dimensional analysis scaling and arguments used for estimating the energy dissipation, ε . In the following outline K represents the total specific turbulent energy, $E(\kappa)$, integrated over the entirety of wave number, κ , space.

In the simple eddy viscosity concept, the local eddy stress tensor is directly related to the averaged rate of strain tensor field. In large eddy simulations, this averaged strain rate field consists of the explicitly resolved scales of motion,

$$T_{ij} = \nu_t S_{ij}, \quad (6)$$

and the shear production of the turbulent kinetic energy is given by the work in producing the eddy viscous stress,

$$K_{,t} = T_{ij} u_{i,j} = \nu_t S^2, \quad (7)$$

where the mean resolved strain rate, S , is defined so that,

$$S = (S_{ij} u_{i,j})^{1/2} = (\varepsilon_{ij} S_{ij}/2)^{1/2} \quad (8)$$

For compressible flow, the incompressible Smagorinsky balance condition between production and dissipation of the energy must be modified for the compressible buoyancy source, B , of kinetic energy (which reaches a peak at the passage of a shock wave), as well as the dilatational turbulence energy lost or dissipated by turbulent pressure work on local velocity divergence, KD . Here $D = u_{i,j}$, while the buoyancy source term, B , is computed from the product of buoyancy times acceleration,

$$B = - Sc^{-1} (\rho_{,j}/\rho) (\rho_{,j}/\rho). \quad (9)$$

Here Sc is a Schmidt number which was assigned a value of 0.7 as in Leith [6,7]. B is positive or zero. In shock interaction simulations, B represents the computed transient positive definite viscoelastic modulus based on instantaneous state and relaxation parameters developed from direct Monte-Carlo shock interaction simulations [8,9]. The compressibility modified Smagorinsky balance between production and dissipation is written,

$$\nu_t (S^2 + B) - 2/3 KD = \varepsilon, \quad (10)$$

from which the generalized eddy frequency away from the shock may be evaluated,

$$f = (S^2 + B + Cd^2 D^2)^{1/2} - CdD. \quad (11)$$

As observed by Leith [7], this is equivalent to the familiar Von-Neumann Richtmyer shock damping dissipation term when the dimensionless coefficient, C_d , is set equal to 10.

At the shock, we define the characteristic viscoelastic interaction response frequency from the parameters identified earlier,

$$G = [B + |g - B| \exp - (\Xi/\Lambda)^n], \quad (12)$$

$$g = \rho^{**}/(\langle \rho^{**} \rangle^2 \Lambda^2).$$

In the exponential relaxation term, Ξ , represents the stream wise distance behind the mean shock front position and the exponent, n , takes the value 2.5 in our present studies, based on the results of the stochastic shock interaction calculations discussed earlier. Near the shock, the generalized eddy frequency becomes,

$$f = (S^2 + G + C_d^2 D^2)^{1/2} - C_d D \quad (13)$$

Away from the shock, at modest finite distance, Ξ , the form of the eddy frequency given by equation (7) obtains directly.

The generalized eddy viscosity is given by,

$$v_t = (Cs\lambda)^2 f. \quad (14)$$

3. RESULTS AND COMPARISONS WITH EXPERIMENTS

We initiate this part of the discussion with results of simulations of shock boundary layer interactions on three two-dimensional wedge compression corners at a nominal Mach number of 2.7, in air. The three compression corner half angles are 8, 16 and 20 degrees. Detailed experimental average turbulence profiles, wall distributions and statistical structure boundary layer information are taken from the experiments of Smits and Muck [12]. In the interest of conserving space in this paper, one example, that of the 16 degree half angle test case, will be used for our discussions. In the experiments and the simulations an oblique shock forms at the upstream compression corner. The foot of the shock is immersed in a turbulent wall boundary layer layer, with which it interacts. Measured values of the turbulent kinetic energy distribution downstream of shock interaction ratioed to the measured upstream values are used as a basis of comparison and test of the LES plus shock interaction model.

In the experiments and the LES trials the distributions of turbulence kinetic energy are traced along three streamline paths displaced at $y^* = 0.2$, 0.4 and 0.6 from the wall surface, where y^* is the ratio of the normal distance from the wall to the total boundary layer thickness at the depicted fluid element transit time following shock interaction. Figure 1. shows the experimental vs. LES traces. It indicates that the computed turbulence distributions are reasonably comparable for the outermost streamline. This particular displacement is the most removed from the near wall influences.

**Shock - boundary layer TKE amplification
16 degree wedge compression corner**

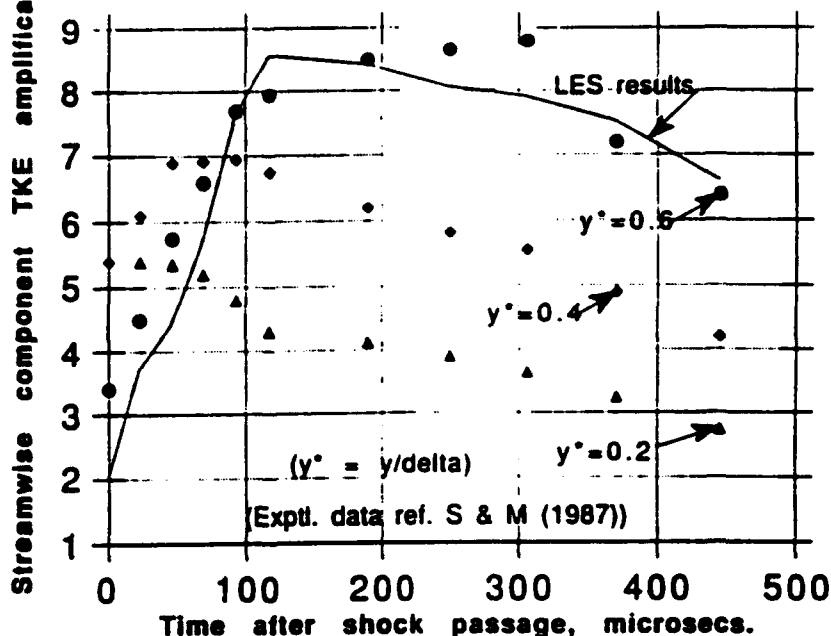


Figure 1. Comparison of current LES results with experiment [12]. Amplification of turbulent kinetic energy by shock boundary layer interaction in a 16 degree compression corner at Mach 2.7.

The result emphasizes the effectiveness of the viscoelastic shock response model in tracing the amplification and relaxation of the shocked turbulent field. At the same time, the results indicate the ineffectiveness of the implicit isotropic, statistically homogeneous, subgrid scale model used here when in the neighborhood of the strongly inhomogeneous, anisotropic wall influences.

Our focus, it must be remembered, is on developing an effective technique which automatically adjusts to the influence of both shock wave interactions and complicated boundary or interface geometries on turbulence. To this end, we implement and test a dynamically adjusted sub-grid scale model introduced by Germano, et al [13] and extended for compressibility by Moin et. al. [14]. These later developments are currently being evaluated as a means to automatically resolve features both in the immediate neighborhood of the shock front and the wall influence regions with concurrent attention to the influence of the unresolved scale stochastic backscatter on the resolved grid scale motions. [10].

Our current LES predictions [9, 10] (symbol B) are displayed in Figs. 2 and 3 together with those from the specialized, precise shock resolution studies of Rotman [3] (symbol R) which produced satisfactory comparisons to low Mach number shock tube experimental interaction results [3].

Figure 2 shows pre-shocked spectral distributions of power spectral density while Fig. 3 shows the post-shocked spectral distribution. The figures illustrate that predominant shock amplification and energy transfer occur at the low wave number (explicitly computable grid scale) dynamic range of greatest interest in both our LES development and our shock interaction analyses. For comparison, we also display low Mach number experimental shock turbulence interaction spectral distributions. These are taken from the speckle photographic experimental results for a reflected low Mach number plane shock passing back through grid-generated turbulence created in the wake of the incident shock phase [11] (symbol K & M).

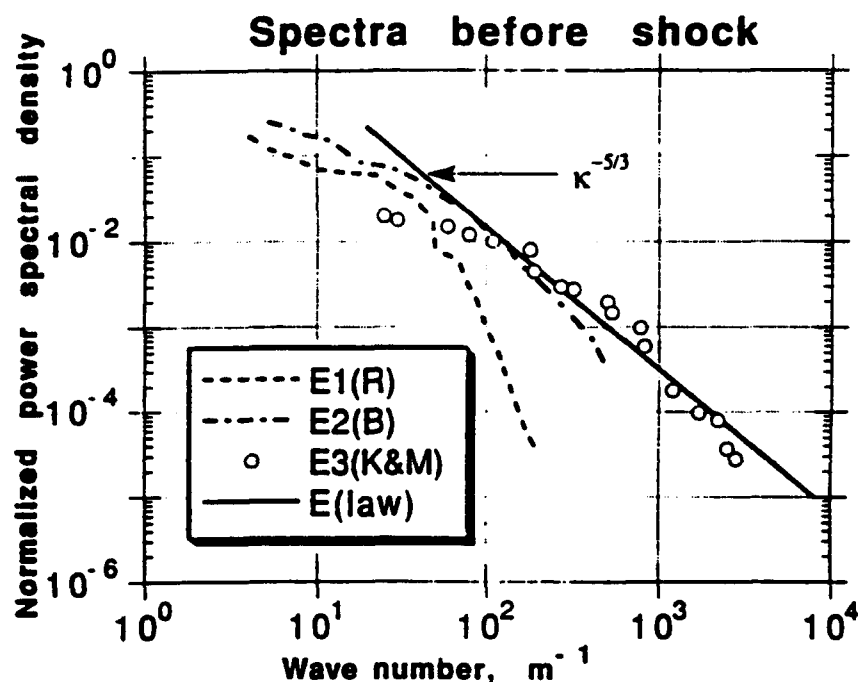


Figure 2. Comparison of pre-shocked normalized power spectral density distributions from current LES computations, previous computations [3] and shock tube reflected shock interaction experiments [11] at Mach 1.2.

While the Mach numbers, initial turbulent states, dynamic range, and gas composition were somewhat different in the two sets of computational simulations and the underlying experiments, for comparative purposes the results are rescaled and renormalized to individual peak values taken independently from each of the experimental or simulated trials. Specifically, all ordinate quantities plotted are power spectral density values vs wave number ratioed to the peak post-shocked decade value obtained for each individual experiment or simulation.

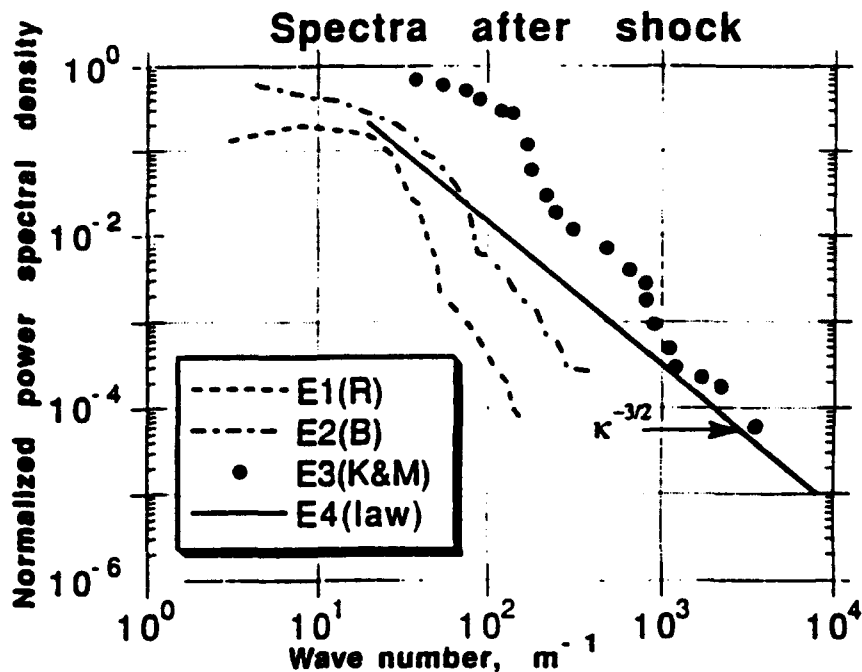


Figure 3. Comparison of post-shocked normalized power spectral density distributions from current LES computations, previous computations [3] and shock tube reflected shock interaction experiments [11] at Mach 1.2.

In Figs. 2 and 3, the Rotman results appear to show some evidence of very slight, late time computational dissipation in comparison to the current results. This may reflect the absence of explicit control by subgrid scale modeling. The integrated energy increase through shock interaction predicts an increase in the overall grid spectral energy content of about 20%, following shock transition. This is in reasonable agreement with the underlying experiments simulated [2].

The current LES results predict about an 85% increase in the energy content through shock amplification, while the experimental values at these flow conditions [11] reflect a measured increase of almost double this amount. The disparity is not considered crucial because of the limited dynamic range of the simulations in comparison to the experiments. Both experimental and computational cascades are seen to be somewhat steeper than the classical $\kappa^{-5/3}$ two dimensional spectral decay law, possibly reflecting some 3 dimensional influences in the experiments and some uncontrolled numerical dissipation in the simulations. Overall the behavior appears quite reasonable. We move on to even more promising results in the hypervelocity shock turbulence interaction range.

The most recent experiments [1], used as a primary data base for our latest LES developmental efforts, provide unique and remarkable

experimental evidence of the existence of pronounced interactive shock distortion and turbulent field alteration even for a very strong (Mach number > 100) spherical shock wave. The experimental findings appear to be well supported by our current LES simulations, created to assist in the interpretation and analysis of the experimental data. In our experiments, a 4-ns pulse from the 1.06- μm , 1 kJ Pharos III laser at the Naval Research Laboratory is focused onto the surface of a period-sized piece of target material placed in an ambient gas of optionally selected composition and background density. The laser heats the material to a few hundred eV, creating a powerful, miniature explosion. Depending on details of the experimental setup this explosion can initiate one or more shocks in the ambient gas as well as initiate the turbulent plume through which the shock propagates and interacts at a later stage.

Figures 4 and 5 illustrate the experimental pre-shocked and post shocked turbulent power spectral density distributions and the current LES simulation results. Amplification predictions, particularly in the dominant low wave number range, are seen to be even more satisfactory than in the previous low Mach number results. The experimental decay is steeper than the simulated decay in the inertial range reflecting an approach to three dimensionality (κ^{-3}) in spherical shock propagation experiments in contrast to the cylindrical

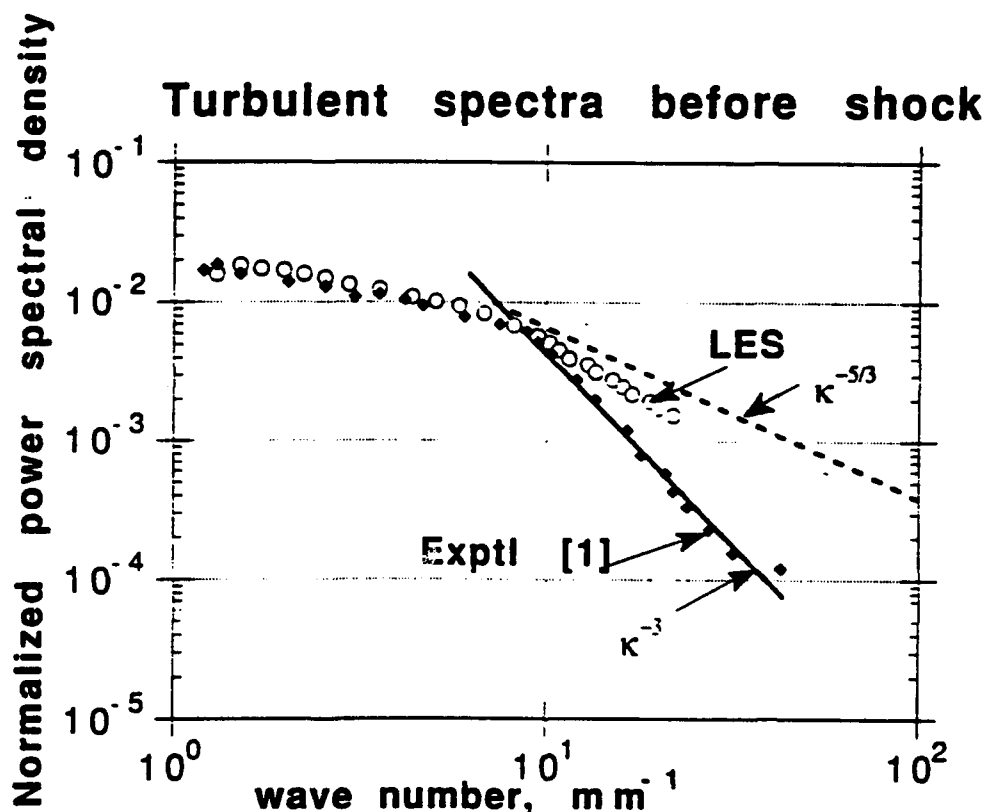


Figure 4. Comparison of pre-shocked normalized power spectral density distributions from current LES computations with laser target interaction hypervelocity experiments [1] at Mach numbers of the order of 100.

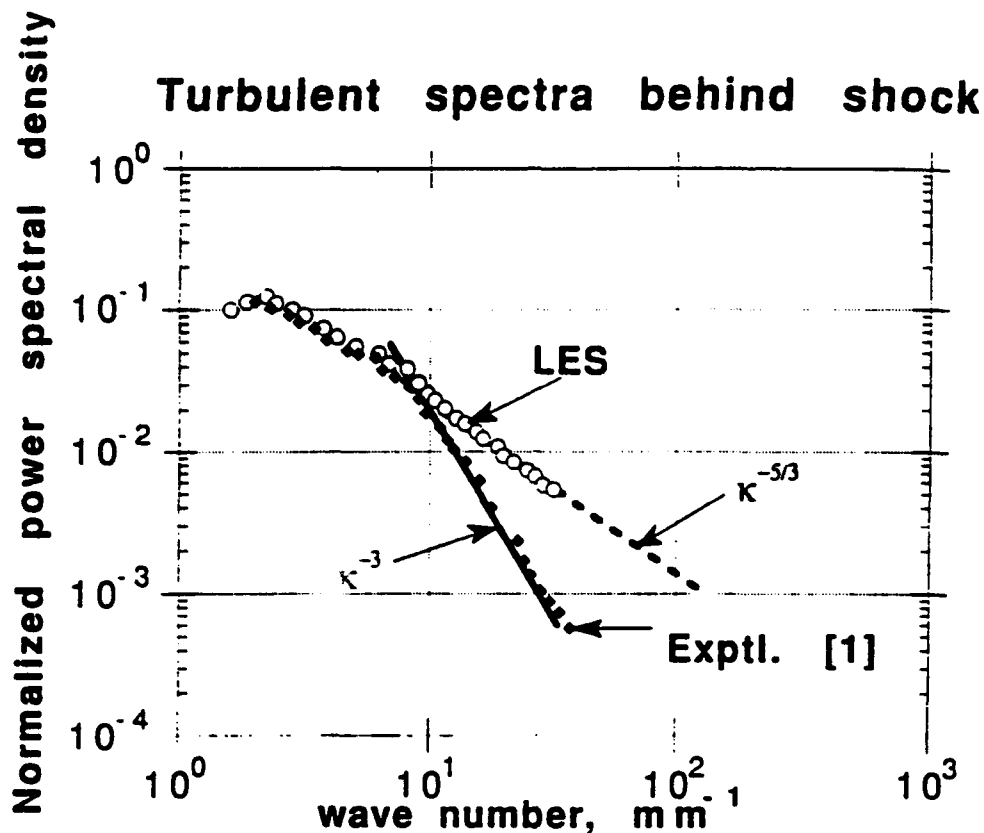


Figure 5. Comparison of post-shocked normalized power spectral density distributions from current LES computations with laser target interaction hypervelocity experiments [1] at Mach numbers of the order of 100.

geometry of the simulations which are seen to decay approximately at the classical ($\kappa^{-5/3}$) inertial distribution.

The shock amplification of the turbulence energy and the relaxation behind the shock as well as the distribution of the average integral scales of motion are displayed in Fig. 6, as a function of distance measured as fractions of shockwave radius of curvature. These distributions illustrate perhaps the most significant promise in the present stage of LES development for interaction analysis. The close parallel with the experimental results indicates that crucial information can be obtained from numerical simulations on the explicit grid scale range of motions, provided attention is given to properly modeling the influence of the non-resolved subgrid scale motions on the resolved motions. Variation in decay at substantial distance behind the shock is the result of physical differences between the LES conditions and the experimental situation. The experimental post shock decay is associated with a rapid depletion of sensible vapor matter near the origin. The rarefaction is not simulated in the LES results which were generated with a constant momentum reservoir during the test phase.

kinetic energy amplification and scale contraction through shock

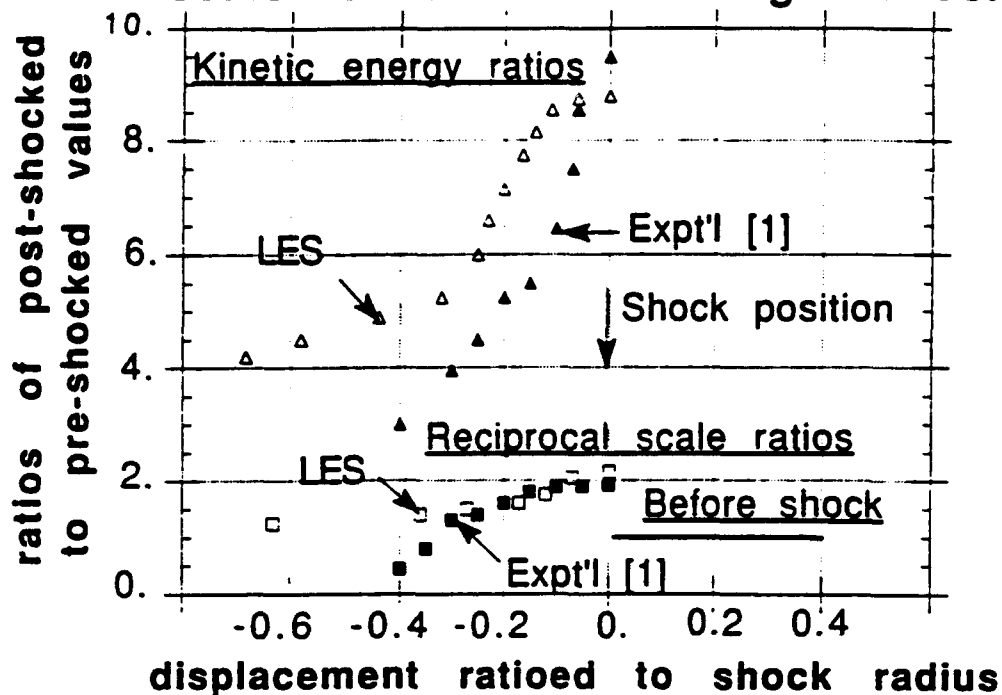


Figure 6. Comparison of turbulent kinetic energy amplification and correlation length scale contraction through and beyond shock interaction comparing current LES computations with hypervelocity experiments [1].

4. SUMMARY

These results, even though obtained at an early stage in the present trials and comparisons, seem to supply confirmation of the utility of a formal procedure for modeling the influence of the non-resolvable subgrid scales on the explicitly computed scales of motion. At the same time, however, recent applications of adaptive mesh refinement with the Godunov shock resolution schemes have produced much more highly resolved results including a well established inertial range and appropriate spectral decay, even in the absence of a sub-grid scale model formal procedure.

The mechanisms governing the influence of shock waves on turbulence are not well characterized and, it almost certainly follows, not well understood. Numerical simulations and appropriately designed experiments may help to reduce the uncertainty.

The Reynolds numbers for the particular flow circumstances and configurations of interest here discourage the use of direct numerical simulations. Hence, LES and selected supplemental computational techniques such as the direct Monte-Carlo shock structure simulation procedure applied at an earlier stage of this work are the tools of choice for augmenting and

analyzing the experimental data. The present effort focuses on current progress in developing an all-Reynolds number, compressible LES procedure that will provide a valuable tool in investigation of the underlying physical mechanisms that govern the interaction of shock waves and turbulence in the neighborhood of realistically complicated geometries.

5. ACKNOWLEDGMENTS

This is a report of work performed under the auspices of the U.S. Department of Energy by the Lawrence Livermore National Laboratory under Contract No. W-7405-Eng-48. The work of the second author was supported by the Office of Naval Research and the Defense Nuclear Agency. The first author gratefully acknowledges the ideas, comments and suggestions that were developed in discussions with C. E. Leith, D. A. Rotman, and W. P. Dannevik during the course of this work.

6. REFERENCES

1. GRUN, J., MANKA, C.K., RIPIN, B.H., BUCKINGHAM, A.C., RESNICK, J., and BURRIS, H.R. — Enhancement of Turbulence by a High Mach Number Shock, Bull. Am. Phys. Soc. Vol. 37, No. 6, p. 1478. (to be published), 1992.
2. HESSELINK, LAMBERTUS and STURTEVANT, BRADFORD — Propagation of Weak Shocks through a Random Media, J. Fluid Mech Vol. 196, p. 513, 1988.
4. COLELLA, PHILLIP and GLAZ, HARLAND M., J. Comp. Phys., Vol. 59, p. 264, 1985.
5. SMAGORINSKY, J., Mon. Weather Rev. Vol. 91, p. 99, 1963.
6. LEITH, C.E. — Stochastic Backscatter in a Subgrid-scale Model: Plane Shear Mixing Layer, Phys. Fluids, A Vol. 2, p. 297, 1990.
7. LEITH, C.E. — Stochastic Backscatter in a Subgrid-Scale Model: 3D Compressible Flows, International Workshop on Large Eddy Simulation, Eds. S. A. Orszag, T. A. Zang, Cambridge University Press, Cambridge, UK, 1993.
8. BUCKINGHAM, ALFRED C. — Numerical Studies of Shock Wave Structure Sensitivity to Interactions with Turbulent Fields, Numerical Methods in Laminar and Turbulent Flow, Vol. VI Part 1, Eds., C. Taylor, P. Gresho, R. L. Sani, J. Hauser, Pineridge Press, Swansea, UK, p. 805, 1989.
9. BUCKINGHAM, A.C. — Interactive Shock Structure Response to Passage through Turbulence, AIAA Paper 90-1642, AIAA 21st Fluid and Plasma Dynamics Conf., Seattle, WA, 18-20 June, 1990.

10. BUCKINGHAM, ALFRED C. — Large Eddy Simulation of Shockwave Passage through Turbulence, Proc. Symposium on Engineering Applications of Large-Eddy Simulations, ASME Fluids Engineering Summer Meeting, June 20-23, 1993, Washington DC. (MS in review, J. Fluids Engineering), 1993.
11. KELLER, J. and MERZKIRCH, W. — Interaction of a Normal Shock Wave with a Compressible Turbulent Flow, Experiments in Fluids, Vol. 8, p. 241, 1990.
12. SMITS, ALEXANDER J. and MUCK, KIN-CHOONG — Experimental Study of Three Shock Wave/Turbulent Boundary Layer Interactions, J. Fluid Mech. Vol. 182, p. 291, 1987.
13. GERMONO, M., PIOMELLI, U., MOIN, P., and CABOT, W. H. — A Dynamic Sub-grid Scale Eddy Viscosity Model, Phys. Fluids, A, Vol. 3, p.1760, 1991.
14. MOIN, P., SQUIRES, K., CABOT, W., and LEE, S. — A Dynamic Subgrid-scale Model for Compressible Turbulence and Scalar Transport Phys. Fluids, Ser. A Vol. 11, p. 2746, 1991.

**PHYSICS OF LASER-PRODUCED
INTERSTREAMING PLASMAS**

Laser Interaction and Related Plasma Phenomena, Vol. 7,
(Plenum Press, New York 1986, Editors: H. Hora and G. Miley)

PHYSICS OF LASER-PRODUCED INTERSTREAMING PLASMAS

B.N. Ripin, A.W. Ali, H.R. Griem, J. Grun, S.T. Kacenjar,
C.K. Manka², E.A. McLean, A.M. Mostovych, S.P. Obenschain,
and J.A. Stamper.

Naval Research Laboratory
Washington, D.C. 20375-5000

INTRODUCTION

The interaction of two interstreaming plasmas is of interest from several points of view. As a basic plasma physics topic, there are a myriad of possible collisionless and hydrodynamic instabilities that may occur when two beams interpenetrate. Some aspects of these instabilities are well established and have been observed, but others are poorly understood. Interpenetrating plasmas related to our choice of experimental parameters appear in several natural and man-made situations. The sun, for instance, emits a solar wind plasma which forms a flowing interplanetary drifting plasma with drift velocities in the hundreds of kilometer per second range; interestingly, laser-produced plasmas have comparable ablation velocities; laser-produced plasmas also stream from coronas having temperatures very close to the solar coronas (1-2keV). The solar wind interactions with the earth's magnetosphere and cometary plasmas have been observed to be very complex. An even more dramatic natural example of interacting energetic plasmas is a supernova explosion. Man-made counter streaming plasma situations also abound, e.g., in some proposed inertial confinement fusion reactors, theta pinch devices, ion beam ICF schemes, and in some ionospheric modifications.

We describe a laser-produced-plasma experiment which explores interstreaming plasma effects in both collisionless and collisional regimes. One of the plasma components consists of the ablation plasma from the Nd-laser solid-target interaction; the other plasma is formed by the photoionization of the ambient gas surrounding the target. An externally applied magnetic field can be applied across the interaction region.

We concentrate on the regime where the relative velocity of the two plasma components have Mach numbers (relative to either sound or Alfvén waves) much greater than one, and where one component is effectively unmagnetized while the other component may be magnetic field dominated. Instability boundaries, blast-wave behavior, and Rayleigh-Taylor effects are prime objectives of this study.

When two plasma components interpenetrate they stream freely through each other unless the collisional mean free path is short compared to the system size. Collisional coupling can occur through atomic, molecular, or nuclear collisions as well as between the various electron and ion

ponents. Collective plasma instabilities can cause an "effective" collision frequency even when ordinary collisions are not dominant. Beam-plasma instabilities can be of the bump-on-tail variety, where a small "beam" component sits on the wing of the dominant component near the phase velocity of plasma wave; ours is not this type. Our configuration is of the beam-beam type, illustrated in Figure 1, where the two counterstreaming plasma components have a large drift velocity compared to their thermal speeds.

Strong interaction between the two counterstreaming components is observed when the collisionality is high. In this case, strong energy- and-momentum-conserving shocks (also known as "blast-waves" or Sedov, Taylor, Von Neumann shocks) are formed. We verify that the system has many characteristics predicted by a simple blast-wave model, yet it also deviates from the simple model in many respects.

As the ambient plasma density is reduced, the system becomes collisionless and the coupling between the two plasma counterstreaming components tend to diminish. However, signatures of collective beam-plasma instability, probably the magnetized ion-ion (MII) instability, are seen in our experiments. Although the instability is weak under our conditions, it has the potential of being an effective momentum transfer mechanism between the energetic drifting plasma and the ambient plasma in the collisionless regime.

We describe the behavior of the interaction found experimentally and make comparisons where possible with theory and hydrodynamic code calculations.

EXPERIMENT

The experiment consists of focusing the beam from the NRL-Pharos II Nd-laser (1.05 μ m wavelength) onto small foil targets (≤ 1 mm dia, few-microns thick Al or CH) in the center of the target chamber. Typically, the laser pulse is a gaussian 4-ns FWHM 100 J pulse focused in the range of 10^{12} to 10^{14} W/cm². Target material is ablated by the laser irradiation and streams radially outward at high-velocity (20^o-100^o km/s). We call this plasma component the target-plasma. A low density background gas maintained in the chamber is promptly ionized in the vicinity of the target by radiation from the laser-target interaction (photoionization), and additionally, at later times by the expanding target-plasma (UV photoionization from the plasma shell emission or by particle impact). The background gas is usually nitrogen although gases from the hydrogen to Xe have also been used. This creates a stationary ambient plasma through which the high-velocity target-plasma streams; an external magnetic field is sometimes applied over the whole interaction region, using permanent magnets or helmholtz configuration coils. The spatial scale of the interaction region is centimeters, the time-scales involved are tens-of-nanoseconds, the magnetic fields, when applied, are in the kilogauss range, and the ambient gas pressures used are ten Torr (1 Torr = 1 mm of Hg = 3.24×10^{16} molec/cc) and below. Table I summarizes the experimental parameters and Figure 2 shows the experimental arrangement schematically.

DIAGNOSTICS

Many instruments are used to measure the evolution of the beam-plasma interaction. Diagnostics include: incident and reflected laser-beam energy calorimeters and time-resolving light-diodes to measure the time-history of the incident laser pulse. The angular distributions of the resulting target-plasma energy, velocity, mass, and momentum are obtained

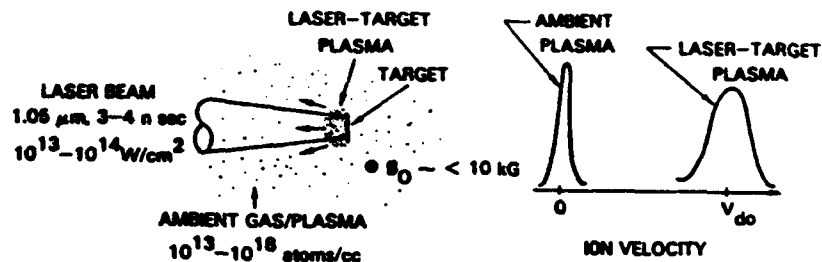


Figure 1. Schematic of the target-plasma shell moving outward from the laser focal region through a magnetized photoionized ambient gas (left). The ambient (stationary) plasma and drifting target-plasma (ablation) distributions form a classic interstreaming instability configuration (right).

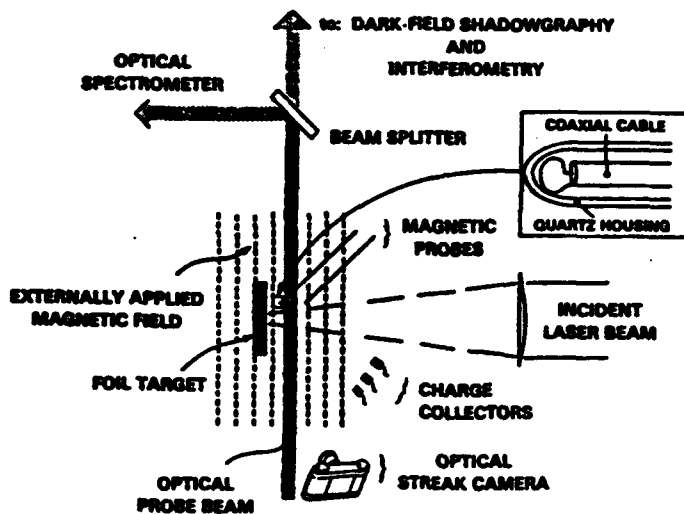


Figure 2. Experimental Arrangement

Table 1. Parameters used in laser-plasma counterstreaming experiment

<u>Laser:</u>	
Energy	1-400 J
Pulse Duration	4-ns FWHM
Irradiance	10^{12} - 10^{14} W/cm ²
<u>Ambient Gas:</u>	
Pressure	10^{-3} -10 Torr
Species	H, He, N ₂ , Ar, Ne, Air, Xe, Kr,...
<u>Target Plasma:</u>	
Initial Velocity	100-1000 Km/sec
Mass (A ₀)	0.1-1.0μgm
<u>Magnetic Field:</u>	0-1000 gauss

with arrays of mini-calorimeters, time-of-flight ion detectors, and light sensitive diodes.² Magnetic loop induction probes measure magnetic-field distortions in the target-plasma/ambient-plasma interaction region and any self-generated magnetic field components as a functions of position and time.³ Optical laser-probe diagnostics, such as dark-field, two-time shadowgraphy and interferometry, yield quantitative pictures of the plasma density structure at moderate-to-high densities ($> 10^{17}$ electrons per cm³).⁴ Laser scattering provides density and temperature information from Thomson scattering, as well as plasma fluctuation spectral information in the collective regime. Optical imaging with still photography, time-resolved framing photography, and streak photography also give qualitative and quantitative information on plasma properties and structure. Spectroscopy, from the infrared to XUV, is used to give spatially and temporally resolved information about the velocity, temperature, ionization state, density, emissivity, opacity, etc. of the target-plasma material, the photoionized background plasma, and the interaction between them.⁵ X-ray and XUV diagnostics allow diagnosis of plasma properties above 20 eV; X-ray pinhole photography gives two-dimensional spatially-resolved images while electronic x-ray and UV detectors give quantitative information about the initial plasma temperature, the radiant emission from the expanding target-plasma/ambient-plasma front. Tracer-dot techniques, in which small spots of a high-Z material are implanted in the target surface, have proved valuable in providing target-plasma flow visualizations and spatially resolved quantitative spectroscopy.⁶

PLASMA PROPERTIES

The laser-produced target-plasma conditions are characteristic of the steady-state laser-plasma ablation process.^{2,7} This plasma is well suited for this experiment since it has a reproducible single-peaked velocity distribution. The mean velocities of the ion distributions V_d , are tunable⁸ simply by varying the laser-irradiance I ; V_d varies with the 0.2 power of I . A good example of an ion time-of-flight trace, from which the velocity distribution of the target plasma can be determined, is shown in Figure 3. In addition, the velocity spread is relatively narrow, typically $\Delta V/V$ is about 0.25; $\Delta V/V$ is also tunable from 0.1 to 1 by increasing the focal spot diameter to pulse duration ratio.⁹ The mass ablation rate of the target plasma is also well-known, and goes as the 0.6 power of laser irradiance.

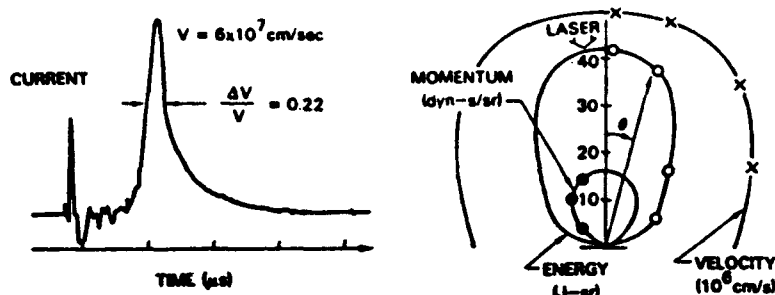


Figure 3. Laser target-plasma ion time-of-flight detector signal (left) and velocity, momentum and energy distributions (right). Note the high-velocity, narrow-velocity spread target-plasma. These ions contain over 80% of the absorbed laser energy.

The photoionized ambient plasma properties have been primarily determined by using plasma spectroscopic methods. These techniques have been described elsewhere.^{9,10} Typical ambient plasma temperatures are in the 1.5 to 2.5 eV range, depending upon the gas density. The degree of ionization is high near the laser-target focal region and decreases to a few tenths of a percent about 1-cm away. Of course, when the target plasma eventually streams through, the ambient properties change dramatically; these changes will be described in a later section.

COLLISIONAL INTERACTIONS

A strong shock forms when an energetic plasma burst expands supersonically into another plasma when the collision mean-free-path is small. The shock propagates into the ambient plasma, sweeping it up into a thin coupling shell, which consequently slows down due to the mass accretion. If the initial energy is released quickly compared to the time scales of interest and both particle energy and momentum are conserved, the resulting shock front is termed a Taylor-von-Neumann-Sedov shock or a "blast-wave."¹¹

In this section we review some features of the blast-wave model and use them to interpret the properties of coupling fronts observed in the experiment. We find good agreement between experimental results and most blast-wave theory.¹² However, in contrast to an ideal blast-wave, which is hydrodynamically stable, the shocks in the laser-experiment develop striking spatial structure, resembling arterial aneurysms, under certain circumstances. Causes of these nonuniformities are not yet isolated; none-the-less, we speculate on some possible responsible mechanisms.

The parameters used in the collisional regime experiments are included in Table I. Notice that the parameters were varied over a broad range to adequately test the blast-wave model scaling. Also, in some shots a 600 G magnetic field was applied over the interaction volume (transverse to the laser beam). However, no magnetic field dependence was seen in the collisional regime. Dark-field shadowgrams were taken of the shock structure at several times after the laser pulse. Spectroscopic observations were also made to determine the state (density and

temperature) of the ambient and coupled plasmas.

Stamper et al.¹³ has seen numerous examples of coupling shells (shock front), such as the one shown in Figure 4, taken with dual-time dark-field laser-probe shadowgraphy. These photographs indicate that the shells have the following general features:

- A thin ($\Delta R/R \approx 0.03$), approximately spherical shock is observed propagating into the ambient media at times long after the laser pulse has terminated.
- The shocks decelerate as they propagate away from the focal region.
- The velocity of the shock is a function of the deposited laser energy, ambient gas type and, of course, time; but the motion of the shell is insensitive to the initial target-plasma velocity.

However, the shocks also develop structure, such as shown in Figure 5, at the higher ambient pressures. We shall return to this point later. The unperturbed portions of these shells follow the same blast-wave scaling as totally unperturbed shells, but the spatial perturbations deviate from the blast-wave behavior.

The spectroscopic results indicate that the ambient plasma is initially weakly ionized (0.2%) at 1-2 eV, one-centimeter from the target surface. But when the blast-front arrives, the plasma becomes 100% ionized with a temperature of about 10 eV; the mass density jumps above the initial ambient level by a factor of 7-10 in the shock.

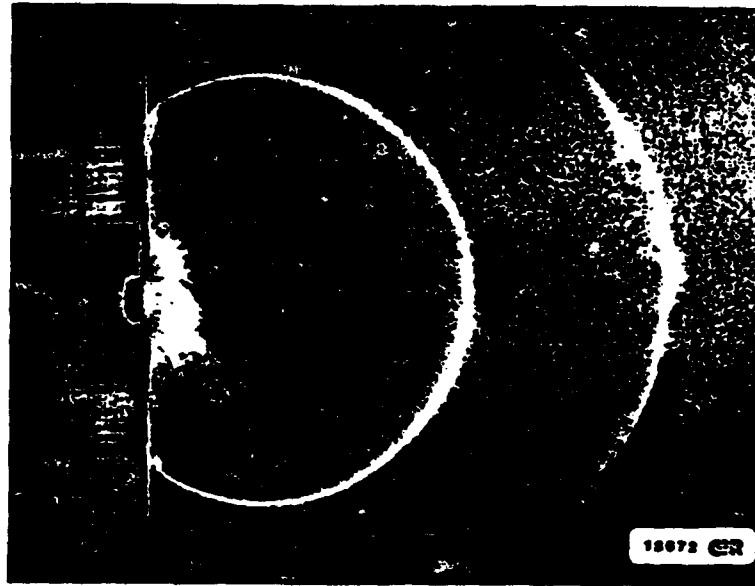


Figure 4. Dual-time dark-field shadowgram of shock waves at 52 and 96 nsec in 5 Torr N_2 gas. The incident laser energy was 4.1 J and the initial debris velocity was 2×10^7 cm/sec; $B=0$.



Figure 5. Dual-time dark-field shadowgrams of shockwaves with aneurisms. (Left) Shadowgram of a shock wave at 52 and 96 nsec in a 5 Torr ambient (90% N_2 + 10% H_2) gas. The laser energy was 38 J and the initial target-plasma speed was 5×10^7 cm/sec; $B=0$. Note the growing "aneurism" at the 4:00 pm position. The object on the right is a magnetic probe (out of focus). (Right) Shadowgram of shock fronts in a 1.5 Torr (N_2 + H_2) gas. The observation times were at 52 and 164 nsec, the incident laser energy was 20 J, the initial debris speed was approximately 3×10^7 cm/sec, and a 600 gauss magnetic field was present into the plane of the paper. The gaps in the target holders are about 5 mm.

We shall compare these experimental observations with a blast-wave model. After the initial energy release (laser-pulse), the plasma rapidly expands, picking up ambient media along the way. After the shell has accreted an ambient mass several times the initial target-plasma mass, the shell decelerates with the familiar self-similar blast-wave dependence $R=(E/\rho)^{1/5}t^{2/5}$. Eventually, when the shell velocity approaches the acoustic speed in the ambient media, the disturbance is no longer shock-treatments of blast-waves since Taylor, Von Neumann, and Sedov. Some of these works extend the theory into the initial phase, where the target-plasma mass is important, while others are hydrodynamic calculations. Here, we follow the method of Chernyi as outlined in Zeldovich and Raizer.¹¹ This blast-wave approximation has been shown to yield results within a few percent of exact treatments. The following assumptions are made: 1. The energy release is considered an instantaneous point explosion. 2. Spherical symmetry is assumed for simplicity. 3. The laser-target velocity and the resulting shock speeds are much larger than the undisturbed ambient sound speed. 4. The expansion conserves particle energy and momentum. 5. The ambient gas/plasma is swept up by the debris front into a thin cold shell having a mass large compared to that of the initial laser-target plasma. 6. The media is characterized by a constant effective ratio of specific heats γ . 7. Finally, counter-pressure due to the ambient plasma is neglected.

The shell front is a strong shock wave and the Hugoniot jump relations apply between the ambient media (ρ) and shell (ρ_s). The density jump is therefore given by

$$\frac{c_s}{c_{s0}} = \frac{\gamma+1}{\gamma-1} \quad (1)$$

The flow velocity behind the shock, u_s , is related to the shock speed V_s by

$$\frac{u_s}{V_s} = \frac{2}{\gamma+1} \quad (2)$$

giving the pressure within the shock,

$$P_s = \left(\frac{2}{\gamma+1}\right) \rho_0 V_s^2 \quad (3)$$

Now, combining these results of the strong shock jump relations with conservation of mass, energy and momentum we obtain many blast-wave properties. Conservation of mass is expressed by,

$$4\pi R^2 \Delta R \rho_s = \frac{4\pi R^3}{3} \rho_0 + (m_d) = M \quad (4)$$

The quantity on the left side of Eqn. (4) is the total shell mass as a function of shell radius R and shell thickness ΔR ; on the right side is the mass of ambient gas within the bubble volume (assumed to be completely swept up) plus the initial debris mass m_d (neglected here). The relative thickness of the shell is found by combining Eqn. (4) with Eqn. (1), i.e.,

$$\frac{\Delta R}{R} = \frac{1}{3} \frac{\gamma-1}{\gamma+1} \quad (5)$$

Proceeding further, conservation of momentum is expressed by,

$$\frac{d}{dt}(Mu_s) = 4\pi R^2 P_b \quad (6)$$

P_b is the pressure within the bubble volume which pushes outward on the shell. The shell is assumed to have most of the system mass, but some small amount of mass must remain inside the shell boundary (bubble). Finally, conservation of energy sets the energy in the explosion E equal to the sum of the shell kinetic energy plus the thermal energy invested in the system; this is expressed as:

$$E = \frac{1}{2} Mu_s^2 + \frac{1}{\gamma-1} \frac{4\pi R^3}{3} P_b + \left(\frac{1}{\gamma-1}\right) 4\pi R^2 \Delta R P_s \quad (7)$$

The first term on the right-hand-side of Eqn. (7) is the shell kinetic energy, the second and third terms are the thermal energies within the bubble and shell respectively. The last term (shell thermal energy) is usually neglected relative to the second term (bubble thermal energy) since the ratio is of order 10^{-1} . We make the same assumption here, however, note that these two contributions to the thermal energy become more comparable as ΔR increases, as P_b decreases, or in the event that the γ of the plasma in the bubble is higher than that of the shell (which

could be true since the bubble has a much hotter, lower-density plasma than the shell). This assumption about the apportionment of thermal energy does not change the blast-wave radius versus time scaling - only the constant of proportionality. We shall return to this point again. Demanding that the energy E be independent of radius throughout the expansion and assuming that $P_b = P_s$ gives a bubble pressure about half that of the shell pressure P_s , i.e.,

$$P_b = \frac{1}{2} P_s. \quad (8)$$

[This is to be compared to $P_b = 0.41 P_s$ for $\gamma = 1.2$ in the exact case.]

Now, from the above relations, the expression for the blast-wave radius with time similarity solution is

$$R(E, \rho_0, t) = \zeta_0 (E/\rho_0)^{1/5} t^{2/5}, \quad (9a)$$

or, in "practical" units,

$$R(\text{cm}) = 0.092 \zeta_0 [E(J)/(P(\text{Torr})/(MM/MM_{N_2}))]^{1/5} t(\text{nsec})^{2/5}, \quad (9b)$$

where (MM/MM_{N_2}) is the ratio of the ambient gas molecular weight relative to a nitrogen² molecule, and ζ_0 is a weak function of γ with a value of order unity. Within our set of assumptions, ζ_0 is given by the relation,

$$\zeta_0 = \left(\frac{75}{16\pi} \frac{(\gamma-1)(\gamma+1)^2}{(3\gamma-1)} \right)^{1/5}. \quad (10)$$

For completeness, we extend the treatment in Ref (11) to include the shell thermal energy in the energy balance [third term of Eqn. (7)].¹² We also allow for the γ of the plasma within the bubble to differ from the shell/ambient plasma γ by designating the bubble γ by γ_b and that of the remaining plasma by γ ; then Eqn. (10) becomes,

$$\zeta_0' = \left(\frac{75}{16\pi} \frac{(\gamma_b-1)(\gamma+1)^2}{4\gamma_b + \gamma - 3} \right)^{1/5}. \quad (10')$$

The ratio of inferred explosive energy release under the two sets of assumptions (ζ_0/ζ_0')¹³ can differ by about a factor of two although the maximum error in $R(t)$ is only 12%. It is clear that detailed hydrodynamic calculations which keep track of the local values of γ are necessary to get a precise description of the expansion. We use Eqn. (10) in the remainder of this paper.

The ratio of thermal energy to kinetic energy in the blast-wave system is surprisingly high; this ratio, obtained by taking the ratio of the second-term to first-term in Eqn. (7), is given approximately by

$$\frac{W_{TH}}{W_{KE}} = \frac{1}{2} \left(\frac{\gamma+1}{\gamma-1} \right). \quad (11)$$

[The right hand side of Eqn. (11) becomes $(1/2)[(\gamma+1)/(\gamma-1)]$ under the same set of assumptions as Eqn. (10').] Other relevant blast-wave parameters are the plasma effective γ and the temperature in the shell and in the bubble volume. The temperature in the shell can be estimated by using an approximation to c , the internal energy of air,¹¹

$$c = 8.3 T_s (\text{eV})^{1.5} (\rho_A/\rho_s)^{0.12} \text{ eV/molec.} \quad (12)$$

which is valid for temperature T_s between 1 and 25 eV, and density ρ_s between $10\rho_A$ (ρ_A = atmospheric density) and $10^{-3}/\rho_A$; γ ranges from 1.1 to 1.3 for air in this regime with $\gamma = 1.24$ a good effective value. The internal energy is also given by

$$c = \frac{1}{\gamma-1} \frac{P}{\rho} \quad (13a)$$

where P and ρ can be determined through Eqns. (1), (3), (8) or by direct measurement. In the shock front Eqn. (13a) becomes

$$c = \frac{2V_s^2}{(\gamma+1)^2} \text{ Joules per kg.} \quad (13b)$$

or, to obtain Eqn. (13b) in the same units as Eqn. (12), multiply by 0.334 x MW and express the shock speed V_s in units of (10^7 cm/sec) . Equating Eqn. (13a) to (12), with appropriate units, gives an estimate for T_s . The resulting expression for temperature in the shell is thereby found to be,¹²

$$T_s (\text{eV}) = 4.0 \times \left[\frac{V_s^2 (\times 10^7 \text{ cm/sec})^2 \text{ MW}}{(\gamma+1)^2 (\rho_A/\rho_s)^{0.12}} \right]^{2/3} \quad (14)$$

A tabulation of these blast-wave parameters is given in Table II for $\gamma = 1.2, 1.4, \text{ and } 5/3$. Note that, as assumed, most of the mass is in a very thin shell. Also, the high temperature within the bubble is a consequence of the approximate pressure balance with the shell (but with a much lower density). As we go towards the center of the bubble, the model predicts that the plasma density goes to zero as: $\rho = R^{-3/(\gamma-1)} t^{2/(\gamma-1)}$, and the temperature increases as: $T = R^{3/(\gamma-1)} t^{(2-\gamma)/(\gamma-1)}$.

Blast-wave Experiments

We now compare the experimental findings with the blast-wave model. The main observables in this experimental series, that we will relate to blast-wave theory are the shell position R , the thickness of the shell ΔR , and density ρ_s and temperature T_s of the shock wave. Experimental variables included: the laser energy, the laser focal spot size (and thereby the initial target-plasma velocity), the ambient gas type and pressure, the presence or absence of an external magnetic field, occasional variations in the target angle or structure, and the observation times.

Shell position and blast-wave scaling. A plot of the distance of the shock fronts from the target surface, R , for experimental shots which span the range of parameters tabulated in Table I, is shown in Figure 6; the variables along the abscissa of Figure 6 are scaled according to Eqn.

Table II. Variation of blast-wave parameters with effective γ .

Parameter	Relation	$\gamma=1.2$	$\gamma=1.4$	$\gamma=5/3$
ρ_s	$\gamma+1$	11	6	4
ρ_0	$\gamma-1$			
$\frac{\Delta R}{R}$	$\frac{1}{3} \frac{\gamma-1}{\gamma+1}$	0.03	0.06	0.08
$\frac{M_{TH}}{M_{KE}}$	$\frac{1}{2} \frac{\gamma+1}{\gamma-1}$	5.5	3	2
P_s	$\frac{2}{\gamma+1} \rho_0 V_s^2$	($\sim 10^3$ atmospheres at 7 Torr N_2 , $V_s = 100$ km/sec)		
$\frac{P_b}{P_s}$	1/2	0.4	0.35	
ζ_0	Eqn. (10)	0.89	1.01	1.12
ζ'_0	Eqn. (10'), $\gamma_0 = \gamma$	0.86	0.97	1.06

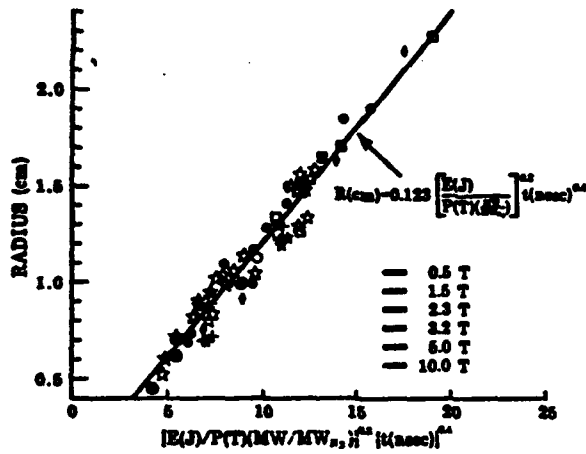


Figure 6. Plot of shock front positions R as a function of the normalized blast-wave scaling parameter for the data set in Table I. Note the excellent consistency with blast-wave scaling with $0.092 \zeta_0 = 0.123$.

(9b). Note the good agreement of the entire data set with the blast-wave scaling parameter $[(E/\rho_0)t^2]^{1/2}$, with a single universal constant of proportionality, $\tau_{0e} = 0.123/0.092 = 1.34$ (from Eqn. 9b).¹² The scaling is insensitive to the initial target-plasma velocity for constant incident laser energy.

It is possible to relate the experimentally observed τ_{0e} to theory τ_0 by taking into account the angular distributions of the plasma expansion. If we use the fact that half the laser-plasma energy is contained within a half-cone angle of 40° from the normal of the target in vacuum and assume that this angular distribution still holds true throughout the expansion (this may not be too bad an assumption since the flow is very supersonic), then we obtain an equivalent spherical experimental value for τ_0 of 1.0 ± 0.1 .

Coupling Efficiency. No distinct laser-target-plasma ion peak reaches our time-of-flight detectors at 2 Torr fill pressure, and most of the target-plasma ion peak is lost at 200 mTorr. We conclude, therefore, that the coupling between target-plasma and ambient plasma is high in this pressure regime, and nearly complete above 1 Torr.

The coupling efficiency, $E_{\text{plasma-wave}}/E_{\text{laser}}$, ambient pressure dependence can be inferred by fitting the radius-time observations to the blast-wave model and solving for $E = E_{\text{DW}}$ in Eqn. (9). Figure 7 shows the results for an initial target-plasma velocity of 4.5×10^7 cm/s streaming into nitrogen ambient plasma. The coupling efficiency drop below 1 Torr is roughly consistent with the loss of collisionality.

Shock Thickness. The shell thickness-to-radius ratio $\Delta R/R$ is observed to be about 0.03 ± 0.01 . In fact, the bright-dark-bright structure seen in the shock front shadowgrams are indicative of a steep gradient on both the front and back surfaces of the shell. This implies $\gamma = 1.20 \pm 0.07$ from Eqn. (5), a value consistent with both the determination from $R(t)$ (above) and $t_{\text{ion-of-state}}$ of air, Eqn. (12). Actually, the shell thickness is a relatively sensitive independent indicator of the effective γ ; for convenience, we invert Eqn. (5) and solve for γ , i.e.,

$$\gamma = \frac{1+3(\Delta R/R)}{1-3(\Delta R/R)} \quad (15)$$

McLean et al.⁵ uses results from spectroscopic continuum measurements to infer the density of the plasma within the shock front. Typical shell densities are found to be about 7 to 10 times the ambient N_2 density above 1 Torr fill pressure. The inferred γ from Eqn. (1), expressed by

$$\gamma = \frac{(\rho_s/\rho_0) + 1}{(\rho_s/\rho_0) - 1} \quad (16)$$

yields $\gamma = 1.18 \pm 0.04$ using the observed density jumps. Thus, the density jump at the shell is also consistent with a blast-wave with $\gamma = 1.2$ and the other experimental results.

Interferograms of the shock confirm the shock density jump obtained spectroscopically. Figure 8 shows such a shock profile obtained from interferometry. The interferograms also show behavior not predicted by the simple blast-wave model. Non-blast-wave features observed include: a density ramp and step in front of the steep shock bubble and higher than expected density inside the shock bubble.¹³ Moreover, aneurisms are

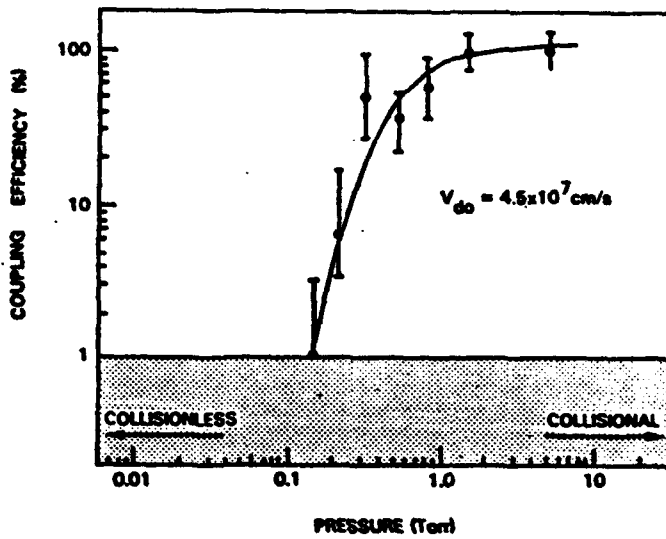


Figure 7. Coupling efficiency of the interaction between a 4.5×10^7 cm/s laser-target plasma and ambient nitrogen plasma.

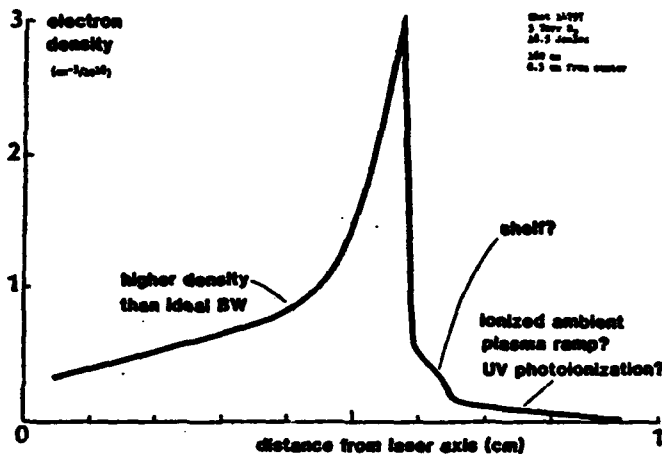


Figure 8. Electron-density shock profile obtained from an interferogram. Non-blast-wave like features are noted.

definitely not in the blast-wave model. Figure 9 shows another dual-time shadowgram showing further non-blast-wave features. In addition to the aneurism, considerable plasma turbulence or fluff, is seen to the rear of the target (away from the laser beam). This structure is probably caused by the disruption of the target material accelerated by the ablation-plasma. Note also in Fig. 9 that there is scattered laser-probe light in the bubble, on the inside of the blast-fronts; this is likely to be caused by short-wavelength plasma turbulence in the bubble.

Shock Temperatures. Shock front temperatures of 10-15 eV were estimated by McLean et al.⁵ from the highest ionization state of nitrogen observed. The temperature predicted within the shock front [using $\gamma = 1.2$, $\rho_2/\rho_1 = 100$, $MW = 28$, and typical shock speed at $R=1$ cm of $V_s = 1 \times 10^7$ cm/sec] in Eqn. (14)] is $T_s = 9$ eV. This is also in remarkable agreement with experiment.

The very low density plasma within the shell cavity, or bubble, should be at a much higher temperature than T_s . No measurement of T_b has yet been made. But, to estimate what to expect, we assume that the equation-of-state of this plasma continues to follow Eqn. (12) [not too likely since Eqn. (12) is based upon Saha equilibria and the bubble should be closer to coronal equilibrium], then the bubble temperature will be higher than the shell temperature by a factor of order $(\rho_2/\rho_1)^{0.6}$. This scaling was obtained by assuming pressure balance throughout the blast-wave system, which sets $c_p = \text{constant}$. A more accurate air/target-plasma equation-of-state for the bubble plasma is needed to make a better estimate. Measurement of T_b is an experimental challenge due to the low-density of the bubble plasma within the high-density shell.

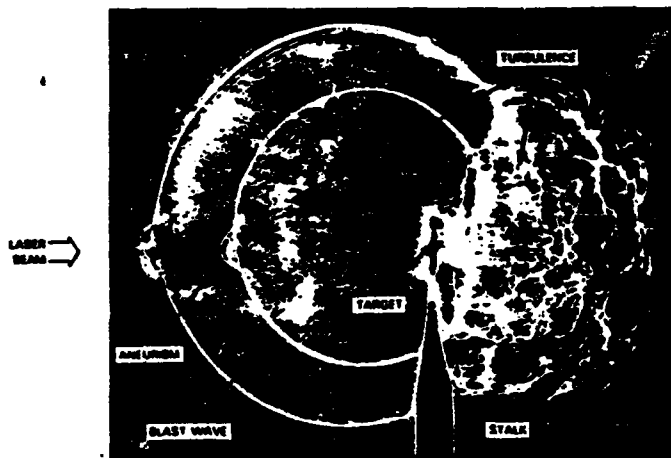


Figure 9. Dual-time shock-front shadowgrams (55 and 160 ns) of a 5T N_2 ambient shot with 36 J on a stalk mounted Al target. Note the blast-wave fronts and the non-blast-wave like turbulence and aneurism.

Shock Front Nonuniformities. What causes the shock front nonuniformities that are observed to develop in the experiment? Why are the "aneurism" nonuniformities, such as seen in Figures 5 and 9, so weird? To answer these questions we need inventive theory and experiments to eliminate or confirm mechanisms. Here are a few speculations.

Expanding ideal shock waves tend to be hydrodynamically stable, yet this statement has not, to our knowledge, been proven in general. If the shock fronts are Rayleigh-Taylor unstable for some reason, (caused by, for example, an adverse density gradient set up by radiation energy loss from within the swept up debris/ambient plasma) the growth-rates can be very large. For example, taking shell decelerations typical of the experiment ($g \sim 5 \times 10^{14}$ cm/sec²) and typical wavelengths observed ($\lambda \sim 3$ mm) yields growth rates, $\gamma_{RT} = (kg)^{1/2}$ of order 10^8 /sec, sufficient to create large nonuniformities within typical expansion times.

Another possible mechanism, target jetting, could cause aneurism-type protrusions.¹⁴ Bumps in the coupling front might occur due to the impact of slower target debris with the decelerated blast-wave. But, aneurisms still showed up in an experimental series using thin foils and limited mass targets which should have been completely ablated by the laser pulse, thereby eliminating a source of slower debris material. The aneurisms often occur outside the incident laser-beam path so that incident laser beam effects are excluded. Keskinen¹⁵ has proposed interesting asymmetrizing mechanisms caused by the self-generated magnetic fields that may be present during the initial expansion; these magnetic fields modify the flow patterns of the expanding debris plasma. A novel explanation by J. Giuliani,¹⁶ also employs the self-generated magnetic fields trapped inside of the shell. In this model hot plasma inside the bubble preferentially ablates the back of the central region of the blast-front near the axis of symmetry due to magnetic insulation off axis, thereby pushing out an aneurism near the target normal.

Other nonuniformity-inducing mechanisms are, no doubt, possible; a full understanding of this phenomena awaits further study. It is noted that some similar shock front nonuniformities have also been seen by others.¹⁷

We have seen that highly-coupled blast-waves are formed at pressures above 0.5 Torr in the laser-experiment. These shocks are thin ($\Delta R/R = 0.03$) dense ($\rho_2/\rho_1 = 10$) cool ($T_2 = 10$ eV) and exhibit many properties associated with energy- and momentum-conserving blast-wave. However, considerable non-ideal non-blast-wave features appear upon close inspection.

COLLISIONLESS INTERACTIONS

It is evident, from Figure 7, that the interaction between the fast laser-produced target-plasma and the stationary ambient plasma diminishes as the ambient pressure is reduced. This is primarily due to classical collision mean-free-paths becoming large compared to the interaction region and the two plasmas cease interacting. In this collisionless regime, however, plasma instabilities can occur and still cause momentum exchange between the two plasma components; this gives an effectively higher, or "anomalous", collision frequency.

In our first experiments in the low-pressure (<200 mTorr) regime, we searched for signs of beam-plasma instabilities. Five streaming instabilities are thought to be potentially important in our experimental regime;¹⁸ these instabilities are: the magnetized and unmagnetized ion-ion, modified two-stream, ion sound, and beam cyclotron instabilities. We

Focus our attention on the magnetized ion-ion (MII) instability. The magnetized ion-ion instability is an efficient momentum transfer mechanism with an effective collision frequency of about one-tenth the lower hybrid frequency.

We are in a regime in which the target plasma ions are unmagnetized (cyclotron radius \gg equal mass radius), the ambient plasma is magnetized (electron and ion cyclotron radii $<$ the equal mass radius), and, most importantly, the target-plasma magnetic Mach number is high ($V_D > V_{\text{Alfven}}$).

The uncoupled target-plasma ion distribution has high-velocity (up to 8×10^7 cm/sec) and a narrow spread as noted previously. Thus, the relative velocity between target-plasma and ambient ion distributions exceeds the thermal speeds of the beams, satisfying one of the criteria for streaming instability.

Residual Collisions. When no magnetic field is applied, but ambient gas is present below 80 millitorr, the target-plasma ion distributions are not generally altered. For ambient pressures of 80 millitorr and up, the target-plasma ion distributions reaching the time-of-flight detector (about 22 cm away from the target) are somewhat attenuated and broadened. These pressure effects on the target-plasma velocity ions distribution are thought to be due to collisional processes, such as charge exchange, since they do not seem sensitive to the presence or absence of a magnetic field (at least not sensitive to fields below one-kilogauss).

This hypothesis was confirmed by using three time-of-flight charge collector detectors placed 10, 25, and 55 centimeters from the target, to detect the ion distribution changes occurring between them.

One question is whether we can rely upon the preservation of the shape of the ion distribution in passing through the ambient media? If so we can detect the effects of an interaction occurring within a few centimeters of the target much further away. The answer is yes, at least through mass-pathlength of 5×10^{16} molecules/cc \cdot cm (i.e., 150 μ Torr N_2 with $l = 10$ cm). In this range, neither the peak velocity nor the velocity spreads are strongly affected. Therefore, the ion time-of-flight traces can be used as good indicators of interactions close to the target.

Some energy, albeit a small amount, is transferred from the target plasma to the ambient-plasma in the 100 μ Torr regime; this is observed in the framing camera pictures of visible light emission. A fuzzy shell expands with a speed of about 250 km/sec into a 100 μ Torr N_2 background gas.

Measurements of the magnetic field dynamics show that ambient field is largely swept out of the region traversed by the target plasma and is compressed ahead of it, as illustrated in Fig. 10. An extensive description of the magnetic field behavior is to be found in papers by Kacemjar, et al.^{3,19}

Magnetized ion-ion instability. For what experimental parameters is the magnetized ion-ion instability most likely to be observed? To answer this question we examine the instability criteria outlined in Lampe et al.¹⁸ The two most stringent instability criteria are that of avoiding electromagnetic stabilization ($V_D/V_A = M < 2.5$) and fitting at least one parallel wavelength in the system size ($\lambda_{11} < 2\pi R_M$).

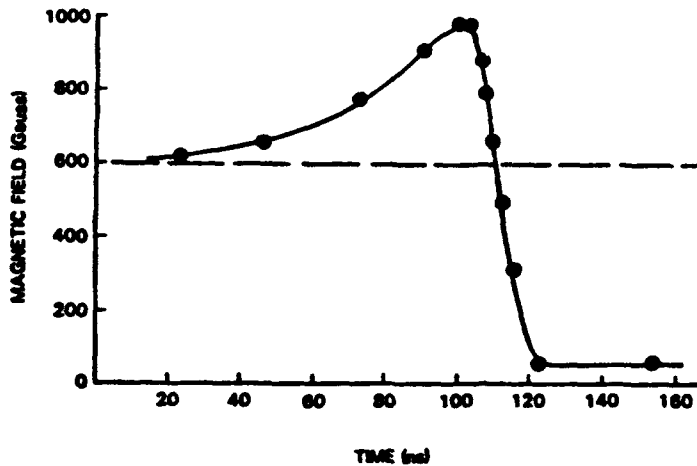


Figure 10. Temporal behavior of the change in magnetic field detected by a magnetic loop probe located 3 cm from the target. The applied field was 600 gauss. Note the field compression peak at 100 nsec and near depletion of the applied field (magnetic bubble) for $t > 120$ nsec. (Ambient gas was 5 mTorr hydrogen; laser energy was 7.7 J)

Smith and Huba²⁰ quantitatively delineated expected regions of instability in laser energy-ambient pressure space, as illustrated in Figure 11.

To detect the presence of instability, an array of four ion time-of-flight detectors is deployed perpendicular to the magnetic field direction, but at various angles from the target normal.

A clear difference between the target plasma ion distributions with and without the magnetic field is seen in Fig. 12. Without a field present, as in the ion distributions on the left side of Fig. 12, the ion distributions are well-behaved and similar to those generated in a vacuum. In contrast, the distributions in the presence of the magnetic field (on the right) are broadened and have lower velocity (later-time) peaks which are like the expected signatures of beam-plasma instability. The pressure is very low and collisions play little or no role. (We used hydrogen gas to have a low ambient-plasma atomic number in order to be more susceptible to instability.) To test the conjecture that raising the ratio of drift velocity to Alfvén velocity above about 2.5 quenches the instability. We compared ion distributions resulting from use of nitrogen ($V_D/V_A = 4$) and hydrogen ($V_D/V_A = 1$), as shown in Fig. 13. The magnetic field dependent interaction that occurs in hydrogen is not seen in nitrogen. This lends support to the notion that MII may be occurring in the carbon-hydrogen combination but not in carbon-nitrogen under otherwise identical conditions, due to the electromagnetic stabilization criteria.

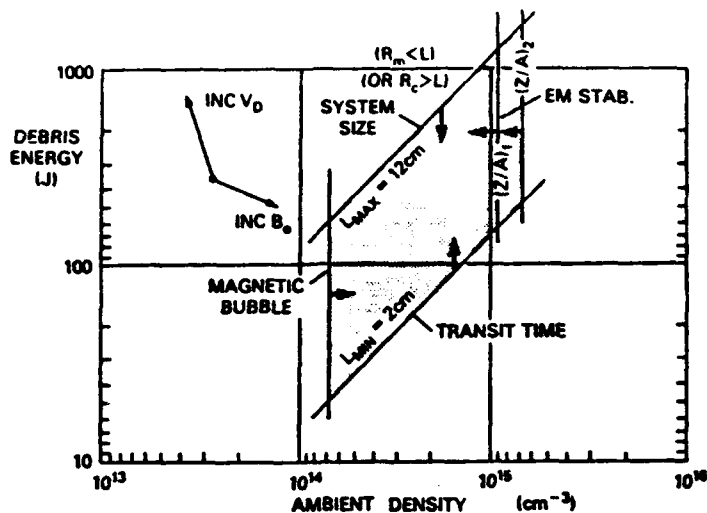


Figure 11. Magnetic ion-ion instability window (qualitative). The unstable region is bounded on the right by electromagnetic stabilization when $V_D > 2.5 V_A$, on the left by the requirement that the energy density in the target-plasma exceed that of the magnetic field, on the bottom by requiring that the transit-time of an ambient ion passing through the shell exceed one momentum transfer e -fold, and bounded on the top by the practical requirement that the equal mass radius fit inside the experiment. The top can also be limited by the cyclotron radius of the debris ions at high field strengths.

Finally, sometimes ion signals are observed with components having higher velocities than in the original target-plasma distributions. This occurs at low incident laser energy in cases which exhibit the other signs of magnetic field dependent interaction. We have very few examples of these accelerated ions, and, therefore the results are considered tentative. But, these "fast ions" may be the result of a reflection or acceleration process near the coupling region.

SUMMARY

The laser-target counterstreaming plasma experiment shows interactions in both the collisional (high-pressure) regime and the collisionless (low-pressure) regime.

The bulk of our experimental work has been in the collisional regime. Here, we increase the ambient pressure in the experiment into the hundreds to thousands of millitorr pressure range. Well-formed Taylor-Von-Neumann-Sedov shocks (or "blast-waves") are formed when the expanding target-plasma sweeps up the ambient plasma. The blast-wave radius versus

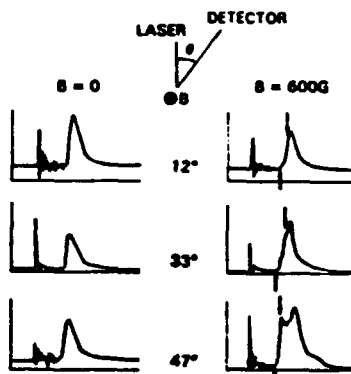


Figure 12. Comparison of target-plasma ion time-of-flight traces without a magnetic field present (left) and with a 600 G field present (right). Note the distorted debris distributions in the presence of a magnetic field. (Both cases had hydrogen ambient gas at 15 mTorr; shot on left had 7.4 J laser energy while that on right had 8.6 J).

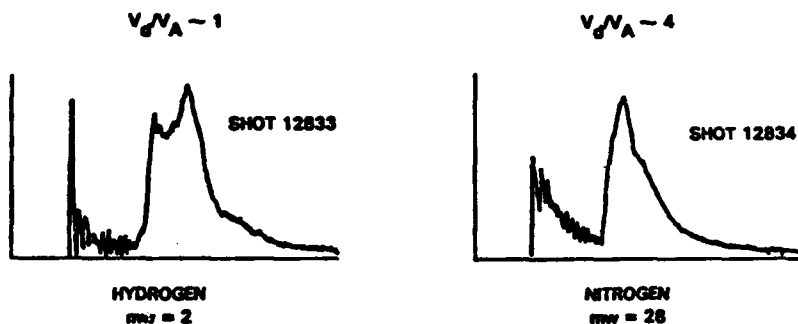


Figure 13. Comparison of target-plasma ion distributions with atomic number of the background gas. ($B_0 = 600$ G, $n_1 = 0.01$, $n_0 = 6 \times 10^{12}$ ions/cc, and $V_d = 4 \times 10^7$ cm/s; $E_L = 8$ J; ion detector at 47°)

Time dependence follows the classic blast-wave theory over a broad range of operating parameters. The coupling shells in this regime also satisfy other predictions of blast-wave theory such as the temperature and density jumps. But, the fraction of the target-plasma energy actually coupled into the blast-wave system falls off rapidly below about 500 mTorr pressure (for ions with an initial speed of 450 km/s).

However, in addition to smooth classic blast-wave shock regions, features are observed which are not included in simple blast-wave models, i.e., the aneurisms, fluff to the rear of the target, and unresolved turbulence inside the blast-front. The mechanisms causing this structure are still under active investigation. Other non-blast-wave-like features observed include: a higher density inside the bubble than expected and an electron density ramp and ledge in front of the shock.

Another area in which very good progress has been made experimentally and theoretically is in describing the dynamics of the magnetic field under the influence of the expanding target-plasma and shock fronts. It has been established that the uncoupled target-plasma compresses some of the external magnetic field ahead of it. Also, in very recent experimental runs, additional compression due to the blast-wave is observed.

In the collisionless regime, the experiments show magnetic field dependent interactions between the fast target ions and ambient plasma. In many ways these observations are similar to those expected from the magnetized ion-ion instability.

ACKNOWLEDGEMENTS

The authors thank contributions from L. Daniels, V. Salzman, M. Nocerino and D. Carpentier. This work was sponsored by the Defense Nuclear Agency under task order W99QMXWA and task order number 00011.

REFERENCES

- a. Sam Houston State University, Huntsville, TX 77341.
1. G. Taylor, Proc. Roy. Soc. A201, 159 (1950) and A201, 175 (1950).
J. von Neumann and R.D. Richmyer, J. Appl. Phys. 21, 232 (1950); and H.H. Goldstine and J. von Neumann, Comm. Pure Appl. Math, VIII 327 (1955).
L.I. Sedov, "Similarity and Dimensional Methods in Mechanics," (Academic Press, NY, 1959, ed. M. Holt).
2. B.H. Ripin, R.R. Whitlock, F.C. Young, S.P. Obenschain, E.A. McLean, and R. Decoste, Phys. Rev. Lett. 43, 350 (1979); also see B.H. Ripin et al., Phys. Fluids 23, 1012 (1980) and 24, 990 (1981).
3. S.T. Kacendar, B.H. Ripin, J.A. Stamper, J. Grun, and E.A. McLean, NRL Memo Report #5260 (1984).
4. J.A. Stamper, B.H. Ripin, E.A. McLean, and S.P. Obenschain, NRL Memo Report #5278 (1984).
5. E.A. McLean, J.A. Stamper, H.R. Griem, A.W. Ali, B.H. Ripin, and C.K. Manka, NRL Memo Report #5274 (1984).
6. M.J. Herbst and J. Grun, Phys. Fluids 24, 1917 (1981);
M.J. Herbst et al. NRL Memo Report #4893 (1980) and #5003 (1983)
see also, M.J. Herbst et al., "Laser Interaction and Related Plasma Phenomena, Vol. 6," pgs. 317-334. eds. H. Hora and C. Miley, Plenum Press (1984).

7. J. Grun, S.P. Obenschain, B.H. Ripin, R.R. Whitlock, E.A. McLean, J. Gardner, M.J. Herbsi, and J.A. Stamper, *Phys. Fluids* 26, 588 (1983).
8. J. Grun, R. Decoste, B.H. Ripin, and J. Gardner, *Appl. Phys. Lett.* 39, 545 (1981).
9. J. Grun, R. Stellingwerf, and B.H. Ripin, to appear in *Phys. Fluids* (1986).
10. A.W. Ali and E.A. McLean, *J. Quant. Spect. Rad. Trans.* 33, 381 (1985).
11. Y.B. Zel'dovich and Y.P. Raizer, "Physics of Shock Waves and High Temperature Hydrodynamic Phenomena, Vol. 1," (Academic Press, NY, 1966).
12. B.H. Ripin, J.A. Stamper, and E.A. McLean, *NRL Memo Report* 5279 (1984).
13. J.A. Stamper, C.K. Manka, E.A. McLean, A.N. Mostovych, S.P. Obenschain, and B.H. Ripin, (to be published).
14. C. Longmire, (private communication).
15. M. Keskinen, (private communication).
16. J. Giuliani, *NRL Memo Report* #5420 (1984).
17. G.V. Sklizkov, in "Laser Interaction and Related Plasma Phenomena, Vol.1" pg. 235, eds. H. Schwarz and H. Hora, *Plenum Press, NY* (1971).
- M.G. Basov et al., in "Laser Interaction and Related Plasma Phenomena, Vol 3B," pg. 553, eds. H. Schwarz and H. Hora, *Plenum Press, NY* (1974).
- D.M. Wilke, *Los Alamos Report* LA-9182-T (1982).
18. M. Lampe, W.H. Manheimer, and K. Papadopoulos, *NRL Memo Report* #3076 (1975).
19. S.T. Kacenjar, M. Hausman, M. Keskinen, A.W. Ali, J. Grun, C. Manka, E.A. McLean, and B.H. Ripin, to appear in *Phys. Fluids* (1986).
20. R. Smith, and J. Huba, *NRL Memo Report* #5092 (1983).

**INSTABILITY OF TAYLOR-SEDOV BLAST WAVES
PROPAGATING THROUGH A UNIFORM GAS**

Instability of Taylor-Sedov Blast Waves Propagating through a Uniform Gas

J. Grun, J. Stamper,^(a) C. Manka, J. Resnick,^(b) R. Burris,^(c) J. Crawford,^(d) and B. H. Ripin
Space Plasma Branch, Plasma Physics Division, Naval Research Laboratory, Washington, D.C. 20375-5000
 (Received 10 January 1991)

We present the first measurements of an instability in Taylor-Sedov blast waves propagating through a uniform gas. The instability occurred in a gas whose adiabatic index was low. Amplitude perturbations grew as a power of time. Our observations are compared to theory.

PACS numbers: 47.40.Nm, 28.70.+y, 47.20.-k, 52.35.Tc

Blast-wave instability may contribute to the structuring observed in supernovae and play a role in the formation of stars and galaxies.¹ Unfortunately, knowledge of blast-wave instabilities is based almost entirely on theoretical considerations, and these have been accompanied by considerable controversy.²⁻⁴ Unstable blast waves had not been observed experimentally, leading some to conclude that blast waves must be stable.³

We present the first measurements of an instability in Taylor-Sedov blast waves⁵ propagating through a uniform gas. The instability occurred in an ambient gas whose adiabatic index γ was a low 1.06 ± 0.02 . Perturbations grew as a power of time. Our observations are compared to a theory described in papers by Vishniac and Ryu.⁴

Blast waves, in our experiment, are produced by the expansion of ablation plasma from the surface of laser-irradiated foils into an ambient gas (Fig. 1). A 6- μm -thick polystyrene foil is placed in a chamber which is first evacuated and then filled to 5-torr pressure of nitrogen or xenon gas. The foil surface is heated⁶ to about 800 eV with a 200-J, 1.054- μm , 5-ns pulse from the Pharos III Nd-glass laser, which is focused to a 3-TW/cm², 880- μm -diam spot. Ablation plasma from the hot foil surface propagates supersonically into the background gas⁷ at about 700 km/s and, much like the products of a chemical explosion, forms a blast wave. (Simultaneously, the background gas is photoionized by radiation from the vicinity of the laser's focal point.)

We have verified through extensive experimentation that this laser-ablation method forms classical Taylor-Sedov blast waves when the interaction between the ablation plasma and the gas is collisional, and when the mass of the swept-up ambient gas is greater than the mass of the ablation plasma.⁸ For nitrogen, collisional coupling occurs at gas pressures exceeding 0.5 torr.

Blast-front structure is photographed using the well-known dark-field imaging method, which is sensitive to the square of fluctuations in the index of refraction. In our implementation, a 0.53- μm , <1-ns-duration, 5-cm-diam, few-mJ laser probe illuminates the blast wave side-on. Electron-density gradients within the blast wave deflect a part of the probe while the remainder passes through undisturbed. The probe beam emerging from the blast-wave region is then relayed onto a film surface with a telescope. A stop placed at a focal point inside the telescope blocks the undisturbed component of the probe light but passes the deflected part, thereby forming an image in which fluctuations in the index of refraction (and hence electron density) appear as bright features on a dark background.

In addition, visible emission from the blast front is photographed with a very fast (120-ps to 5-ns gate time), four-frame, microchannel-plate intensifier camera. This, together with the dark-field image, provides five photographs per shot of the blast wave at different times in its evolution. The dynamics of the blast wave are reconstructed by combining the results of dark-field and emission photographs taken at different times on individual and multiple shots. Also, the spectrum of light emitted by the ambient gas before and after the passage of the blast wave is measured with temporal and spatial resolution. To do this, we image a 3-mm-diam spot in front of the foil onto the slit of a spectrometer and record the resulting spectrum with a streak camera.

We find that Taylor-Sedov blast waves formed in nitrogen gas are always stable and smooth—like the example in Fig. 2(a). In startling contrast [Fig. 2(b)], the surface of the blast fronts launched into an ambient xenon gas is wrinkled like a dried prune. This wrinkling is quantified by tracing and then Fourier transforming⁹ the outer edge of the front, which is equivalent to looking at the projection onto a plane of the edge of an unstable

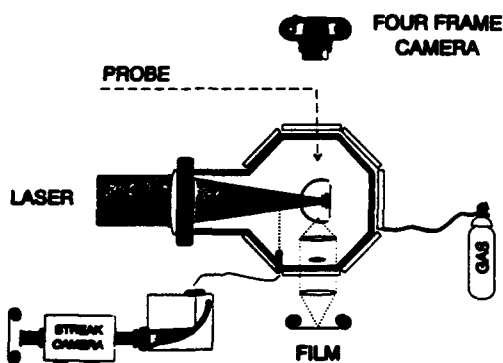


FIG. 1. Experimental setup.

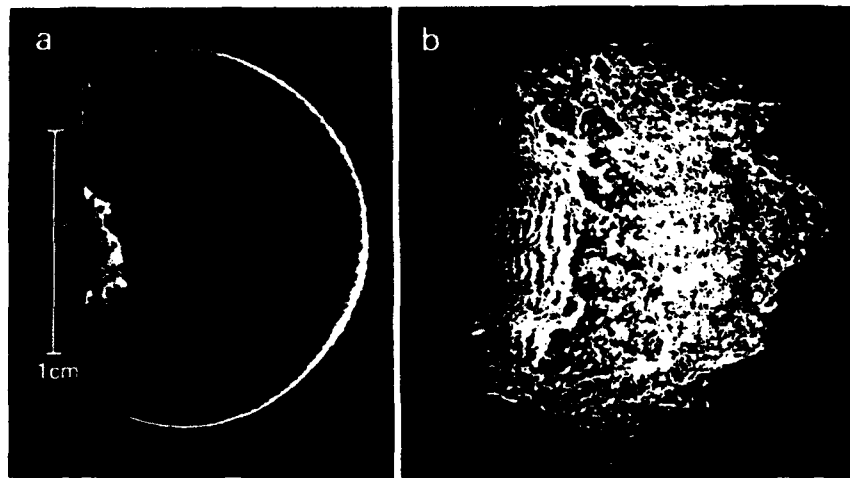


FIG. 2. Dark-field shadowgraph of (a) a stable blast wave in nitrogen gas, and (b) an unstable blast wave in xenon gas (at 243 ns).

sphere. The results are presented as $A_t(k)/R$ vs $\log_{10}(kR)$, where $A_t(k)$ is the full amplitude of the mode with wave number k at time t , and R is the average radius of the blast-front boundary.

The blast-wave trajectory in xenon and the evolution of instability amplitude $A_t(k)/R$ are shown in Fig. 3. From 6 to 18 ns the front moves at a constant speed corresponding to the velocity of the ablation plasma, a blast wave not yet having formed. The front is slightly structured, but these nonuniformities do not grow. By 25 ns a blast wave propagating with the $t^{2/5}$ Taylor-Sedov dependence has formed. Now the surface becomes significantly more wrinkled and spikelike protuberances shoot ahead of the front: $A_t(k)/R$ increases as a power of time until 300 ns. It is noted that the blast wave does not fall apart or otherwise dissipate, but propagates as a shocklike, albeit structured, front. As the protuberances get larger they become increasingly more difficult to observe. By 400 ns they are not seen at all and the blast wave takes on the appearance of a slightly structured but basically stable shock.

A power law of the form $A_t(k)/R \cong t^{S(kR)}$ was fitted to the $A_t(k)/R$ -vs-time data during the period of growth, with the results shown in Fig. 3(c). We find clear growth for modes satisfying $0.7 < \ln(kR) < 2$. Maximum growth occurs at $\ln(kR) = 1$, where $S = 1.6$, and minimum growth, with $S = 0.3$, occurs at $\ln(kR) = 2$. The fit by a power law is very good (correlation > 0.7) for $\ln(kR) < 1.5$, but worse (i.e., data are more noisy) for larger values of $\ln(kR)$. Noise may be the reason why $S(kR)$ stays clamped at 0.3 for $2 < \ln(kR) < 3$ and does not decrease to zero.

A basic difference between stable blast waves in nitrogen and unstable blast waves in xenon is that the former propagate in a gas with adiabatic index $\gamma_N = 1.3 \pm 0.1$, and the latter in a gas with $\gamma_{Xe} = 1.06 \pm 0.02$. To derive γ_{Xe} we utilize the observation that blast waves in nitro-

gen and xenon propagate according to the Taylor-Sedov blast-wave relation¹⁰

$$d \propto \left(\frac{75(\gamma-1)(\gamma+1)^2}{16\pi(3\gamma-1)\rho_0} \right)^{1/5} t^{2/5},$$

where d is the distance between the focal spot and the blast-wave front and ρ_0 is the gas mass density. Therefore, by dividing the measured d in nitrogen by the measured d in xenon at any given time we arrive at a relationship between γ_{Xe} , γ_N , and the mass of each gas species. Solving numerically for γ_{Xe} as a function of γ_N , we find that as γ_N varies from 1 to $\frac{5}{3}$, γ_{Xe} varies from 1 to 1.13. Hence, for any reasonable value of γ_N the value of γ_{Xe} is less than 1.13. In past experiments⁸ we have measured γ_N to be 1.3 ± 0.1 , which implies that $\gamma_{Xe} = 1.06 \pm 0.02$.

γ_{Xe} is lower than γ_N because prior to the arrival of the blast wave xenon gas radiates much more than nitrogen gas. (Radiation increases the degrees of freedom within a gas and hence reduces its effective γ .) This is demonstrated by examining the spectrum of light emanating from a spot in front of the laser's focal point [Fig. 3(d)]. In nitrogen gas the laser-induced explosion produces little measurable emission prior to the arrival of the blast wave. Immediately before the blast wave arrives at the observation point there is a slight increase of N^{1+} and N^{2+} lines: These lines are probably excited by UV or heat from the blast wave. When the blast front arrives, there is a sudden increase in emission from the N^{1+} , N^{2+} , and target C^{2+} lines, as well as an increase in continuum emission. In contrast, xenon emits copiously in many Xe^{1+} and some Xe^{2+} lines from the moment the laser strikes the foil. Arrival of the unstable blast wave is signaled by a more gradual increase in continuum emission, but line emission is not changed significantly. We conclude, therefore, that it is the radiation in xenon

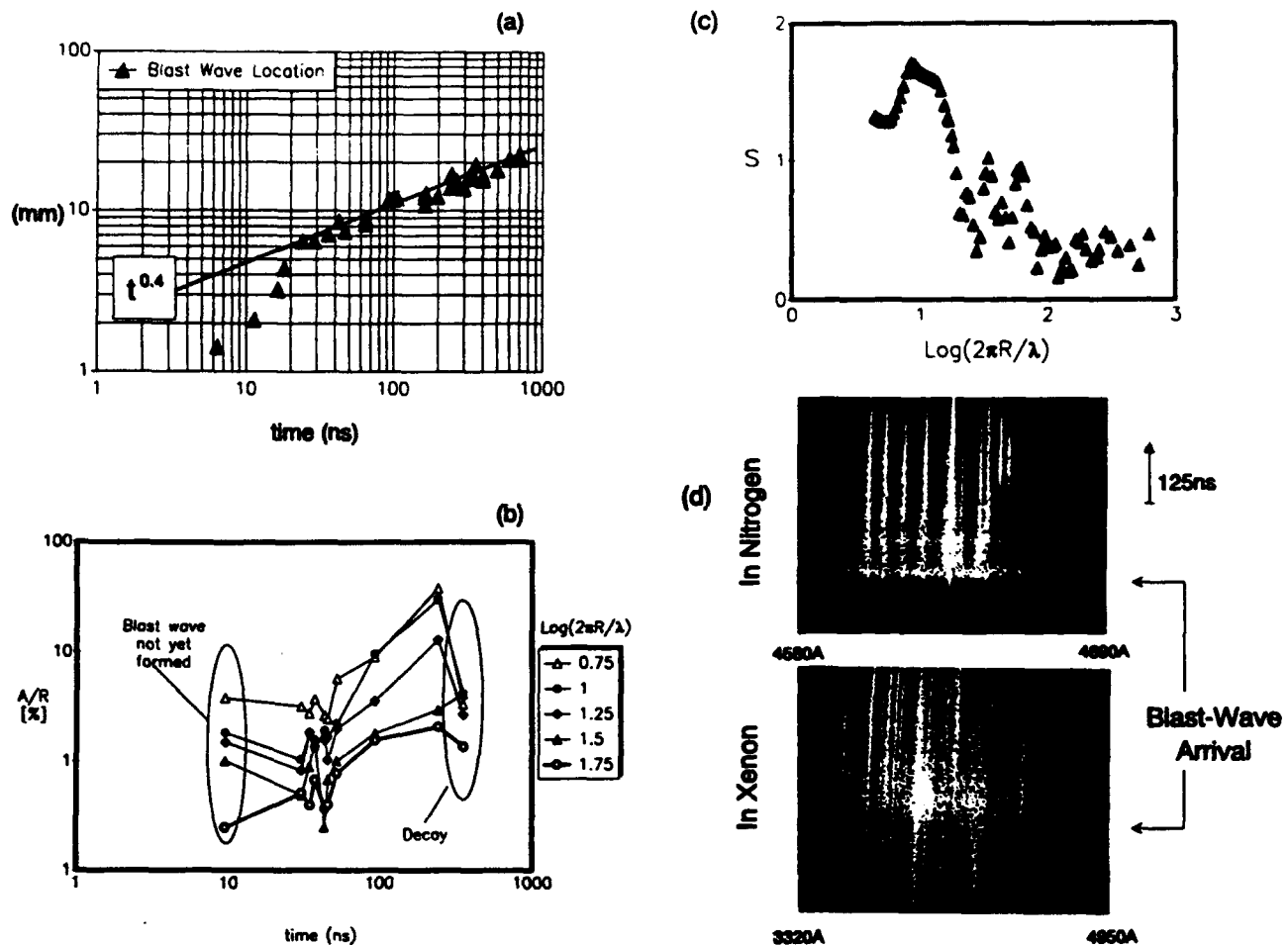


FIG. 3. Instability growth. (a) Blast-wave trajectory. (b) Amplitude growth as a function of time for different values of $\ln(kR)$. The scatter of points between 30 and 45 ns at each value of $\ln(kR)$ indicates the shot-to-shot reproducibility in this experiment. (c) Growth exponent $S(kR)$. (d) Emission spectra as a function of time in nitrogen and xenon gas from a spot which is 2 cm from the laser's focal point.

which reduces its effective γ below that of nitrogen.

Among the various theories,²⁻⁴ the one by Vishniac and Ryu⁴ predicts that Taylor-Sedov blast waves in a uniform gas with $\gamma < 1.2$ will become unstable. In spherical geometry, perturbations are predicted to grow as $Y_{lm}(\theta, \phi)t^{S(l)}$, where Y_{lm} are spherical harmonic modes. In planar geometry, perturbations grow as $e^{iky}t^{S(kx)}$, where x is the direction of blast propagation. For $\gamma = 1.1$, numerically calculated maximum growth occurs at $\ln(l) \approx 1.5$ with $\text{Re}[S(l)] \approx 0.5$, and $\ln(kx) \approx 1.2$ with $\text{Re}[S(kx)] \approx 0.3$, for the spherical and planar cases, respectively. For $\gamma = 1.06$, a less precise but analytic calculation¹¹ in spherical geometry gives maximum growth at $\ln(l) \approx 1.7$, with $\text{Re}[S(l)] \approx 0.7$. Theory does not treat the large-amplitude regime where saturation or stabilization may occur.

The basic predictions of this theory agree with our observations of r^S growth in a low- γ uniform gas, but there are differences in the details. For $\gamma = 1.06$ we measure

maximum growth at $\ln(kR) \approx 1$ with $S \approx 1.6$, whereas theory predicts maximum growth at higher $\ln(l)$ and lower S : Theory predicts virtually no growth ($S \approx 0.04$) at $\ln(l) = 1$. Possible stabilization is seen at 400 ns. We remind the reader, however, that the wave numbers in our experiment were obtained from the projection onto a plane of the edge of an unstable sphere. Thus, kR is not identical to either l or kx . Also, there are a few alternative explanations for the observed apparent stabilization. One may argue, for example, that the stabilization is a real nonlinear phenomenon; or that γ is large at some point far from the focal spot and the blast wave stabilized because it moved into that region; or that the instability is still growing but the density gradients in the spikes are too gentle to measure at late times. These issues will be addressed in future work.

We point out that the phenomenon described here is not the Rayleigh-Taylor instability commonly associated with decelerating systems. That instability is caused by

opposing density and pressure gradients and exhibits exponential growth. This instability is associated with the sloshing of material within the blast-wave shell and exhibits power-law growth. Our instability mechanism may be briefly explained as follows:⁴ The thermal pressure which drives the blast wave is perpendicular to the local blast shell surface, while the external ram pressure (ambient density times square of blast speed) is antiparallel to the direction of propagation. In a uniform blast wave the front and the direction of propagation are orthogonal so that the thermal and ram pressures are both perpendicular to the shell surface. But in a rippled blast wave the thermal pressure is no longer parallel to the propagation direction while the ram-pressure orientation does not change. Therefore, there appears a net pressure along the blast front surface that accelerates mass into the lagging trough parts of the ripple. The now heavier trough has more momentum, slows less, and consequently moves ahead. Then the process reverses and an oscillation ensues. This oscillation is damped out at wavelengths comparable to the blast shell radius and wavelengths much larger than the shell thickness. Otherwise, it grows. Since shell thickness is related to γ , so is the growth exponent of the instability.

In conclusion, we have shown experimentally, for the first time, that Taylor-Sedov blast waves in a uniform gas are unstable when the adiabatic index γ is sufficiently low, in our case 1.06. Perturbed amplitudes grow as a power of time. Our results confirm the basic predictions of Vishniac and Ryu.

We are grateful to Levi Daniels, Jim Ford, and Nicholas Nocerino for their expert and dedicated technical assistance. We acknowledge electronic-mail exchanges with Dr. Ethan Vishniac on the utilization of the analytic theory in Ref. 4. The authors also thank Dr. Jim Barthel and Dr. David Book for reviewing early versions of this manuscript. This work is supported by the Office of Naval Research and the Defense Nuclear Agency.

^(a)Present address: Laser-Plasma Branch, Plasma Physics Division, Washington, DC 20375-5000.

^(b)Present address: Science Applications International, McLean, VA 22101.

^(c)Present address: Physical Sciences, Inc., Alexandria, VA 23701.

^(d)Present address: Physics Department, SW Texas State University, San Marcos, TX 78666.

¹Sample works: R. A. Chevalier, *Astrophys. J.* **207**, 872 (1976); H. Gerola and P. E. Seiden, *Astrophys. J.* **223**, 129 (1978); J. P. Ostriker and L. L. Cowie, *Astrophys. J. Lett.* **243**, L127 (1981); V. Trimble, *Rev. Mod. Phys.* **60**, 859 (1988).

²P. A. Isenberg, *Astrophys. J.* **217**, 597 (1977); A. Cheng, *Astrophys. J.* **227**, 955 (1979); I. B. Bernstein and D. L. Book, *Astrophys. J.* **240**, 223 (1980); B. Gaffet, *Astrophys. J.* **279**, 419 (1984); B. Gaffet, *Astron. Astrophys.* **135**, 94 (1984); I. Kohlberg, Kohlberg Associates Report No. KAINRL02-89, 1989 (unpublished).

³W. I. Newman, *Astrophys. J.* **236**, 880 (1980).

⁴E. T. Vishniac, *Astrophys. J.* **274**, 152 (1983); D. Ryu and E. T. Vishniac, *Astrophys. J.* **313**, 820 (1987); E. T. Vishniac and D. Ryu, *Astrophys. J.* **337**, 917 (1989).

⁵L. I. Sedov, *Similarity and Dimensional Methods in Mechanics* (Academic, New York, 1959).

⁶P. G. Burkhalter *et al.*, *Phys. Fluids* **26**, 3650 (1983).

⁷J. Grun *et al.*, *Appl. Phys. Lett.* **39**, 545 (1981); *Phys. Fluids* **26**, 588 (1983); **29**, 3390 (1986).

⁸B. H. Ripin *et al.*, in *Laser Interactions and Related Plasma Phenomena*, edited by H. Hora and G. H. Miley (Plenum, New York, 1986), Vol. 7, pp. 857-877; J. Grun *et al.*, *ibid.* (to be published), Vol. 9; and (to be published).

⁹An 80% cosine taper (Tukey) window is used to eliminate mismatches at the ends of the region to be transformed.

¹⁰Ya. B. Zel'dovich and Yu. P. Raizer, *Physics of Shock Waves and High-Temperature Hydrodynamic Phenomena* (Academic, New York, 1966); the claim that $\gamma_{xc} < 1.13$ for any reasonable value of γ_N relies primarily on the accuracy of the Chernyi blast-wave solution on page 99. Error bars in γ_{xc} result from the error bars in γ_N .

¹¹Calculated using equation 19 in the 1989 paper of Ref. 4. In that paper we used $D = (\gamma - 1)/3(\gamma + 1)(1 - \beta)$.

**OBSERVATION OF HIGH-PRESSURE
BLAST-WAVE DECURSOR**

Observation of high-pressure blast-wave decursors

J. Grun, J. Stamper,^{a)} C. Manka, J. Resnick,^{b)} R. Burris,^{b)} and B. H. Ripin
Space Plasma Branch, Plasma Physics Division, Naval Research Laboratory, Washington, DC 20375-5000

(Received 17 December 1990; accepted for publication 29 April 1991)

We observe, for the first time in a laboratory, the formation of decursors at intersections of planar surfaces with powerful blast waves. The blast waves, which have hundreds-kilobar overpressures, are created by rapid ablation of material heated with an intense laser beam.

It is well known that a blast wave colliding with a planar surface sets up a reflection that propagates back into the ambient gas heated by the passage of the incident front. The interacting incident and reflected blast fronts can form structures known as Mach stems and triple points.¹ Even more complex structuring can occur if the reflecting surface is shaped, or if the sound speed near the surface varies. For example, if the sound speed near the reflecting surface is higher than in the rest of the ambient gas, part of the blast front moves faster and outruns the bulk of the blast wave. This, in turn, forms additional shocks and complicated vortical flow patterns. The structure which outruns the blast wave, called a precursor, has been studied at length both theoretically and experimentally.^{2,3} It is also possible to envision situations in which the sound speed near the reflecting surface is slower than in the rest of the ambient gas. Under such circumstances, one expects that one part of the blast wave will lag behind the rest. The existence of such structure, called a decursor, has been considered theoretically but it has never been seen in an experiment.

We report the first observation of blast-wave decursors. In our experiment blast waves are created by rapid ablation of material heated with an intense laser beam. We will show that such laser-induced blast waves follow Taylor-von Neumann-Sedov scaling^{4,5} and that their overpressures are much higher than overpressures achievable with chemical explosives.

Figure 1 shows how a laser is used to create blast waves. A small, millimeter-diameter, foil or sphere target is placed in an evacuated chamber, which is then backfilled with gas. The target surface is irradiated at high intensity by a focused pulse from the PHAROS III Nd glass laser (which has three beams and can produce up to 1500 J per pulse). Material ablating from the target surface expands rapidly into the background gas—much like the products of a chemical explosion—and forms a blast wave.^{4,5} In the experiments described here, the targets are 9- μm -thick polystyrene foils and 1/16 in. diam aluminum rods, the atmosphere is 5 Torr of nitrogen gas, and the laser pulse is a 100–200 J, 1.054 μm , 5 ns, pulse focused to a 880- μm -diam spot. This produces an irradiance of 3 TW/cm². With these parameters the foil surface heats to about 800 eV,⁶ and ablates (or explodes) away at about 700 km/s.^{7–9} A

classic blast wave forms within about 10 ns.

The blast front structure is photographed using the dark-field imaging method, which is sensitive to density gradient fluctuations.¹⁰ In our implementation, a 0.53 μm , < 1 ns duration, 2-in.-diam, few-millijoule laser probe illuminates the blast-wave side-on. Density gradients within the blast wave deflect part of the probe while the remainder passes through undisturbed. The emerging probe beam is then relayed onto a film surface with a telescope. A stop placed at a focal point inside the telescope blocks the undisturbed component of the probe light but passes the deflected part, thereby forming an image in which blast-front gradients appear as bright features on a dark background.

In addition, the visible emission from the blast front is photographed with a very fast (100 ps shutter), four-frame, microchannel-plate intensifier camera. Thus, together with the dark-field image, we get five photographs of the blast wave at different times in its evolution. This minimizes shot-to-shot variations and gives an accurate measure of the blast-wave region history.

Different blast-wave-surface configurations are shown in Fig. 2. Figure 2(a) shows a blast wave soon (185 ns) after it hit an aluminum plane placed 6 mm below the laser's point-of-focus. The blast wave shows up as a bright circle surrounding the focus. Above the aluminum plane are seen diffuse, bright features that rise to the point-of-focus immediately below the explosion, but stay closer to the plane as the lateral distance from the explosion in-

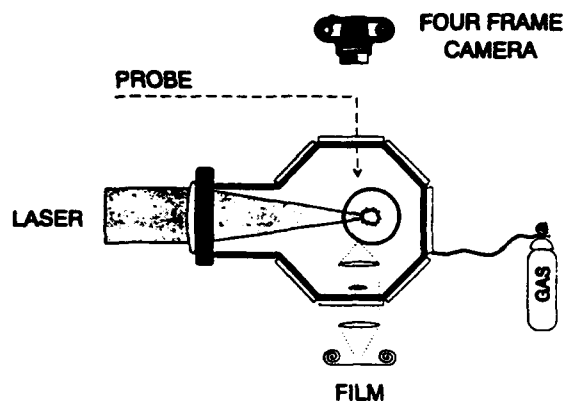


FIG. 1. Experimental setup. A blast front is launched by an energetic, laser-produced plasma expanding into a low-pressure ambient gas. Emission from the blast front is imaged with a four-frame, fast-gated intensifier, optical imager (GOI). Density gradients are recorded with a dark-field shadowgraphy camera.

^{a)}Code 4730, Naval Research Laboratory, Washington, DC 20375.

^{b)}Physical Sciences Inc., 635 Slaters Lane, Alexandria, VA 22314.

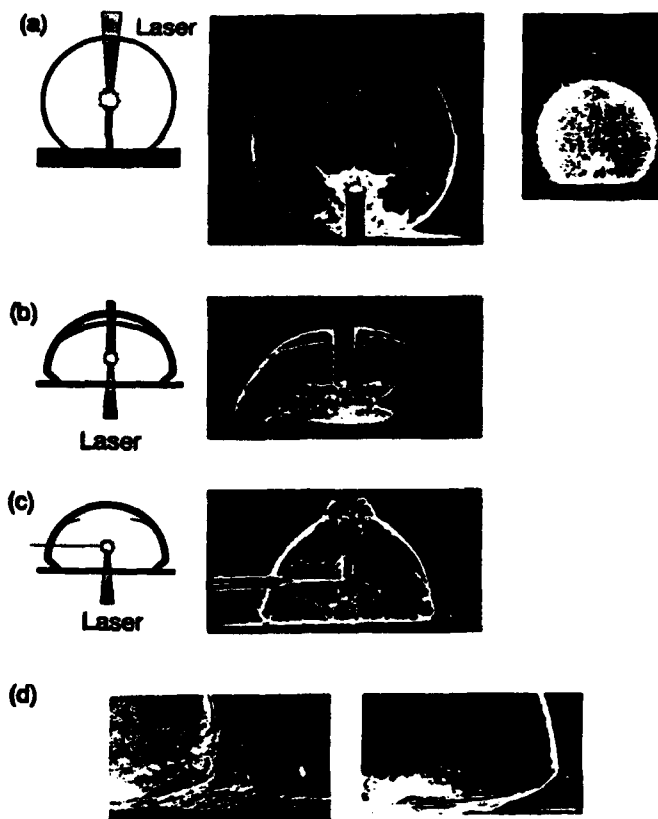


FIG. 2. Structuring of blast waves near reflecting, aluminum surfaces as seen with dark-field shadowgraphs and visible emission photographs. The blast waves originate about 6 mm above the surface and propagate in 5 Torr of nitrogen. (a) Spherical blast wave originating at the tip of an aluminum rod as observed 185 ns after explosion. The laser energy was 210 J. (b) Mach stem, triple point, and decursor formation in a blast wave originating at the tip of an aluminum rod. The laser energy was 100 J and the observation was at 302 ns. (c) A blast wave from a plastic target shows Mach stems, triple points, and strong decursor at 357 ns after explosion. Laser energy was 103 J. (d) Closeups of different decursor shapes observed in this experiment.

creases. Similar features, which surround the point-of-focus itself are seen in both the dark-field and emission photographs. These diffuse features, which do not exhibit any sharp characteristics associated with blast waves and shocks, are signatures of material ejected from the target and also of material ablated or vaporized from the surface of the reflecting plane by radiation from the focus region or the blast front. The electron density of the ionized material near the plane is comparable to the density of the 5 Torr background nitrogen gas—implying that the gas above the plane is mostly singly ionized. (Electron density was estimated by calculating the minimum probe deflection necessary to miss the stop inside the dark-field telescope.) The reflected part of the blast wave is buried within the features of the ionized gas and is, therefore, not clearly visible. A dark circle near the top of the photograph marks the passage of the laser beam.

Figure 2(b) taken later at 302 ns, shows well developed Mach stems and triple points. As in the previous picture, there is evidence of ionized material around the focal point and near the reflecting plane. Where the blast

wave meets the plane we see the rounded, tucked-back features of a decursor.

Much clearer and stronger decursors are seen in Fig. 2(c), observed at 357 ns after explosion. By this time the diffuse plasma features near the plane are no longer seen. The decursor is also straighter than the rounded decursor in the previous shot. The same photograph also shows Mach stems and triple points.

A likely explanation of why our experiment forms decursors is that the material ablated or vaporized from the reflecting plane forms a layer with increased density and/or effective mass, and a lower sound speed. The source of energy for this ablation is radiation from the laser-heated plasma and/or the blast wave. Radiant energy from plastic and aluminum targets which are heated to 800 eV constitute approximately 5% and 25% of the incident laser energy, respectively.¹¹ The ratio of blast-wave speed to decursor speed can be estimated by assuming that it is roughly the same as the ratio of their respective distances from the point of explosion. For the shots shown in Fig. 2 that ratio is 1.1.

The spatial and temporal scales of laser-induced blast waves are much shorter than the scales in traditional shock tube or explosively driven experiments. Typical laser-laboratory scales are centimeter and submicrosecond versus tens of centimeters and milliseconds in the more traditional methods. Also, our experiments were done at a fraction of atmospheric pressure. It is, therefore, legitimate to ask how laser driven shocks relate to those produced in more usual environments. We proceed to show that laser-produced blast waves follow the scaling laws of ideal blast waves. We will also show that laser-produced blast waves achieve overpressures unreachable by explosively driven methods.

Ideal blast waves propagate according to the Taylor-von Neumann-Sedov relation:¹²

$$R \approx \zeta (E/\rho_0)^{1/5} t^{2/5},$$

with

$$\zeta = \{ [75(\gamma - 1)(\gamma + 1)^2] / 16\pi(3\gamma - 1) \}^{1/5}, \quad (1)$$

where E is the explosion energy, ρ_0 is the ambient-gas density, t is the time of observation, and γ is the ratio of specific heats. These expressions were derived assuming spherical symmetry, energy and momentum conservation, and an instantaneous, massless, point explosion. We have performed detailed experiments to verify that laser-produced blast waves follow Eq. (1).⁴ Many parameters such as the laser energy, laser focal-spot size (and therefore the ablation velocity), pressure, and observation times were varied in these experiments. As long as the ambient pressure is high enough (> 0.5 Torr) to place the experiment in a collisional regime, laser-produced blast waves follow the Taylor-von Neumann-Sedov relation. From the data and Eq. (1) we determined that $\zeta = 1.0 \pm 0.1$ in a nitrogen ambient gas, which implies a γ of 1.4 ± 0.2 .

Blast-wave overpressure is determined from the dark-field photographic data using the following expressions:^{2,12}

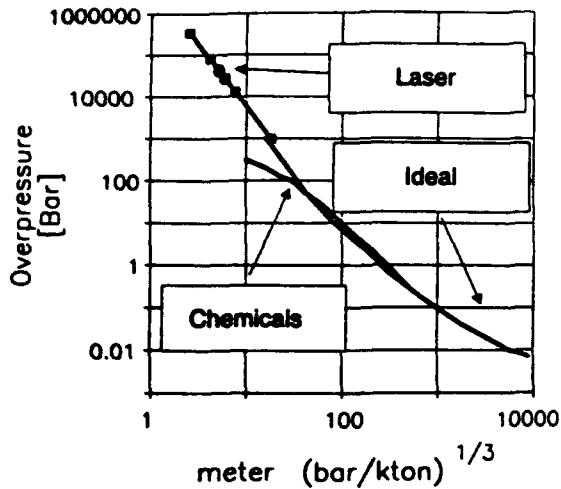


FIG. 3. Laser-created blast-wave overpressures compared to ideal overpressures and overpressures created by chemical explosives. Blast waves created by nuclear explosions follow the ideal curve. The horizontal axis is the distance from the explosion point scaled with (ambient pressure/explosion yield)^{1/3}.

$$\frac{P}{P_0} = \frac{2\gamma}{\gamma + 1} (M^2 - 1), \quad (2)$$

$$M = \frac{(dR/dt)}{C_0}, \quad (3)$$

$$\frac{dR}{dt} = [3(\gamma - 1)(\gamma + 1)^2/4\pi(3\gamma - 1)]^{1/2} \times [E/\rho_0]^{1/2} R^{-3/2}, \quad (4)$$

where P is the peak overpressure, P_0 is the ambient pressure, M is the blast-wave's Mach number, and C_0 is the sound speed in the ambient gas.

Figure 3 plots the overpressures inferred from Eqs. (2)–(4) as a function of distance from the explosion scaled using the Sachs scaling law.^{1,13} This law, which is based on geometrical similarity principles and conservation of momentum, is used to plot and compare experiments performed with different explosive yields and at different ambient pressures. Also plotted are curves expected of an ideal blast wave and a blast wave created with explosives.¹ This figure shows that laser-produced blast waves follow the ideal scaling law, as do nuclear blast waves² which occur at higher ambient pressures and have significantly larger spatial and temporal scales. They also continue to follow the ideal law at much higher pressures than blast waves produced with chemical explosives. Furthermore,

the laser experiment produces blast waves with overpressures greater than 100 kbar, which is more than 1000 times greater than the capability of conventional explosives.

In conclusion, we have shown that rapid ablation produced with focused laser beams can serve as a useful driver for the study of high-pressure blast waves. In particular, we demonstrated that such "explosions" produce Taylor-von Neumann–Sedov blast fronts in a pressure regime much higher than otherwise achievable in a laboratory. These laser-driven blast waves can be used to simulate and investigate many interesting and relevant blast front-surface interactions. We report, for the first time, observations of blast-wave decursor formation. In future experiments we will study the phenomena observed here more quantitatively and will extend our measurements to higher ambient pressures.

We are grateful to Mr. Levi Daniels, Mr. Jim Ford, and Mr. Nicholas Nocerino for their expert and dedicated technical assistance. This work is supported by the Defense Nuclear Agency.

- ¹G. F. Kinney and K. J. Graham, *Explosive Shocks in Air* (Springer, New York, 1985).
- ²S. Glasstone and P. J. Dolan, eds., *The Effects of Nuclear Weapons* (United States Department of Defense and the Energy Research and Development Administration, Washington, DC, 1977).
- ³W. J. Glowacki, A. L. Kuhl, H. M. Glaz, and R. E. Ferguson, in *Shock Waves and Shock Tubes*, edited by D. Bershader and R. Hanson (Stanford University, Stanford, CA, 1986), p. 187; D. Krauss-Varban, *ibid.*
- ⁴B. H. Ripin, A. W. Ali, H. Griem, J. Grun, S. Kacenjar, C. K. Manka, E. A. McLean, A. N. Mostovych, S. P. Obenschain, and J. A. Stamper, in *Laser Interaction and Related Plasma Phenomena*, edited by H. Hora and G. H. Miley (Plenum, New York, 1986), Vol. 7, p. 857.
- ⁵J. Grun, J. Stamper, J. Crawford, C. Manka, and B. H. Ripin, in *Laser Interactions and Related Plasma Phenomena*, edited by H. Hora and G. H. Miley (Plenum, New York, 1990, in press), Vol. 9.
- ⁶P. G. Burkhalter, M. J. Herbst, D. Duston, J. Gardner, M. Emery, R. R. Whitlock, J. Grun, J. P. Apruzese, and J. Davis, *Phys. Fluids* **26**, 3650 (1983).
- ⁷J. Grun, B. Stellingwerf, and B. H. Ripin, *Phys. Fluids* **29**, 3390 (1986).
- ⁸J. Grun, R. Decoste, B. H. Ripin, and J. Gardner, *Appl. Phys. Lett.* **39**, 545 (1981).
- ⁹J. Grun, S. P. Obenschain, B. H. Ripin, R. R. Whitlock, E. A. McLean, J. Gardner, M. J. Herbst, and J. A. Stamper, *Phys. Fluids* **26**, 588 (1983).
- ¹⁰Technically, the image intensity variations are proportional to fluctuations in the square of the index of refraction.
- ¹¹A few representative references: M. Galanti and N. J. Peacock, *J. Phys.* **B 8**, 2427 (1975); D. Duston and J. Davis, *Phys. Rev. A* **23**, 2602 (1981); B. K. Sinha, *J. Appl. Phys.* **52**, 3010 (1981); U. Feldman *et al.*, *Astrophys. J.* **192**, 213 (1974); P. G. Burkhalter *et al.*, *Phys. Fluids* **26**, 3650 (1983).
- ¹²Ya. B. Zel'dovich and Yu. P. Raizer, *Physics of Shock Waves and High-Temperature Hydrodynamic Phenomena* (Academic, New York, 1966).
- ¹³P. G. Sachs, "The Dependence of Blast on Ambient Pressure and Temperature," Aberdeen Proving Ground, Maryland, BRL Report No. 466 (1944).

**TURBULENCE IN VERY-HIGH MACH NUMBER,
LASER-ACCELERATED MATERIAL**

TURBULENCE IN VERY-HIGH MACH NUMBER, LASER-ACCELERATED MATERIAL

J. Grun, J. Stamper, J. Crawford*, C. Manka, and B.H. Ripin

Space Plasma Branch

Plasma Physics Division

Naval Research Laboratory

Washington DC 20375

* Physics Department

SW Texas State University

San Marcos, Texas 78666

INTRODUCTION

Most flows in nature are turbulent. Often, turbulence critically influences the nature of an important event. For example, satellite communications can be interfered with by natural or man-made turbulence in the earth's atmosphere¹; x and gamma rays in the 1987A supernova appeared prematurely because of turbulence²; the rate of star formation depends on the nature of interstellar turbulence³; turbulent mixing influences the efficiency of inertial-confinement-fusion pellets⁴. There are many other examples in aeronautics, chemistry, and combustion.

Turbulence has been studied for more than a century but it is still incompletely understood⁵. This is not surprising: Turbulence is by definition highly nonlinear, experiments are difficult to interpret quantitatively, and it is hard to relate experimental observations to theoretical predictions. Many experiments, such as those in shock tubes, suffer from extraneous effects caused by walls and membranes. However, with rapid advances in computer architecture, advances in computer aided visualization and analysis, and advances in experimental methods, rapid progress in understanding turbulence is now possible.

High-power lasers, such as those used for inertial-confinement-fusion research, are a new and very good tool for studying turbulence and other hydrodynamic phenomena^{6,7,8}. Laser hydrodynamics experiments are not hampered by walls and membranes that make clean shock tube experiments difficult. Areas of parameter space not accessible by conventional methods can be reached easily with high-power lasers. For example, multi-megabar pressures, Mach numbers of a few hundred, temperatures of many electron volts can be achieved. Intense x-ray radiation can be turned on when needed. Also, it is relatively easy to vary parameters, such as pressure, flow speed, Mach number, temperature, fluid composition, etc., over a broad range. Laser experiments can duplicate many astrophysical parameters⁹. Also, many of the sophisticated diagnostics which have been developed over the past twenty five years for fusion research can be utilized in hydrodynamics experiments.

We use the N.R.L. Pharos III laser and target facility to study linear and nonlinear hydrodynamic flows. This paper describes our experimental work in very high Mach number turbulence.

DESCRIPTION OF EXPERIMENT

The Pharos III laser facility 10 has a three-beam glass laser with an output of 500 joules per beam at a wavelength of $1.054\mu\text{m}$ in a 2-6ns pulse. The laser wavelength can also be halved. Irradiances of 300 terawatts per square centimeter can be produced by focusing the laser a few hundred micron diameter spot. The spatial irradiance profile can be shaped and smoothed to a few percent level with the induced-spatial-incoherence (ISI) method¹¹. Experiments are performed in a large, 80 cm radius chamber which can be evacuated or filled with gas. A magnetic field of up to 10 kgauss over more than 100 cm^3 surrounding the point of laser focus can be turned on. Figure 1 shows a photograph of the area around the Pharos III target chamber.

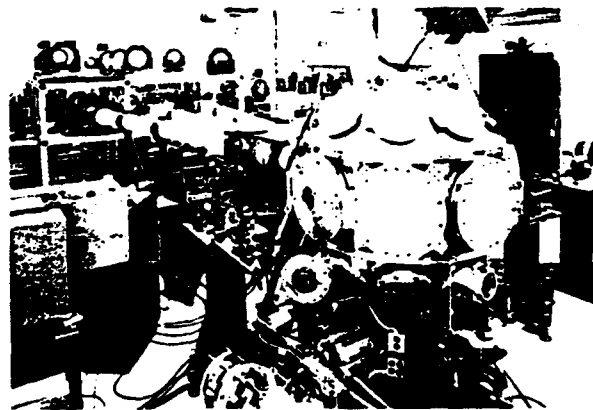


FIGURE 1. Photograph of the area around the Pharos III target chamber. Laser focusing optics and parts of laser beam diagnostics are seen in the background.

In this work one beam of the laser is focused onto the surface of thin, 5-20 μm , polystyrene (CH) or aluminium foils to produce an irradiance of 1-300 terawatts/cm² in a 100-1000 μm diameter spot. The chamber is filled with gas but an external magnetic field is not used. This is what happens when the laser irradiates the foil:¹² The irradiated part of the foil (target) is heated on its surface to a temperature of about 800 eV¹³, causing the surface to ablate. The ablated material expands toward the laser at about 700 kilometers per second in a narrow shell¹⁴. Half of the ablation mass is contained within a 40 degree half-cone angle^{15,16}. Meanwhile, the background gas is photoionized by radiation from the target or by impact with ablation material. A Taylor-Sedov blastwave forms in front of the target when the ablated material sweeps up a gas mass equal to a few times its own¹⁷. The non-ablated part of the target is accelerated away from the laser by the rocket-like effect of the ablation material to speeds of 10-100 km/sec. During acceleration the target heats to 1-2 eV and becomes Rayleigh-Taylor unstable^{6,7,8}. Later, the unstable target becomes turbulent and entrains background gas so that it too becomes turbulent. When the acceleration ceases the target decompresses thermally. An example of a target irradiated in a background gas, showing both the blast wave and the turbulence, is shown in Fig.2.

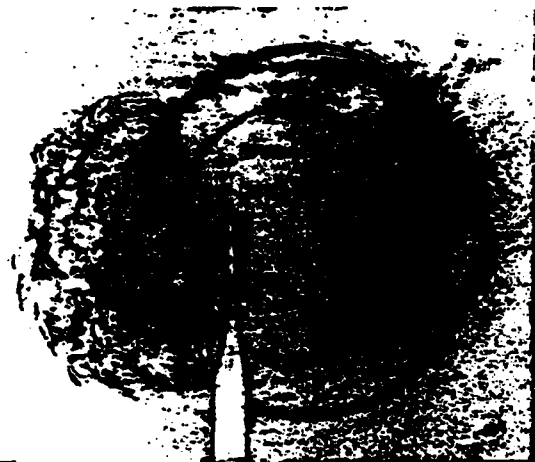


FIGURE 2. A dual-time Schlieren shadowgraph of an aluminium foil irradiated with 36 joules in 5 torr of nitrogen. The two exposures were at 55ns and 160ns. Note the blastwave on the laser side of the foil and the turbulent region behind the target.

Our most important diagnostic tool is a laser probe (0.53 μm , 350psec FWHM) which is transmitted through the turbulent region as shown in figure 3. The phase and amplitude of the probe may both, in theory, be affected by the turbulence. The disturbed probe light is recorded using various shadowgraphy methods, such as bright-field, Schlieren, or phase-contrast photography, and with holographic interferometry. In addition, visible light emission from the turbulent region is photographed with a gated optical imager (shuttered at 600psec) which is filtered so that it images emission from only the target material, only the background gas, or both. Emission spectra measured with a temporally and spatially resolved optical multichannel analyzer identify ionic species and help us estimate temperature.

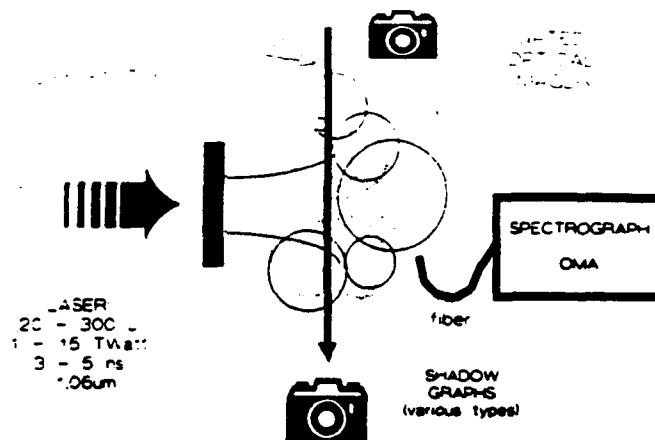


FIGURE 3. Schematic of experiment and main diagnostics.

CHARACTERISTICS OF THE TURBULENT REGION

In this section we address the following questions about the turbulent region: How does it move?; What is turbulent, the target, the background gas or both?; What is its spatial wavelength spectrum?; and, Can the spectrum be manipulated?

How does it move? Figure 4 shows a time sequence of phase-contrast photographs of the turbulent region. The speed of the turbulent front is determined from plots of the distance between the original foil position and the tip of the turbulent front versus the time of the observation (Fig. 5). From such time sequences we see that the front moves at a speed which is somewhat larger (< 20%) than the speed we calculate for the target material itself. Furthermore, the front is not slowed down by collisional interaction with the background gas. The front speed in figure 5 is moving at about Mach 70 with respect to the unheated background gas. Mach numbers of up to 200 were observed in other cases. The speed of the turbulent region does not depend strongly on the background gas pressure.

What is turbulent? The fact that turbulence exists - and yet its motion is not perceptively slowed down by the background gas - may indicate that a gas-target interchange instability is not a dominant factor in its development. Rather, the target itself, which we know to be linearly unstable^{6,7,8}, may be the primary cause of the turbulence. This would explain why the turbulent front speed is somewhat higher than the target speed and why it does not depend significantly on the background gas pressure. The front is probably a shock driven slightly ahead of the target material - much like a shock moving ahead of a supersonic piston. An alternative picture, that a target-gas interchange instability causes the turbulence, is less likely. If this was the case, we would intuitively expect the background gas to slow the target. Since this does not happen we believe the first picture above to be more probable: But a definitive answer awaits more experiments and calculation.

SHOT 88-546

SHOT 88-559

SHOT 88-554

SHOT 88-638

SHOT 88-639

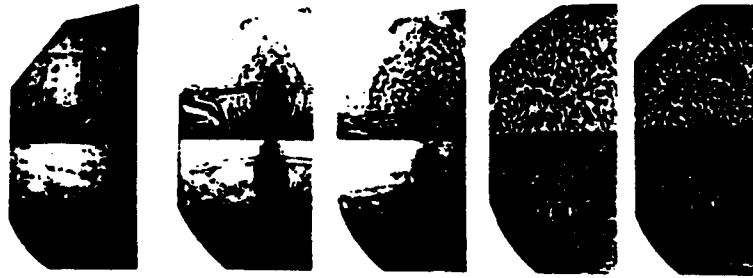
 $t = 50\text{ns}$ $t = 130\text{ns}$ $t = 219\text{ns}$ $t = 500\text{ns}$ $t = 750\text{ns}$

FIGURE 4. Sample bright-field and phase-contrast time sequence of the turbulent region. The target is $20\mu\text{m}$ CH and the background gas is 5 torr of nitrogen. Laser is incident from the bottom.

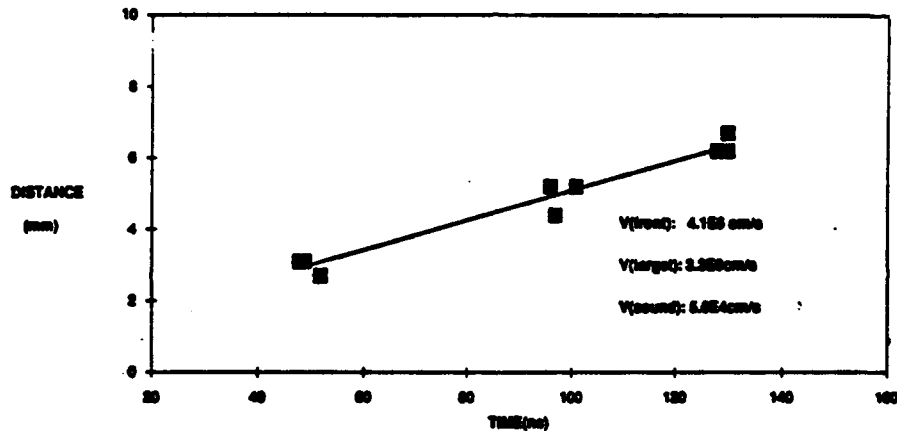


FIGURE 5. Trajectory of turbulent region for the case of a $9\mu\text{m}$ thick CH target irradiated with 5 terawatts/cm² in 5 torr of nitrogen. The turbulent region moves at Mach 70.

Nevertheless, the background gas does mix with the target "piston", and is, therefore, also turbulent. This can be seen by examining photographs of visible light emission from the turbulent region and comparing them to shadowgraphy pictures taken at the same time on the same shot. In front of the camera is a narrow band-pass (50Å FWHM) interference filter which passes the 5001Å N^{++} line from the background nitrogen gas. In general, the overall shape of the emission region matches closely with the turbulent region seen by shadowgraphy. But, small scale $10\text{-}100\mu\text{m}$ structures seen in the shadowgraphs are washed out in the emission pictures, probably by integration of the emission along the line-of-sight through the turbulent volume: The smallest emission structures have a size of about $200\mu\text{m}$. (Camera resolution is $50\mu\text{m}$ in the target plane.) Limb brightening causes the outer edges of the emitting region to be brighter than the inner regions. Figure 6a shows a sample emission picture and figure 6b a time integrated

spectrum from the turbulent region. No spectral lines from highly ionized states of are observed. From this we estimate that the temperature in the turbulent region is about 10 eV or less.

To further test the relationship between turbulence and background gas we varied the gas pressure (0.05 to 10,000 mTorr) and the gas species (He, N, Xe). Interestingly, below 200 mTorr of nitrogen the turbulence could not be seen in our emission and shadowgraph diagnostics. Turbulence was never observed in high vacuum. This may mean that the shadowgraphy diagnostics are sensitive to features of the background gas - perhaps density gradients in the swept up gas - and that collision with the background gas raises the temperature so that the region emits enough to be seen. This would have to be the case if the hypothesis that the target is turbulent without the presence of gas is correct. When the turbulence is seen it does not seem to be affected by the type or the pressure of gas. However, detailed spectral information has not yet been quantified.

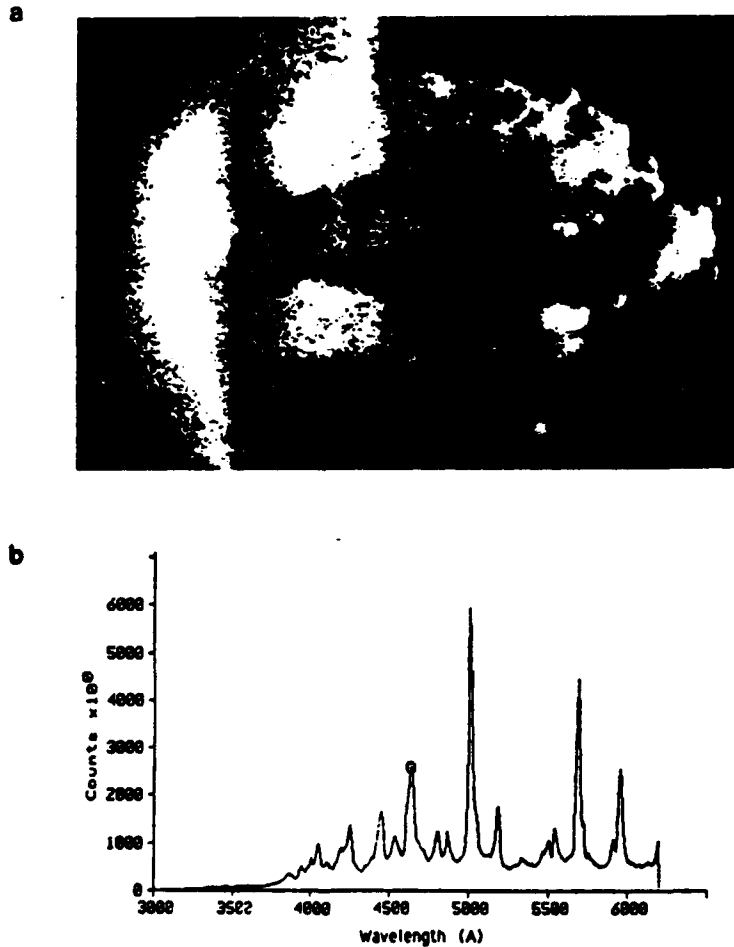


FIGURE 6. (a) Sample emission photograph and (b) sample emission spectrum of the turbulent region.

Power Spectral Characteristics

Nonuniformities in the turbulent region can be quantified by measuring their spatial frequency spectrum. Although such a spectrum cannot uniquely identify a turbulence mechanism, any theory that does not reproduce the spectrum can be eliminated. In addition, such spectra are used by designers of systems that must operate in turbulent surroundings. The challenge for experiments is to relate the observed structures to some underlying physical quantity such as density, energy, index of refraction, etc. In our work this is being done using phase-contrast shadowgraphy and holographic interferometry¹⁸.

Phase-contrast shadowgraphy is an application of the Zernike phase-contrast microscope¹⁹ to plasma research. The method is described with modern Fourier-transform mathematics by Cutrona et al.²⁰ Presby and Finkelstein²¹, we recently discovered, were the first to use it in plasma research. The essential aspects of the method may be easily understood by considering the following simplified argument: Imagine the laser probe (Fig. 3) to be a planar electric wave of amplitude E . Assume that turbulence alters the phase, but not the amplitude, of the probe so that after the probe traverses the turbulence its electric field is given by

$$(1) \quad E = E_0 \exp \{ i(\varphi + \theta(x,y)) \} \\ = E_0 \exp(i\varphi) \{ 1 + \sum (i\theta)^n/n! \}.$$

Here φ is an averaged spatially independent part of the phase shift and $\theta(x,y)$ is a spatially varying part (which need not be less than 1). The probe is imaged onto a camera with dual-lens astronomical telescope as shown in Fig 7a. The first lens of this telescope Fourier transforms the probe's electric field at its focal point. The second lens picks up the Fourier transformed electric field and Fourier transforms it again at the location of the camera. The camera photographs the square of the twice Fourier transformed electric field. Mathematically, the first Fourier transform is given by

$$(2) \quad F[E] = E_0 \exp(i\varphi) \{ F[1] + F[\sum (i\theta)^n/n!] \};$$

and the second Fourier transform by

$$(3) \quad F[F[E]] = E_0 \exp(i\varphi) \{ F[F[1]] + F[F[\sum (i\theta)^n/n!]] \};$$

and the image on the film by

$$(4) \quad \text{Image}(x,y) = \{ F[F[E]] \}^2$$

(Magnification, time, and axial direction in the phase terms are, for simplicity, not included here.)

Now, the $F[1]$ term in equation 2 is the transform of the undisturbed part of the probe. Physically, it is a spot of light on the lens axis. This spot can be manipulated, thereby modifying the photograph given by equation 4.

For example, without any manipulation the photograph is given by

$$(5) \quad \text{Image}(x,y) = E_0 E_0^*.$$

This is the so called bright-field shadowgraph. In the absence of absorption it is simply the image of the original probe. With absorption, it forms the shadow of the absorbing region.

If the central spot is eliminated the photograph is given by

$$(6) \quad \text{Image}(x,y) = E_0 E_0^* \{ \theta^2(-x,-y) + \dots \},$$

which is a Schlieren shadowgraph sensitive to the square of phase fluctuations.

If the central spot is shifted by a quarter wavelength the photograph is given by

$$(7) \quad \text{Image}(x,y) = E_0 E_0^* \{ 1 + 2\theta(-x,-y) + \dots \},$$

which is a phase-contrast shadowgraph sensitive to the first power of phase fluctuations.

From phase fluctuations we determine fluctuations in the index of refraction $N(x,y,z)$ integrated along the axial direction using

$$(8) \quad \int N(x,y,z) dz = \lambda_{\text{probe}} \theta(x,y) / 2\pi$$

where λ_{probe} is the probe wavelength. Assuming free electrons of density $n_e(x,y,z)$ dominate the index of refraction we get

$$(9) \quad \int n_e(x,y,z) dz = -\theta(x,y) (\lambda_{\text{probe}}^2 e^2 / m_e c^2)$$

The phase-contrast method is subject to the following caveats:

- Significant absorption or probe nonuniformity will invalidate the commutation in equation 2.
- As a practical matter, one cannot eliminate $F[1]$ by itself. One also eliminates the DC and low frequency components in the terms containing θ . Therefore, measurements of low frequency fluctuations are not accurate²².
- If phase fluctuations larger than π occur then equation 7 cannot be uniquely inverted. This causes aliasing and spectrum distortions. Therefore, any phase excursion greater than π should not occur often and/or be at wavelengths not of interest to the analysis.
- Optical distortions are neglected.

One nice feature of the method is that the probe is imaged right after leaving the turbulent region. Consequently, Fresnel diffraction effects, which would occur if the probe were to propagate a long distance, do not trouble us here. Fresnel oscillations, which distort phase measurements in atmospheric experiments²³ are not a problem.

Fig. 7b shows how the method is implemented in practice. The probe beam is split into two parts by a Wollaston prism after leaving the turbulent region. One part is imaged as a bright-field shadowgraph, while the other part is passed through a phase filter producing the phase-contrast shadowgraph of equation 7. The phase contrast filter is a flat ($\lambda/10$) fused silica window with a 1mm diameter by 2859 angstrom thick ($1/4 \lambda$) mesa on its surface. The film is calibrated by pre-exposing a part of it to the probe light through a Kodak step wedge.

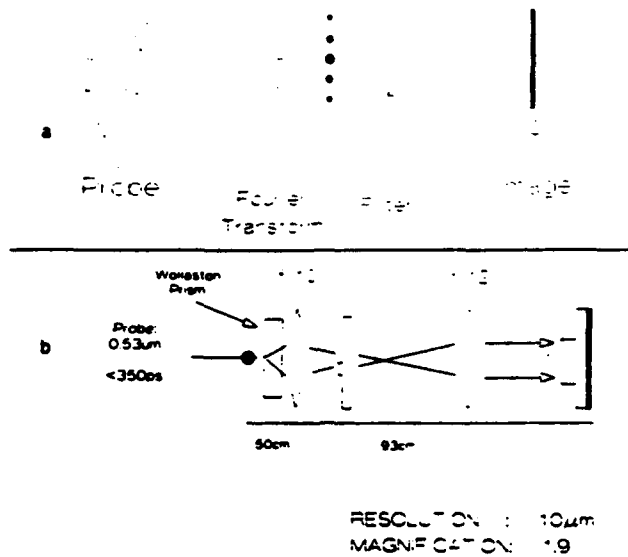


FIGURE 7. (a) Schematic of the phase-contrast concept. (b) Implementation of the phase-contrast method.

Simultaneous bright-field and phase-contrast shadowgraphs verify that absorption or probe nonuniformity effects are not important in the region of interest. Also, photographs taken without turbulence or plasma being present let us balance the two split beams of the probe, and verify that extraneous effects from the mask or the optics are minimal. The diameter of the mesa implies that spatial wavelengths longer than $500\mu\text{m}$ (ie. $\lambda_{\text{probe}} f_{\text{mask}} / r_{\text{mesa}}$) are not measured accurately.

Figure 8 shows typical bright-field and phase-contrast shadowgraphs. The bright-field image shows a shadow of the unirradiated part of the foil, and a shadow of slow material ejected by shocks and heat leakage from the laser spot. Such slow material plays no role in turbulence formation. Also visible is a segment of the ablation-side blast wave which wrapped itself around the rear of the foil. This blastwave scatters light out of the optical path so that, for practical purposes, it behaves as an absorbing object. The turbulent region is barely visible in a few tiny spots in the bright-field image but is very visible in the phase-contrast shadow, proving that the turbulence is primarily a phase object. The phase-contrast shadow is also rich in other phase disturbing features such as a weak shock reflected from the foil holder, and sound waves outside the boundaries of the turbulence.

The phase-contrast photographs are digitized and transformed into equivalent phase images on a computer using the mathematics outlined above. Then the spatial power spectral density is determined from the expression

$$(10) \quad \text{Power}(k_x) = \sum_x [\text{Abs} \int T(x) \theta(x,y) \exp(-ik_x x) dx]^2,$$

where $T(x)$ is an 80% Tukey window²⁴.

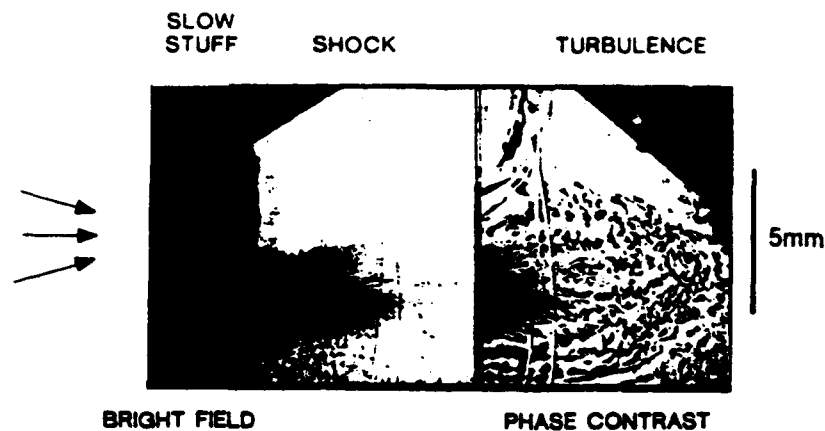


FIGURE 8. A bright-field and a phase-contrast shadowgraph of a $10\mu\text{m}$ Al foil irradiated with 4.5 twatts/cm^2 in 5 torr of nitrogen. The pictures were taken 219ns after the peak of the laser pulse. Laser is incident from the left.

A typical one-dimensional, spatial power spectrum is shown in Fig. 9. Most turbulent power spectra can be characterized by three quantities: an 'outer scalelength' at which energy is pumped into the system, the 'inertial range' of wavelengths at which energy cascades from larger to smaller scales, and an 'inner scalelength' at which energy dissipates out of the system. In our case the outer scalelength is about 1mm which is similar to the diameter of the focal spot. (However, this number is not very reliable as explained above.) The inertial range has a $k_x^{-2.1}$ scaling. An inner scalelength is not observed at $20\mu\text{m}$ or larger wavelengths. Inner scalelengths smaller than $20\mu\text{m}$ are not unreasonable for the estimated Reynold's number in this flow. The scaling of the inertial range is independent of scan direction, reflecting symmetry in the fine turbulent structure.

A two-dimensional, k-space power spectrum, $P(k_x, k_y)$, can also be calculated. We find that $P(k_x, k_y=0) = k_x^{-3.2}$ and $P(k_x=0, k_y) = k_y^{-3.2}$. $P(k) = \int (P(k_x, k_y)) k d\phi$, where ϕ is the azimuthal angle in k_x, k_y space, varies as $k^{-2.1}$. The various scalings are all consistent for spatially symmetric turbulence.

We have yet to show that unacceptable aliasing is not a problem with the phase-contrast measurements. This can be tested with holographic interferometry which measures absolute phase disturbances caused by phase objects, and can also provide an independent determination of the power spectrum. Such interferograms have been taken with a variety of background fringe spacings. Interferograms with fringe spacings of 1mm and $360\mu\text{m}$ show the outlines of the turbulent region clearly. However, the fringes cannot be followed into the turbulent region itself since they have a coarser scale than the turbulence fluctuations. But fringes in interferograms with $70\mu\text{m}$ spacing (Fig.10) can be followed through most of the turbulence. A visual analysis shows that aliasing is probably not significant, but a quantitative estimate has yet to be made. The mathematics for extracting two-dimensional phase information from holographic interferograms of laminar

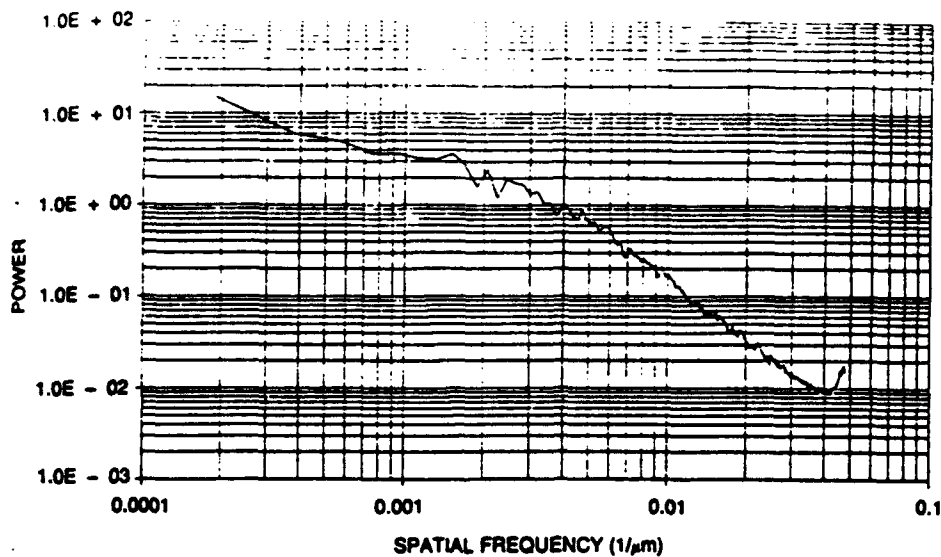


FIGURE 9. One dimensional power spectrum of the turbulent region in a typical shot.

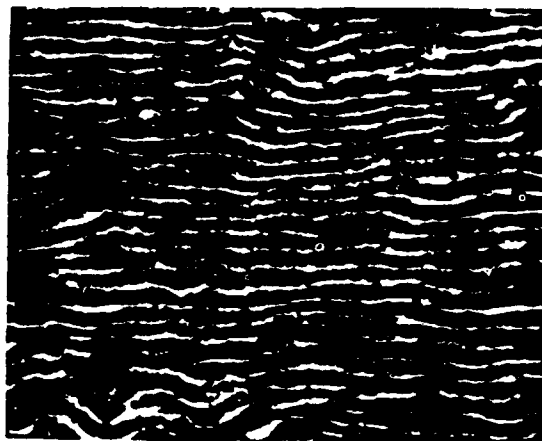


FIGURE 10. Enlarged section of a holographic interferogram of the turbulent region. Reference fringes are spaced $70\mu\text{m}$ apart.

phase objects have been discussed by Takeda²⁵ and Nugent²⁶. We are currently evaluating such methods for accuracy in a turbulent case.

Turbulence control Power spectra alone are insufficient to unambiguously identify the responsible turbulence mechanism. Indeed, we have not proven that the nonuniformities are turbulent in the sense that energy is cascading from larger to smaller scales, or whether they are a frozen eddy structure with a spectrum determined by a linear instability. By manipulating the turbulence we may get further clues into its nature. For example, we can try to turn the turbulence on and off, or to control its power spectrum. If the Rayleigh-Taylor instability in the target is responsible for the turbulence, perhaps we can accelerate a stable target and see if the turbulence disappears. We have accomplished some of these goals in a few different ways. For example:

Burn Through: By focusing the laser beam to a tight spot we can raise its irradiance so that the entire target is heated by x rays, fast electrons and explodes. There is no ablative acceleration and the Rayleigh-Taylor instability is stabilized. When we irradiated a target under such conditions turbulence did not occur. Instead, we observed an expanding, hemispherical front similar to the blast wave normally associated with the target's laser-side (Fig. 11). Long wavelength nonuniformities, similar to weak regions on the surface of an expanding balloon, replaced the fine-scale turbulent structure associated with ablatively accelerated targets. This observation supports the turbulent target model.

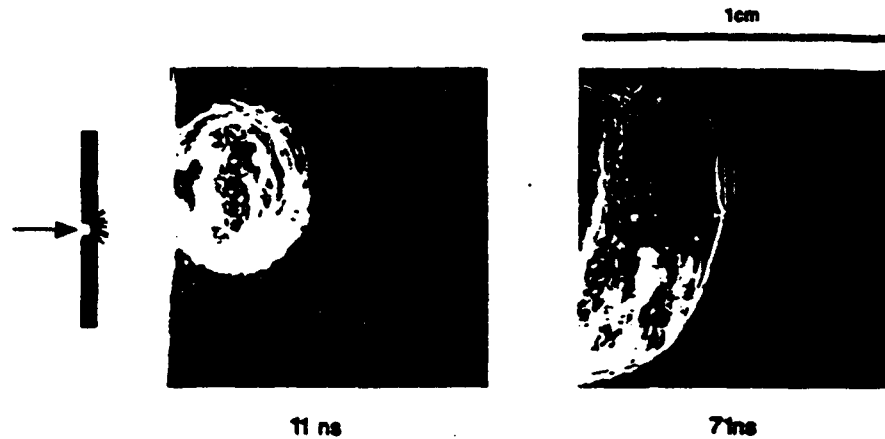


FIGURE 11. Schlieren shadowgraphs of a $9\mu\text{m}$ CH foil in 5 torr of nitrogen irradiated by a tightly focused laser beam to $320\text{ terawatts}/\text{cm}^2$. Note lack of turbulence. Laser is incident from the left.

Structured targets: The Rayleigh-Taylor instability in flat targets develops from natural material imperfections or from nonuniformities in the laser beam. The wavelengths which grow can be controlled by purposefully imposing a large mass perturbation on the target - for example, by grooving its surface^{6,7,8}. Now, if the turbulent spectrum is determined by the linear Rayleigh-Taylor instability then we should be able to alter the turbulent power spectrum by changing the wavelengths at which Rayleigh-Taylor grows. To test this we accelerated targets perturbed with a $100\mu\text{m}$ wavelength groove and compared the resulting turbulent power spectra to those of non-perturbed targets. We found that at early ($<10\text{ns}$) times a $100\mu\text{m}$ structure was visible in the shadowgraphs. But fully developed turbulence at 200ns had the same spectrum as that for flat targets. This supports the argument that we are observing turbulence and not a frozen eddy structure.

SUMMARY

This paper describes our studies of turbulence produced in a background gas by objects accelerated to very high velocities. We have developed methods to quantify features of the instability, in particular the power spectrum of the electron density. Also, we have measured the behavior of the turbulence under many different circumstances and determined its power spectrum. With these methods we are studying the nonlinear hydrodynamics of a system which duplicates in the laboratory many astrophysical properties. We intend to extend our methods to the study of hydrodynamics at less exotic conditions but without the complications of more classical experimental methods.

ACKNOWLEDGMENTS

We are grateful for the expert technical assistance of Nicholas Nocerino, Levi Daniels, Jim Ford, and Ray Burris who helped us conduct the experiments; Loretta Schirey who fabricated the targets; and Joshua Resnick who helped with some of the data analysis. Fruitful discussions with Drs. Cliff Prettie, Joe Huba, Wolf Seka, and T. Kessler are acknowledged. This work is supported by the Defence Nuclear Agency and the Office of Naval Research.

REFERENCES

- ¹ L.A. Wittwer, *The Propagation of Satellite Signals in a Turbulent Environment*, D.N.A. report AFWL-TR-77-183 (1978).
- ² V. Trimble, *Rev. of Modern Phys.* **60**, 859 (1988).
- ³ J. M. Scalo, in "Interstellar Processes", pg. 349:392, D. J. Hollenbach and H. A. Thronson Jr. editors, D. Reidel Publishing Company (1987).
- ⁴ D. L. Youngs, *Numerical Simulation of Turbulent Mixing by Rayleigh-Taylor Instability*, *Physica* **12D** 32:44 (1984).
- ⁵ H. Tennekes and J.L. Lumley, "A First Course in Turbulence", The MIT Press, Cambridge (1987).
- ⁶ A. J. Cole, J.D. Kilkenny, P.T. Rumsby, R.G. Evans, C.J. Hooker, M.H. Key, *Nature* **299**, 329 (1982).

- ⁷ J. Grun, M.H. Emery, S. Kacenjar, C.B. Opal, E.A. McLean, S.P. Obenschain, Phys. Rev. Lett. **53**, 1352 (1984). J. Grun and S. Kacenjar, Appl. Phys. Lett. **44**, 497 (1984).
- ⁸ J. Grun, M.H. Emery, C.K. Manka, T.N. Lee, E.A. McLean, A. Mostovych, J. Stamper, S. Bodner, S.P. Obenschain, B.H. Ripin, Phys. Rev. Lett. **58**, 2672 (1987).
- ⁹ B.H. Ripin et al, in Laser and Particle Beams **8**, (1990) [in press].
- ¹⁰ J. M. McMahon et al., IEEE J. Quant. Elec. **OE17**, 1629 (1981).
- ¹¹ R. H. Lehmberg and S.P. Obenschain, Opt. Comm. **46**, 27 (1983).
- ¹² This description of the laser-foil interaction and the resulting turbulence is placed here to provide a frame of reference for the reader. Some of the assertions are based on extensive studies in the references, others are the subject of this article.
- ¹³ P.G. Burkhalter, M.J. Herbst, D. Duston, J. Gardner, M. Emery, R.R. Whitlock, J.Grun, J.P. Apruzese, J. Davis, Phys. Fluids **26**, 3650 (1983).
- ¹⁴ J. Grun, R. Stellingwerf, B.H. Ripin, Phys. Fluids **29**, 3390 (1986).
- ¹⁵ J. Grun, R. Decoste, B.H. Ripin, J. Gardner, Appl. Phys. Lett. **39**, 545 (1981).
- ¹⁶ J. Grun, S.P. Obenschain, B.H. Ripin, R.R. Whitlock, E.A. McLean, J. Gardner, M.J. Herbst, J.A. Stamper, Phys. Fluids **26**, 588 (1983).
- ¹⁷ B.H. Ripin, A.W. Ali, H.R. Griem, J. Grun, S.T. Kacenjar, C.K. Manka, E.A. McLean, A.N. Mostovych, S.P. Obenschain, and J.A. Stamper, in Laser Interaction and Related Plasma Phenomena. Vol. 7, Edited by H. Hora and G.H. Miley (Plenum Publishing, 1986).
- ¹⁸ J. Crawford, J. Grun, J.A. Stamper, B.H. Ripin, and C.K. Manka, Bull. Am. Phys. Soc. **34**, 1921 (1989); also to be published.
- ¹⁹ F. Zernike, Physica **1**, 689 (1934); Physica **9**, 686 (1942).
- ²⁰ L. J. Cutrona, E.N. Leith, C.J. Palermo, L.J. Porcello, I.R.E. Transactions on Information Theory, **June**, 386:400 (1960).

- 22 H. M. Presby and D. Finkelstein, The Review of Scientific Instruments 38, 1563 (1967).
- 23 In extreme cases one can envision all of the probe light being deflected so that there is no DC term at all: The term 1 is cancelled by the DC components of the phase terms. (Cliff Prettie, private communication) This is minimized by overfilling the turbulent region so there is always a nondeflected part of the probe.
- 24 C. L. Rufenach, J. of Geophysical Research 77, 4761 (1972).
- 25 F. J. Harris, " On the Use of Windows for Harmonic Analysis with the Discrete Fourier Transform", Proc. of the IEEE 66, 51 (1978).
- 26 M. Takeda, H. Ina, S. Kobayashi, J. Opt. Soc. Am. 72, 156 (1982).
- 27 K. A. Nugent, Applied Optics 24, 3101 (1985).